中華民國顯微鏡學會

第24屆學術研討會彙刊

PROCEEDINGS OF THE 24th R.O.C. SYMPOSIUM ON MICROSCOPY

中華民國九十三年一月十七日
台北市 國防大學國防醫學院
January 17, 2004
National Defense Medical Center
Taipei, Taiwan, R.O.C.

中華民國顯微鏡學會

第24屆學術研討會彙刊

PROCEEDINGS OF THE 24th

R.O.C. SYMPOSIUM ON MICROSCOPY

2004

顯微鏡學會

學術研討會

國防大學國防醫學院生物及解剖學科

中華民國九十三年一月十七日

目　　錄

中 華 民 國 顯 微 鏡 學 會

Microscopy Society of Republic of China (MSROC)

PROCEEDING OF THE 24th SYMPOSIUM ON MICROSCOPY

Jan 17, 2004, Taipei

8 : 00 - 9 : 00	**Registration**			
9 : 00 - 9 : 30	**Opening Ceremony (33 教室)**			
主題演講	**Chairman： 王長君、陳力俊 (33 教室)**			
9 : 30 - 10 : 00	**Professor Hideki Ichinose** **HRTEM and EELS Study: Atomic and Electronic Structure of Interface**			
10 : 00 - 10 : 15	Coffee break			
10 : 15 - 10 : 45	**Professor Harumichi Seguchi**			
10 : 45 - 11 : 00	Coffee break			
11 : 00 – 12 : 00	**Annual meeting (33 教室)**			
12 : 00 - 14 : 00	Lunch and Poster Sessions			
Oral Sessions（I）	**Biomedical Session (32 教室)**		**Physical Science Session (33 教室)**	
Chairs：	**黃玲瓏、游祥明**		**開執中、薛富盛**	
	14 : 00 - 14 : 20	黃玲瓏	14 : 00 - 14 : 20	陳力俊
	14 : 20 – 14 : 40	李金梅	14 : 20 – 14 : 40	王玉麟
	14 : 40 – 15 : 00	游祥明	14 : 40 – 15 : 00	王文雄
	15 : 00 - 15 : 20	龔秀妮	15 : 00 - 15 : 20	李志浩
15 : 20 - 15 : 40	Coffee break			
Oral Sessions（II）	**Biomedical Session**		**Physical Science Session**	
Chairs：	**楊瑞森、周逸鵬**		**楊哲人、徐統**	
	15 : 40 - 16 : 00	連宜珍	15 : 40 - 16 : 00	張　立
	16 : 00 - 16 : 20	陳振儀	16 : 00 - 16 : 20	歐陽浩
	16 : 20 - 16 : 40	黃靜端	16 : 20 - 16 : 40	劉全樸
			16 : 40 – 17 : 00	陳福榮
17 : 00 – 18 : 00	**討論、頒獎、摸彩、閉幕 (33 教室)**			

中華民國顯微鏡學會

第十一屆理、監事名錄

理事長	王長君	國防大學國防醫學院生物及解剖學科暨研究所	教授
副理事長	開執中	清華大學工程與系統科學學系	教授
常務理事	沈博彥	中山大學材料科學研究所	教授
	王文雄	台灣大學材料科學研究所	教授
	陳淑華	台灣大學植物學系	教授
理事	郭長生	成功大學生物學系	教授
	徐鴻泉	中興大學植物病理學系	教授
	王重雄	台灣大學昆蟲學系	教授
	陳榮銳	台灣大學植物學系	教授
	黃宏圖	中山大學生物學系	教授
	楊瑞森	海洋大學海洋生物研究所	教授
	鮑忠興	工業技術研究院工業材料研究所	研究員
	林文台	成功大學材料科學系	教授
	張立	交通大學材料科學系	教授
	謝詠芬	閎康科技	總經理
常務監事	鍾美珠	中央研究院植物所	副研究員
監事	游祥明	陽明大學生命科學院解剖研究所	教授
	黃玲瓏	台灣大學植物學系	教授
	楊哲人	台灣大學材料科學研究所	教授
	薛富盛	中興大學材料科學系	教授
榮譽理事	李英雄	長庚醫工大學醫學院	院長
	侯書文	台灣大學醫學院病理科	教授
	陳脈紀	中興大學植物病蟲害系	教授
	吳信淦	中央研究院植物所	研究員
	林良平	台灣大學農化系	教授
	陳力俊	清華大學科學工程學系	教授
秘書長	吳慶祥	國防大學國防醫學院生物及解剖學科	副教授

中 華 民 國 顯 微 鏡 學 會

Microscopy Society of Republic of China (MSROC)

中華民國顯微鏡學會新會員入會申請書

（一）姓名: _____ 性別：_____ 出生年月日： _____

（二）服務機關：_____ 職務：_____

（三）永久地址：

通 訊 處：_____

Phone： _____ Fax： _____

E-mail：_____

（四）學歷： 畢業年月

（1）_____ _____

（2）_____ _____

（五）經歷：

（1）_____

（2）_____

（3）_____

（六）主要研究領域：

（1）_____

（2）_____

（3）_____

（七）申請入會爲 (1)永久會員：入會費 NT. 600 永久會費 NT. 3,000
(2)一般會員：入會費 NT. 600 常年會費 NT. 500
(3)學生會員：入會費 NT. 200 常年會費 NT. 100
(4)團體會員：入會費 NT. 10,000 常年會費 NT. 5,000

（八）介紹人

(1)姓名：_____ 簽章： 服務機關與職務：_____

(2)姓名：_____ 簽章： 服務機關與職務：_____

（九）申請人簽章: _____ 中華民國 年 月 日

會議論文摘要目錄

主題演講

論文宣讀

[材料物理組]

論文壁報展示

[材料物理組]

主題演講

論文宣讀

LOWER BAINITE IN JIS SK5 STEEL

TU, Meng-Yin[1](涂孟寅)；HSU, Yung-Fu[2](徐永富)；WANG, Wen-Hsiung[1](王文雄)

1.Department of Materials Science and Engineering, National Taiwan University, Taipei
2.Department of Materials and Mineral Resources Engineering, National Taipei University of Technology, Taipei

The microstructure of JIS SK5 steel was investigated in this study. The specimens were austenitized at 880℃ for 30 min and then austempered at 300℃ for 1hr. The TEM bright field images of lower bainite in the specimen are shown in Fig. 1. It can be seen that bainitic ferrites(α_1) are plate-like,and cementite platelets(θ_2) are embedded in the ferrite and precipitated unidirectionally at an angle of 55 to 60 deg to their long axes[1], in addition, ferrites(α_2)/cementites(θ_2) layers appear at the interface of plate-like bainitic ferrites, which are decomposed from the retained austenites.

Fig. 2(a) shows the selected area diffraction pattern(SADP) of α_1, θ_1 and θ_2 phases, and the result of stereographic analysis of this SADP is shown in Fig. 3. It indicates that the α_1/θ_2 orientation relationship close to that of Isaichev[2] as follow：

$$[1\bar{1}1]_\alpha // [010]_\theta \qquad (\bar{1}10)_\alpha // (10\bar{3})_\theta$$

However, the orientation of α_1 and θ_1 does not possess Isaichev relationship. Fig. 2(b) shows the SADP of α_1 and α_2 phases, which is composed of two diffraction patterns of and zones. It indicates that the α_2 is decomposed from the retained austenites with an orientation different to that of α_1.

The mechanisms of lower bainite transformation can be postulated as in Fig. 4 [3]. The ferrite subunits with the parallelogram cross sections nucleate at the austenite grain boundary(Fig. 4(a)) and then cemenite platelets will precipitate on one parallel set of the cross sectional interfaces before these subunits coalescence(Fig 4(b)). After that bainitic ferrites will grow broader, longer and thicker with increasing transformation time, and ultimately will be plate-like(Fig 4(c)). At the interface of bainitic ferrites there will be ferrites(α_2)/cementites(θ_2) layers decomposed from retained austenites(Fig 4(d)).

References
1.G. Lai, Metall. Trans., 6A(1975) 1469.
2.H. K. D. H. Bhadeshia, Scripta Metall., 14(1980) 821.
3.Ohmori Y., Mater Trans JIM, 30(1989) 487.

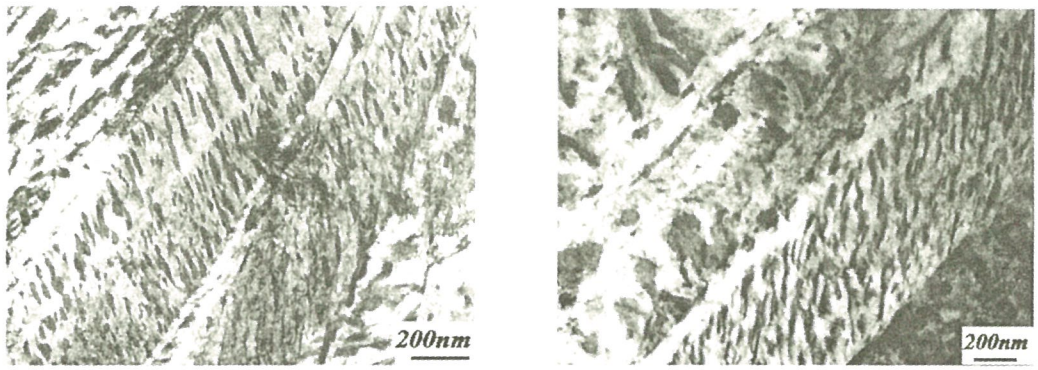

Fig. 1 TEM BF images of lower bainite in the SK5 steel

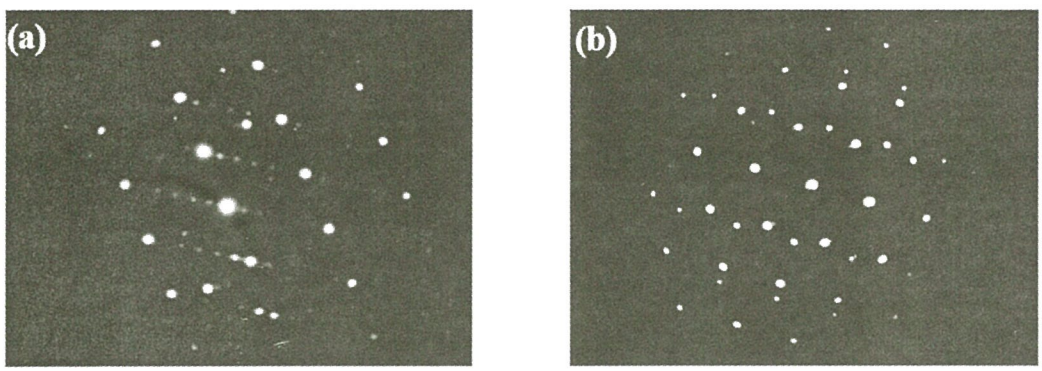

Fig. 2 Diffraction pattern of (a) $\alpha_1/\theta_1/\theta_2$ and (b) α_1/α_2

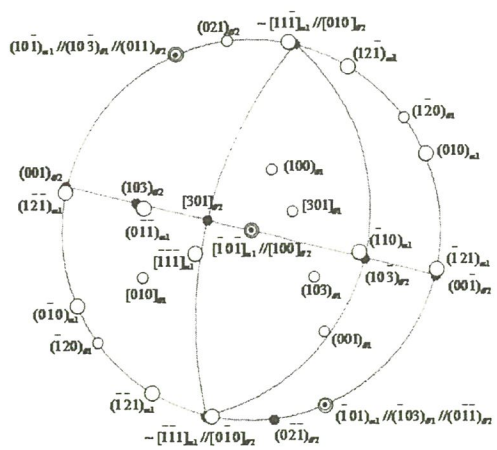

Fig. 3 Stereographic analysis of Fig. 2(a)

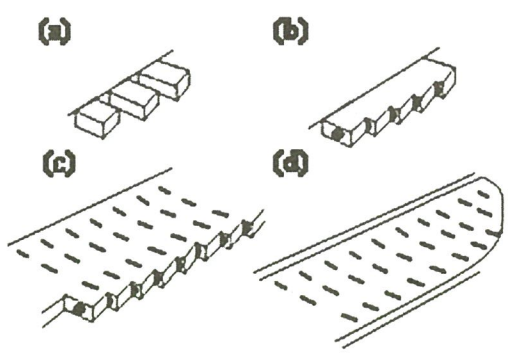

Fig. 4 Schematic illustration of lower bainite formation

Atomic Resolution Tomography and Property Imaging for Nano-Analysis

Fu-Rong Chen and Ji-Jung Kai

Department of Engineering and System Science, National Tsing-Hua University, HsinChu

The dream of microscopists is to determine simultaneously the structure and property of new materials. Although, high resolution TEM is very powerful to resolve the structural variation with atomic resolution, it lacks compositional and property information. The compositional information of one atomic column can be simply related to the phase of the exit surface wave that can be approximated to be 1S state wave associated with atomic column after the electron beam interacts with the sample. In my talk, I will update the development in the theory and recent result of complex TEM and property microscopy in our lab. The "complex" TEM is a newly developed concept for direct and quantitative analysis of atomic structure. The basic idea of complex TEM is to retrieve the phase (and so the wave) of each image planes from a series of de-focal images. The aberration of the objective lens can then be corrected and the directly interpretable wave in the exit surface of sample is recovered. The atomic structure accompanying with the information of the composition in single atomic column can be directly quantified. Quantitative analysis of the exit wave is still a under-developing advanced technique. That can be carried out either using 1S state wave or analytical form of multi-slice formular. The detail algorithm and theory of this method can be found in our recent publication in "Ultramicroscopy". Once the exit wave is reconstructed from more than one crystallography orientation, we can reconstructed 3-d atomic resolution tomography using back projection algorithm.

Electron energy loss spectrum (EELS) provides complementary information from that obtained by high resolution TEM. Complex TEM may give us information of the structure/ composition with atomic resolution, while we can extract the property of the material with near nano-meter resolution from analysis of the EELS. For instant, we can extract the dielectric function, band energy from the low loss region (several eV to 30eV) and chemical bonding information as well as the density of state from analysis of the core loss spectrum (100eV and up). As mentioned wherelse, the surface may play an important role in controlling the property of nano-materials. If two dimensional EELS data can be acquired and analyzed two dimensionally with spatial resolution of nanometer scale, we can actually obtain form property from where the EELS acquired from and so two dimensional"property

image" can be formed. The concept of the property imaging is new and can be seen from several of our recent publications. There are two ways to obtain two-dimensional EELS spectrum. One is using a fixed focused electron beam scans over the sample at the same time EELS spectrum is recorded. This method is referred as spectrum image. The second is reconstructing the EELS spectrum from a series of energy loss images. This technique is referred to be electron spectroscopy imaging (ESI). In the ESI, a parallel beam is used and least beam damage is introduced. We therefore prefer and have set up the second method to explore the several property map from different kinds of nano-materials. The methodology and the detail algorithm of property reconstruction can be found from our publication. In the past year, we have demonstrated the possibility to obtained dielectric function image, band energy image and sp2/sp3 chemical bonding image. I will show the examples of band energy map from GaN/ AlN quantum well pair and sp2/sp3 chemical bonding map in the diamond like multi-layers. Two difficulties exist in the application of this technique to the core loss regime. They are, first, the weak contribution from this core loss signal and the energy resolution. Second, noise is usually the key factor to limit application of ESI to the core loss to record reliable energy loss images. Energy resolution of ESI depends on two factors. The energy resolution of a regular field emission gun TEM is about 1eV in the condition of sufficient beam intensity. The movement and the width of the energy slit is usually also in the range of 1eV. These limit the fine detail structure in the EELS spectrum that can be extracted. In my talk, I will address the possibility to develop state of art analytical method on the mapping of density of state for nano-materials by ESI and find out the correlation between the theory of quantum transport in nano-scale.

Growth of Novel Nanostructures on Self-Assembled Hexagonal Au Particle Networks on Various Substrates

CHEN, Lih-Juann (陳力俊) ; SU, Pai-Ying (蘇百櫻); HE, Jr-Hau (何志浩); CHIANG, Ten-Fu (蔣天福) and WANG, Jen-Hung (王仁宏)

Department of Materials Science and Engineering, National Tsing Hua University, Hsinchu, Taiwan

Novel nanostructures were grown on individual Au particles in self-organized hexagonal networks with discrete Au particles on various substrates in annealed drop-cast samples from the Au nanoparticle solution. Au nanocrystals were synthesized using a two-phase method. Regular hexagonal network was found to form in drop-cast samples by self-organization with a wide range of conditions. In samples annealed at high temperatures, regular hexagonal Au network was observed to form.[1]

Two kinds of structures were found in samples annealed in samples annealed at 1100 ^{0}C for 60 min in N_2 ambient. The first is of flowery appearance and the second is like bean sprout at each of the Au particle site. Examples are shown in Figs. 1 (a) and (b). The nanowires were found to be composed of Si and O from the EDS analysis of TEM samples. The flowery and bean-sprout-like structures were found to grow on relatively thin (10 nm) and thick (100 nm) Si oxide, respectively. The flower-like structure was also found to grow from Au particle on 100-nm-thick SiO_2/Si substrate.

The formation of regular Au particle hexagonal networks was also achieved on Si-Ge and Al_2O_3 surfaces. Figures 2 and 3 show flowery oxide nanowires grown on Si-Ge and Al_2O_3, respectively. From photoluminescence measurement, the Ge-Si-O nanowires were found to emit blue light. On the other hand, the Au particles on c-cut sapphire are facetted with (111)Au//(0001) Al_2O_3. Furthermore, the nanowires tend to grow on {001}, but not on {111} planes. An XTEM image is shown in Fig. 4. For CVD-Cu, Au particles were encased by the Cu particles as shown in Fig. 5.

Promising results were also obtained for the network formation in Au/Si_3N_4, Au/sapphire and Ag/Si systems and for the selective growth of Si and ZnO nanowires on Au particles. The growth can be explained in term of VLS growth and Au-Si-O intermixing during heating and precipitation upon cooling. The scheme to form the Au particle network controlled offers an effective and economical means to produce a universal template to grow functional structures without complex lithography. The wealth of fascinating structures and associated phenomena of the systems points to an exciting new area for future research.

[1]SU, Pai-Ying; LU, Ming-Yan; LIANG, Ju-Ming; CHENG, Shao-Liang; HU, Jung-Chih and CHEN, Lih-Juann, this Proceedings (2004).

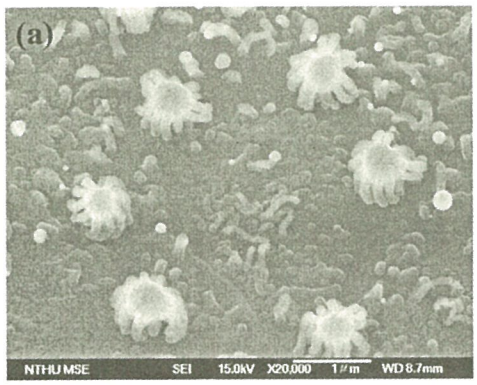

Fig. 1(a) SEM image of an Au/Si sample annealed at 1100 ℃ for 60 min showing the flower-like structure.

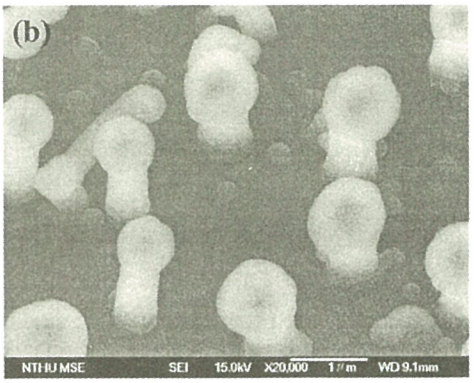

Fig. 1(b) SEM image of an Au/Si sample annealed at 1100 ℃ for 60 min showing the bean sprout-like structure.

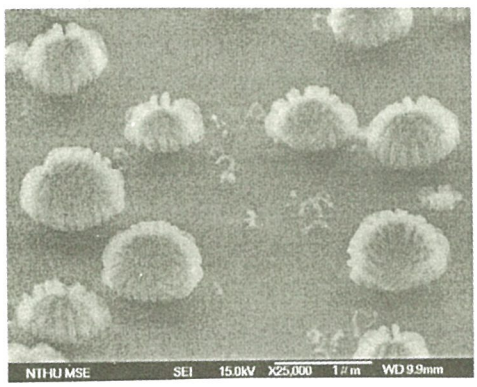

Fig. 2 SEM image showing flowery oxide nanowires grown on Au/Si-Ge.

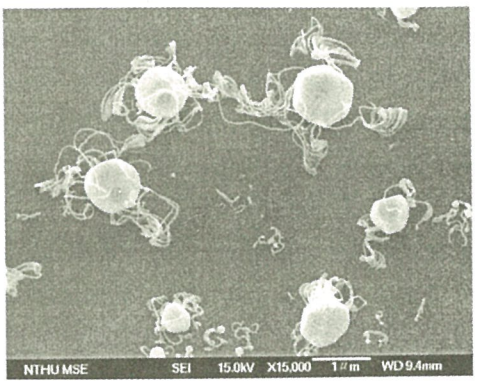

Fig.3 SEM image showing flowery oxide nanowires grown on Au/Al_2O_3.

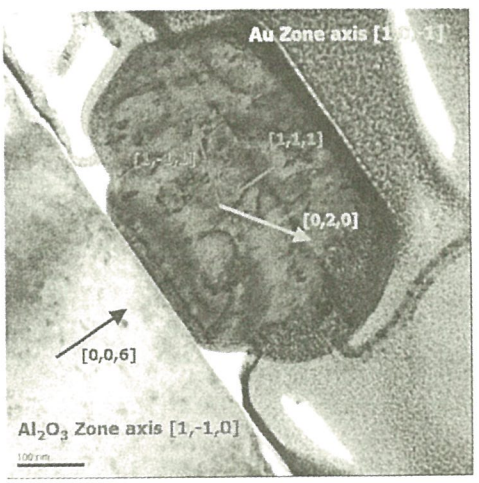

Fig.4 XTEM image showing flowery oxide nanowires grown on Au/Al_2O_3

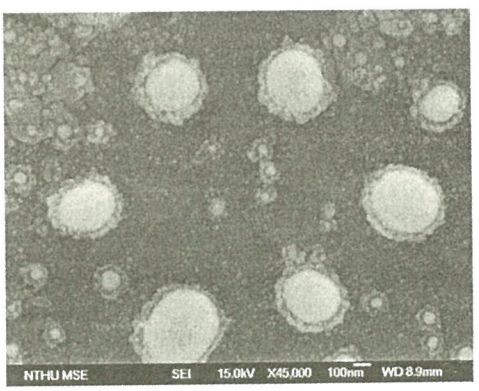

Fig.5 SEM image showing Au particles encased by the Cu particles.

CHARACTERIZATION OF CARBON NANOTUBE BY TRANSMISSION ELELCTRON MICROSCOPY

Jeng-uii Wang ; Chih-Chin Wang ; Chuan-Pu Liu

Department of Materials Science and Engineering, National Cheng-Kung University, Tainan, Taiwan

The variety of nanodevices based on CNT has motivated this filed and the large range of possible properties is associated with many possible microstructures available in CNT [1,2]. Due to the complexity, the precise control of selective CNT growth is difficult and reliability issue occurs. In addition, the detailed growth mechanism behind is a key but also a difficult question. All these await a better understanding of CNT microstructure including helicity, type of CNT, chemistry and all possible defects, which demands a better characterization. Since the microstructure is complex, a TEM simulation from an ideal model helps understanding the correlation between diffraction experiment and real atomic structures. Fig. 1 and Fig.2 show our preliminary results. The ideal atomistic models are built first as in the top row of the figure. Through dynamical scattering theory, a multislice calculation is employed to simulate the diffraction patterns and images, which are shown in the bottom two rows of Fig.1 for single- and three-walled CNT with indices from (10,0), (10,5) to (10,10) and in Fig.2. The symmetry of the atomic arrangement in the CNT is reflected in the patterns. In principle, if the electron beam is perpendicular to the tubular nanowire, the relative positions of two (10-10) diffraction spots would be enough to derive the helicity and the type of the CNT. When more walls associated with the CNT, the diffractions patterns include all fundamental spots and the repeated unit from the arrangement of the walls, which becomes much stronger and makes the spot more sharp. If any additional spot or any spot missing, which then suggests some defects either destroy some symmetry or create new symmetry. The numbers of walls is better examined in imaging mode, which has been simulated as shown in Fig.2. The atomic like structure can be identified, however, it is doubt that these structures can be imaged experimentally due to the small diffraction volume. More work is undertaken to be able to distinguish the defect type and the atomic structure for multi-walled CNT between "Russian doll" and " Swiss cake" models.

Reference

[1] T.W. Ebbesen, Caron Nanotubes: Preparation and Properties, CRC press, 1997.

[2] J.F. Harris, Carbon Nanotubes and Related Structures, Cambridge University Press, 2001

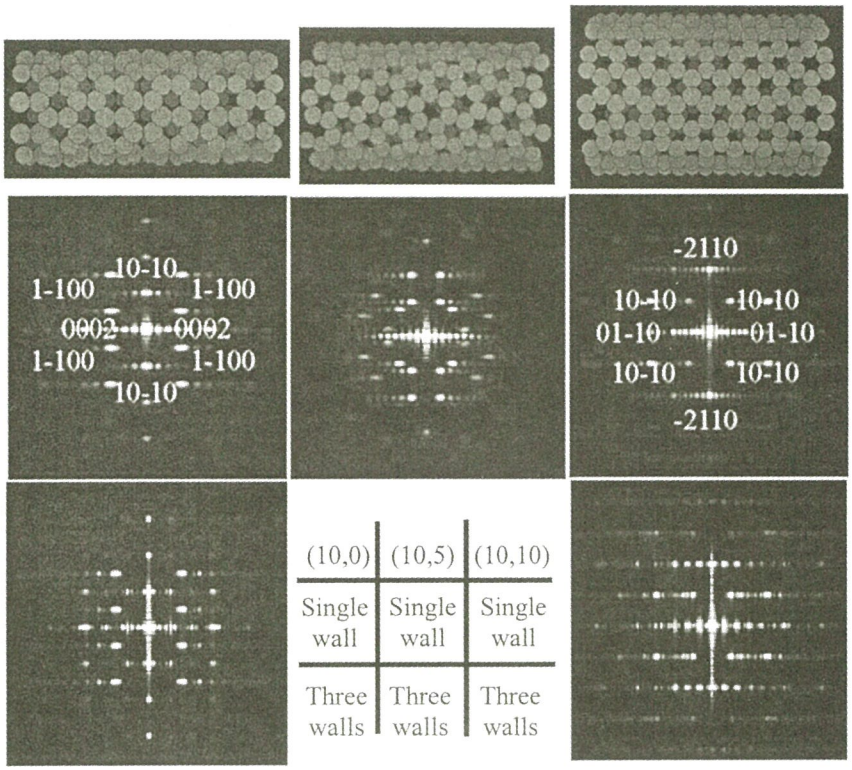

Fig. 1. Simulated diffraction patterns from single-wall and three-walled CNTs with the atomic structures of various types of CNTs including (10,0), (10,5) and (10,10) from left to right.

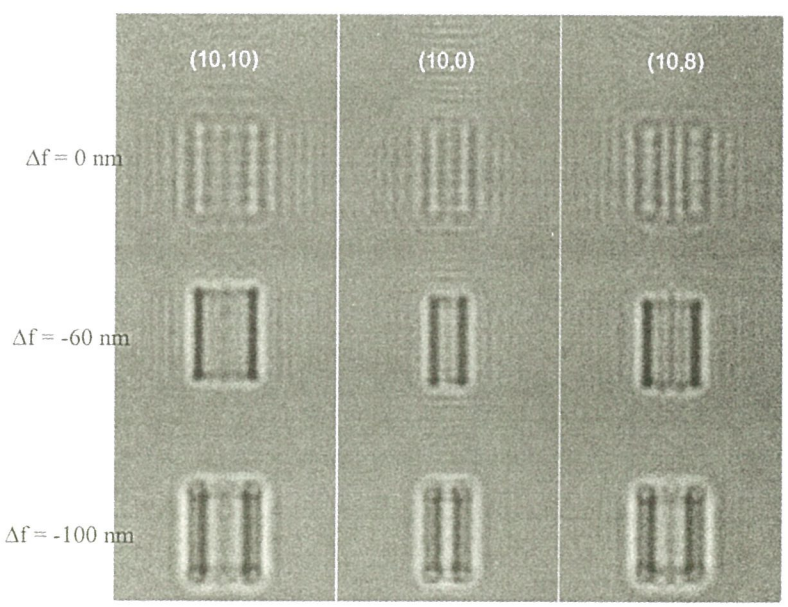

Fig. 2. Simulated single-wall carbon nanotube images with defocus for (10,0), (10,8) and (10,10).

The Study of White Lines and d Occupancy for the 3d Transition Metals, Related Oxides

Hao Ouyang[1], Jen-Tai Kwan[1], C.C. Ahn[2] , J. Graetz[2] and B. Fultz[2]
[1] National Chung Hsing University, Department of Materials Engineering, Taichung, Taiwan 402, R.O.C.
[2]California Institute of Technology, Division of Engineering and Applied Science Mail Code 138-78, Pasadena, CA91125

ABSTRACT

Electron-energy loss spectrometry(EELS) was employed to measure the intensities of the white lines of $L_{2,3}$ absorption edges for 3d transition metals and related oxides as shown in figure 1. The white line ratio ($L3/L2$) was found to increase between $d0$ and $d5$ and decrease between $d5$ and $d10$, consistent with previous results for the transition metals and their oxides.

The intensity of the white lines corrected by the matrix elements[1], normalized to the trailing background, is linear versus d occupancy for the $3d$ transition metals, $3d$ transition-metal oxides and lithium transition-metal oxides as represented in figure 2. An empirical correlation between normalized white line intensity and $3d$ occupancy is established. It provides a way for measuring variations in the $3d$-state occupancy and can be used in some important applications as shown in figure 3[2].

REFERENCE

1. D. H. Pearson, C. C. Ahn, and B. Fultz. Phys. Rev. B, 47, 8471, 1993.
2. Hao Ouyang, Jen-Tai Kwan, Journal of Applied Physics, **92**, 7510, 2002

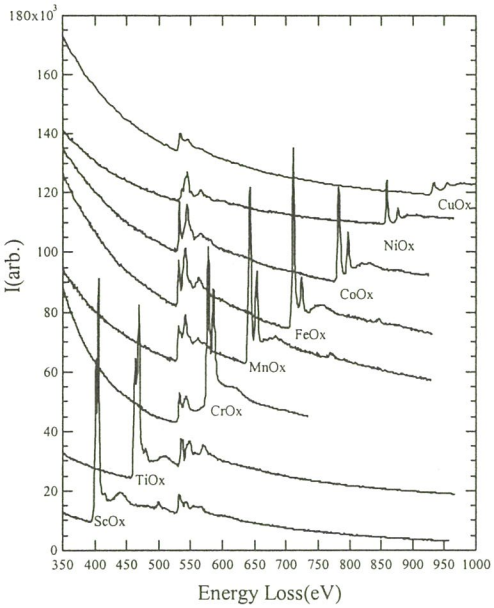

Figure 1. Energy-loss spectra of the transition-metal *L*2,3-edges from a number of transition-metal oxides.

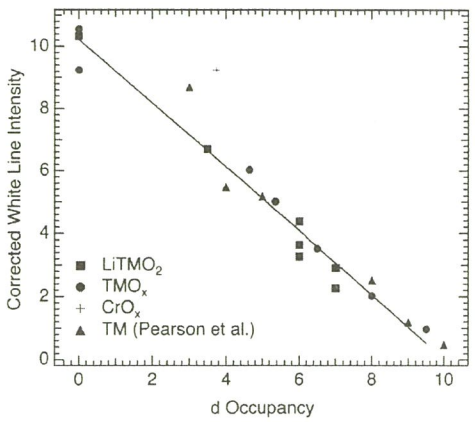

Figure 2. Normalized white line intensity for a series of transition metals, transition-metal oxides, and lithium transition-metal oxides plotted vs. *d*-occupancy. The CrO*x* datum (+) was not included in the linear fit.

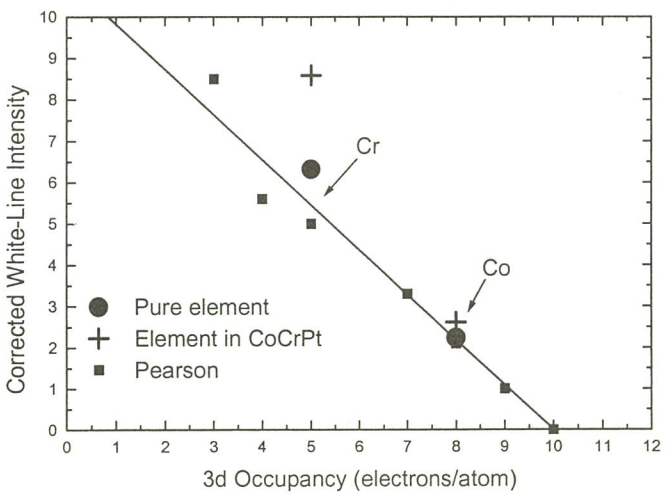

Figure 3. Corrected white-line intensity for Co and Cr being plotted with 3d transition metals

The opportunity of using the microscopy at National Synchrotron Radiation Center

Chih-Hao Lee (李志浩)
Department of Engineering and System Science, National Tsing Hua University, Hsinchu （清大工科系）; Nuclear Science and Technology Development Center, National Tsing Hua University, Hsinchu（清大原科中心）; Users Executive Committee, National Synchrotron Radiation Research Center（國家同步輻射研究中心）, Hsinchu, Taiwan.

Microscopy development using synchrotron radiation is a frontier instrument development at synchrotron community. With the high brilliant synchrotron radiation beam covering a photon energy from IR to hard X-ray, different kind of microscopies can be developed. By using photon microscopy, the best advantage over the TEM/SEM is the less radiation damage, which is very important if a living cell is to be observed *in vivo*.

Several state of art microscopies were setup in the past few years at National Synchrotron Radiation Research Center (NSRRC) in Taiwan. These microscopies are phase contrast X-ray microscopy, spectra-microscopy, photoemission electron microscopy (PEEM) and IR-microscopy. The phase contrast X-ray microscopy taking advantage of highly collimated synchrotron radiation reveals the edge of an object by Fresnel diffraction even if the electron density of the object is similar to the environment. The current lateral resolution is about 1 μm using a high resolution CCD camera. Spectra-microscopy combining the technology of X-ray absorption spectroscopy and the technology of X-ray microscopy can show the chemical state information of a sample with 0.1 μm lateral resolution. PEEM is able to show the photoemission spectra at lateral resolution of 1 μm. Using the circular synchrotron radiation producing by shifting undulator, the image of different spin orientation can be revealed by PEEM. IR microscopy using the high intensity continuous IR spectra at synchrotron radiation, the vibration strength at different chemical bonds in different domains can be revealed. The lateral resolution is about 10 μm. This IR microscopy is very important in biology samples because most of the biological materials composed of C, N, and O with no difference in electron density contrast.

Several microscopies had been developed in the synchrotron community by taking the advantages of tunability of incident X-ray energies of synchrotron radiation. For instants, contact X-ray microscopy with lateral resolution of 20 nm had been reported. A photoresist placed under the sample after exposure of soft X-rays can be etched to reveal the contrast of electron density in the sample. The penetration of

X-ray depends not only on the electron density of the sample but also on the incident X-ray energies. With soft X-ray of energy between the K-edge of oxygen and carbon, it forms a water window, especial good for imaging a small living bacteria or cells. The development of X-ray tomography with a spatial resolution of 10 μm can see the porous microstructure. With tunability of X-ray energy, special element distribution in space can be measured using the K-absorption edge of the sample. For example, the uptake of calcium of a cell can be revealed by subtracting two images taken with the incident X-ray energy one just below the K-edge and the other one just above the K-edge of calcium. X-ray angiography using the iodine as the photon absorbent, by taken two pictures with X-ray energy just below and above the iodine k-edge, the subtraction of these two images shows only the iodine image in the blood vessels. The X-ray topography using the high collimating incident synchrotron radiations can be used to show the dislocation density or the defeats in a highly ordered single crystals nondestructively. The sample can be treated in an oven or applied pressure and monitoring the dynamics change of dislocations. Those microscopy is not yet developed in NSRRC in Taiwan.

In compared with the electron microscopy, the large beam size of the incoming X-ray and the diffraction limit of optical light limit the lateral resolution of a photon microscopy. For long wavelength optical microscopy, the application of near-field technology already breaks the diffraction limitation and can reach a resolution of 20 nm. However, Micro-X-ray beam is still under developed. The large area of grazing incidence focusing mirrors was developed. The flexible bent crystal in Rowland circle was also developed. The high-resolution zone-plate is slowly making progress. The newly developed focusing capillary tube to focus the X-ray beam was also tried and 1 μm was achieved. The recently developed X-ray lenses using small beryllium balls is also reported. None of them is capable to apply well within sub-micrometer resolution without sacrifice the high intensity throughput. To remedy the loss of intensity due to high resolution operation, high intensity light source is needed. The development of undulator and free electron laser to enhance the incident photon brilliance by three orders of magnitude already on the frontline of synchrotron community.

CHARACTERIZATION OF MORPHOLOGY OF DIAMOND NANOPLATELETS

HOU-GUANG CHEN(陳厚光), CHUN-AN AN LU(盧俊安), SHI-YIN CHO(卓仕寅), LI CHANG(張立)
Department of Materials Science and Engineering, National Chiao Tung University, Hsinchu, Taiwan 300

Diamond formed by microwave enhanced chemical vapor deposition at high temperature (>1000 °C) is observed in a platelet-like morphology as shown in Fig. 1, which is unusual in diamond crystal growth. The platelet shape can be in hexagon and triangle, and has an average thickness of 30 nm with the length ranged from a few hundreds of nanometers to several micrometers. It is well known that twin in platelet crystals plays a crucial role on lateral growth and the morphology. Here we show the observation of the morphology of the diamonds, particularly on the side face structure.

In the bright-field TEM micrograph (Fig.2), it can be seen a diamond platelet in a nearly hexagonal shape. The platelet is oriented in 111 direction as shown in the SAD pattern. All the edges are along a specific direction of <110> with an inclined angle of 120° between the neighboring edges. A side-view of another diamond platelet is shown in Fig.3 with the corresponding SAD pattern. The thickness of the platelet is about 30 nm. The diffraction exhibits the typical characteristics of twinning reflections in [110] zone axis. The surfaces of the diamond platelet are parallel to {111} planes. The platelet apparently consists of multiple parallel twins in a few nanometers. Detailed examination of the image at the side face around the twin plane with the diffraction pattern reveals that the morphology is in fact a ridge structure composed of {100}and {111} faceted planes different from previous thought that the facets are all bounded by {111}.

Interestingly, diamond in slightly different morphology of six-side platelet is also observed as shown in Fig. 4. The orientation of the diamond is clearly in [110]. The edges are corresponding to {111} and {100} planes. The twinning diffraction caused by the twins in the middle of the platelet. Theses twins are not parallel to the surfaces, which might lead to formation of various polyhedral shapes of crystallites.

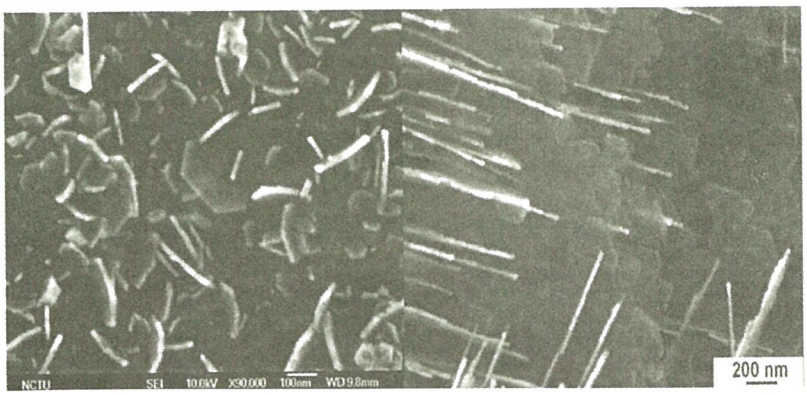

Fig. 1 SEM micrograph showing that the diamond platelet shape can be in hexagon and triangle.

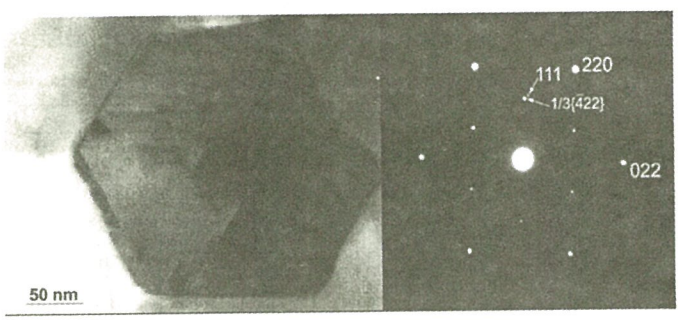

Fig. 2 Bright field TEM image of a hexagon diamond platelet and corresponding SAD pattern.

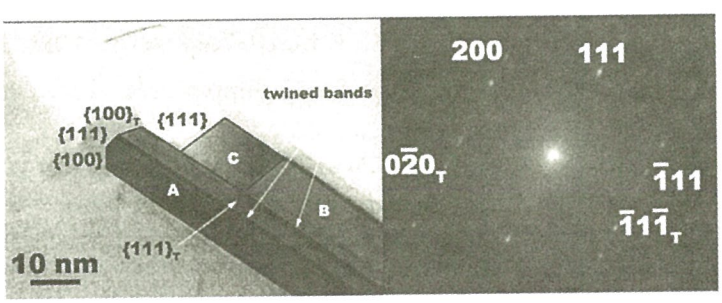

Fig. 3 The side-view TEM image showing a ridge structure composed of {100} and {111}, faceted planes and corresponding SAD pattern.

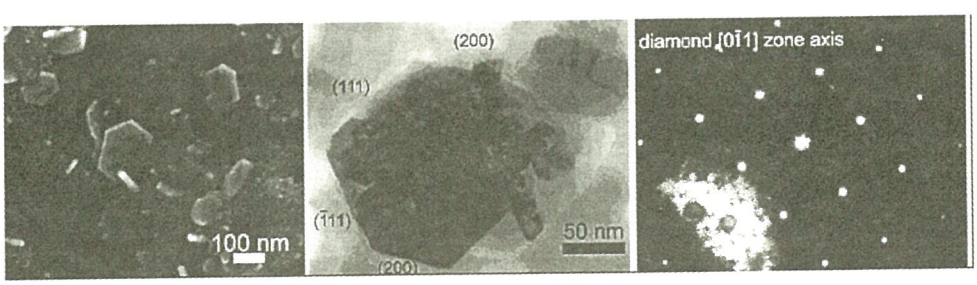

Fig. 4 SEM micrograph showing the hexagonal diamond platelet shape and the top-view TEM image showing diamond with {110} faceted plane and corresponding SAD pattern.

GROWTH STRAINS AND GELATINOUS FIBERS OF THE TRUNKS OF *Trochodendron aralioides*.

Kuo-Huang, Ling-Long (黃玲瓏)[1]，Huang, Yan-San（黃彥三）[2]，Chen, Shih-Shih（陳欣欣）[2]，and Hsieh, Yi-In（謝宜殷）[1]

[1] Institute of Ecology and Evolutionary Biology, University of Taiwan, Taipei, Taiwan.

[2] Division of Forest Utilization, Taiwan Forestry Research Institute, Taipei, Taiwan.

Woody trunks and limbs have the ability to generate growth stresses in the newly formed secondary xylem cells of normal and reaction wood. When growth stresses are relieved by felling and sawing, the wood may split or twist and lose value. Motivation for the study of growth stresses is both practical and theoretical. In conifers, reaction wood (compression wood) forms in the lower side, while in dicotyledons, reaction wood (tension wood) forms in the upper side. It has been reported that the cellulose-rich and small microfibril angled (MFA) gelatinous layer of G- fiber is related to the high tensile stress observed in tension wood (Okuyama et al., 1994). *Trochodendron aralioides* Sieb. Et Zucc. is a primitive, vesselless dicotyledonous native tree to Taiwan. In this study, the peripheral distribution of surface growth strains at basal part of a 30° and a 45° leaning trunks of *Trochodendron aralioides* was measured by kerf method and the formation of reaction wood was investigated. We found that high tensile strains (-1989×10^{-6} and -2383×10^{-6}) existed longitudinally on the surface of upper side of trunks (Fig. 1). From the upper to the lower side of trunks, the absolute value of strains decreased obviously. Growth strains on the lower side were slightly above zero. The observation of wood structure of the surface strain measured wood blocks showed that tension wood (tissue without G-fiber) displayed higher tensile strain than opposite wood (tissue without G-fiber) (Fig. 2-4). The microfibril angles of fibers in the opposite wood were 20-30° (Fig. 5), while the microfibril angles of G- fibers in the tension wood were below 20° . By the ANOVA analysis, longitudinal surface strains varied not significantly with the MFA of fiber cells (Fig. 6).

Okuyama, T., Yamamoto, H. Yoshida M., Hattori, Y., and Archer, R.R. 1994. Growth stresses in tension wood: role of microfibrils and lignification. Ann. Sci. For. 51: 291-300.

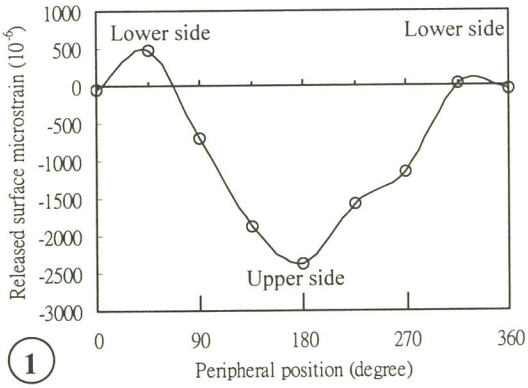

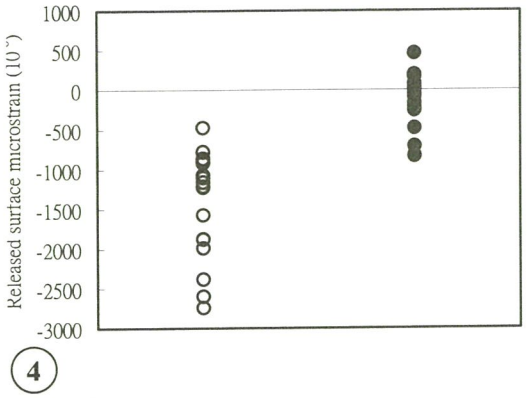

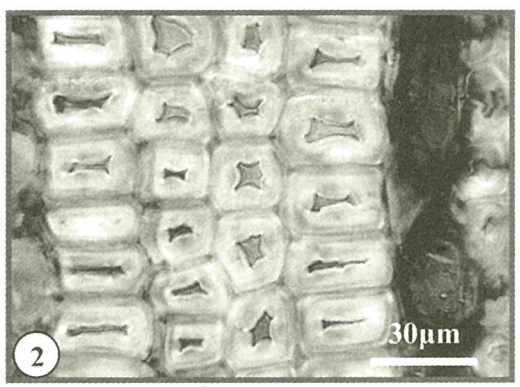

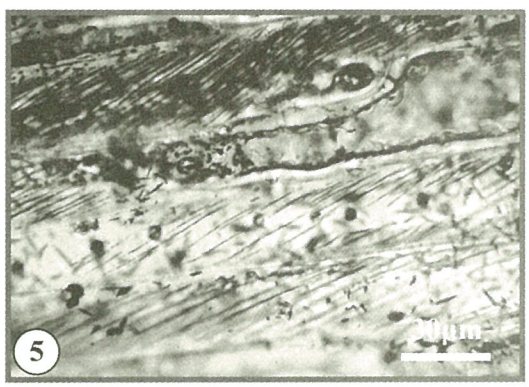

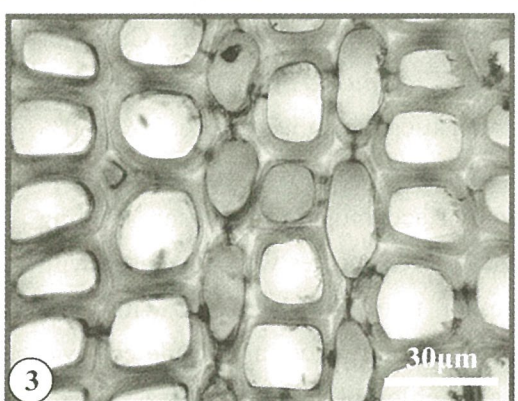

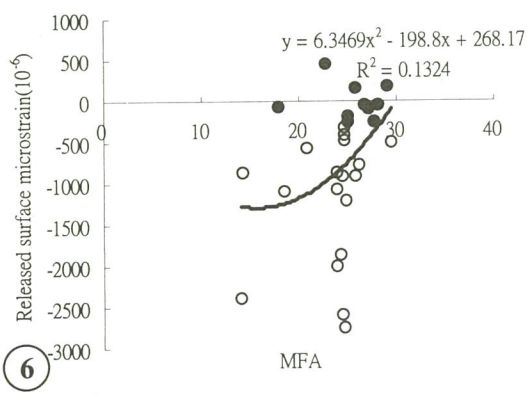

Fig. 1. Peripheral distribution of surface growth strain on a 45° leaning trunk at height of 65 cm.

Fig. 2. Gelatinous fibers in the tension wood.

Fig. 3. Fibers in the opposite wood.

Fig. 4. Comparison of surface growth strain between tension wood (○) and opposite wood (●).

Fig. 5. Microfibrils distributed in the secondary wall of fibers in opposite wood.

Fig. 6. Relation of longitudinal surface strains and MFA of fiber cells (○, tension wood; ●, opposite wood).

EFFECTS OF DIFFERENT LIGHT INTENSITIES ON THE SEEDLING GROWTH AND LEAF MORPHOLOGY OF THREE NATIVE BROAD-LEAVED TREE SPECIES IN TAIWAN

LEE, Chin-Mei（李金梅）[1]；KUO, Sing-Rong（郭幸榮）[2] and HSU, Hsien-Pin（許賢斌）[2]

[1.] Division of Forest Utilization, Taiwan Forestry Research Institute.；[2.] Department of Forestry, National Taiwan University.

In Taiwan, the strikes of typhoon usually result in branches bending and timber falling, which cause the forest gaps and changes of the tree species. Because of the forest gaps, the plant community contains different aspects in structure and physiognomy (1). All the tree species response differently to spectrum of solar radiation, so inside the forest the composition of light intensity and light quality is different. Besides, the light environment changes in different seasons and positions. All plants near the base of forest have to adjust their internal structure and physiological activities adapting to variant light environments for life endurance and reproduction. The purpose of this study is to investigate the changes of seedling growth and leaf morphology in different simulate light intensity on three kinds of native broad-leaved species: Ring-couple oak (*Cyclobalanopsis glauca*), Camphor tree (*Cinnamomum camphora*) and Formosan ash (*Fraxinus griffithii*). The simulate light intensities were indicated in relative light intensities which were 15%, 30%, 60% and 100%. Results showed that growth of these three species were affected by light intensities. The height, ground diameter, dry weight accumulation, Dickson seedling quality, stomatal density and leaf thickness of these three species were increased with light intensity. Therefore, the height of Camphor tree was decreased with light intensity. The ratio of chloroplast, starch grain and oil body area in palisade cell was increased with light intensity. But the amounts of chloroplast, starch grain and oil body in Formosan ash were decreased in high light intensity.

References

（1）Strauss-Debenedetti S. and F. A. Bazzaz 1991 Plasticity and acclimation to light in tropical Moraceae of different successionl positions. Oecologia **87**: 377-387.

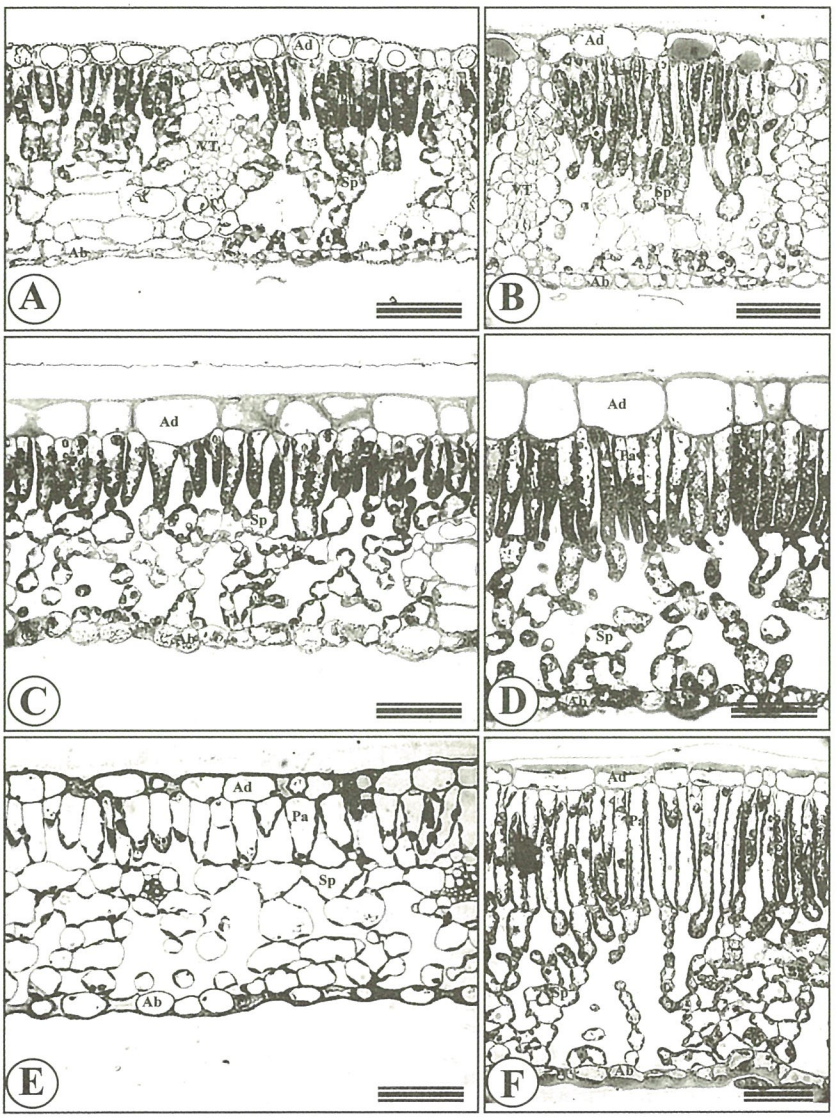

Fig. A and B The leaf cross section in relative light intensities on 15% and 100% of Ring-couple oak. (Bar = 50 μ m)

Fig. C and D The leaf cross section in relative light intensities on 15% and 100% of Camphor tree. (Bar = 50 μ m)

Fig. E and F The leaf cross section in relative light intensities on 15% and 100% of Formosan ash. (Bar = 50 μ m)

AL ALTERATIONS OF

HANG, Chia-Chi（張家綺）

g University, Taipei,

ippocampus after cerebral
e Mongolian gerbil,
se (350mg/kg, i.p.). The
ries occlusion by a
f ischemia, the aneurismal
allow reperfusion. At 0,
re perfused with 6%
r. After immersed the
d then embedded in the
ut with an ultramicrotome.
ned with glial fibrillary
hin sections were cut,
croscope.
he hippocampus had a
not discernible in the CA3
of the astrocyte lost its
ood vessel (Fig. 2). At 1
les in the cytoplasm in the
A3 and dentate gyrus. At
vacuoles in the cytoplasm.
and enlarged in the
he sham-operated.

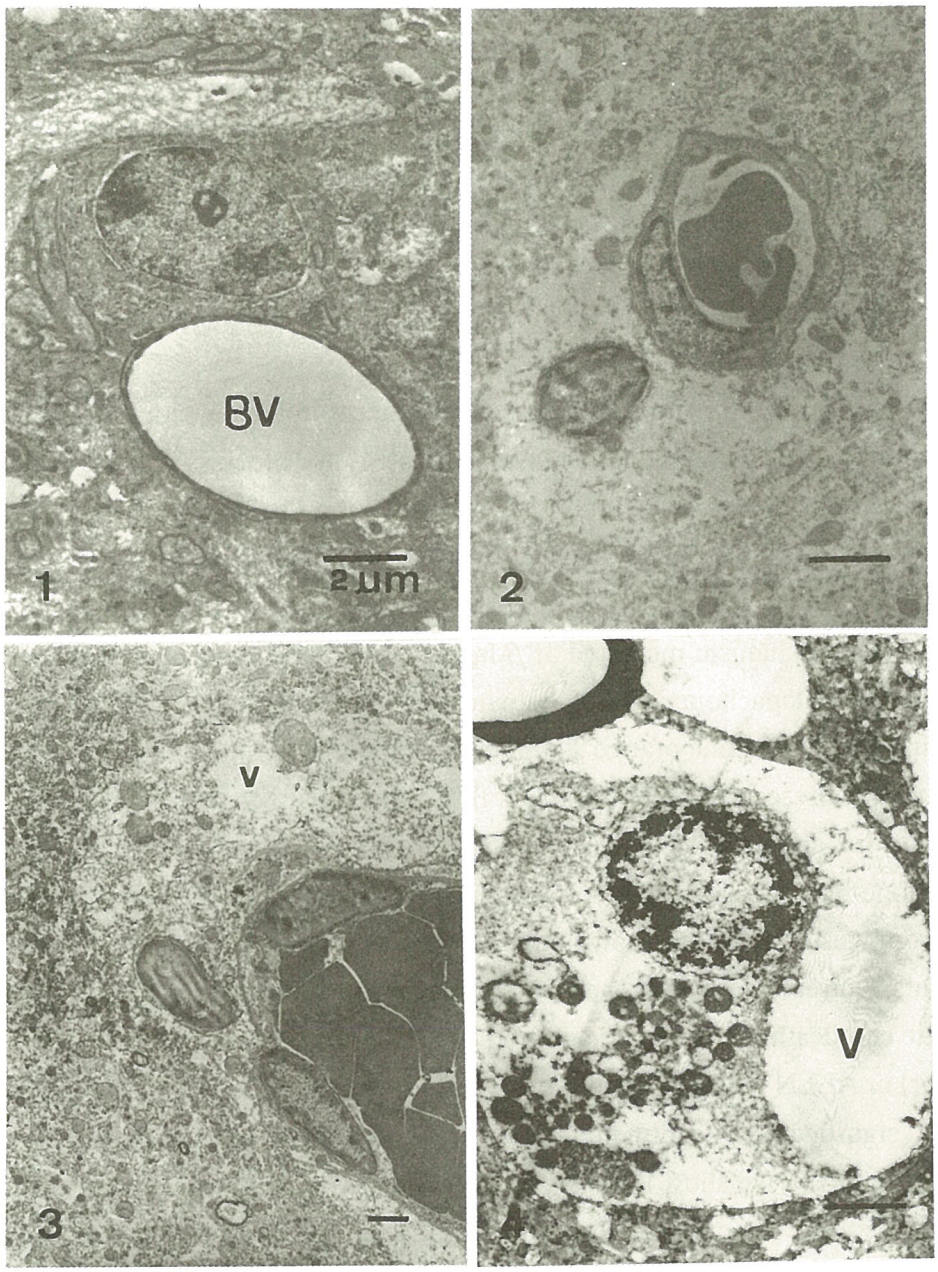

Fig. 1. Electron micrograph of the sham-operated animals.BV: blood vessel.

Fig. 2. Electron micrograph at the onset of reperfusion.

Fig. 3. Electron micrograph at 2 hours after reperfusion.V: vacuole.

Fig. 4. Electron micrograph at 6 hours after reperfusion.

Apoptosis induced by β-lapachone in human endothelial cells through Ca^{2+}-calpain dependent pathway.

Kung, Hsiu-Ni[1,2] (龔秀妮)* ; Yang, Li-Jyun[2] (楊利君) ; Lien, Yi-Chen[2] (連宜珍) ; Chau, Yat-Pang[2] (周逸鵬) and Lu, Kuo-Shyan[1] (盧國賢)

[1]Department of Anatomy and Cell Biology, School of Medicine, National Taiwan University, Taipei, Taiwan, R.O.C.

[2]Department of Anatomy and Cell Biology, School of Medicine, National Yang-Ming University, Taipei, Taiwan, R.O.C.

Since neovascularization is an essential process in the development of tumor, it is conceivable that anti-angiogenesis may be a strategy for blocking the growth of tumor. β-Lapachone (3, 4, dihydro-2, 2-demethyl-2H-naphtho-[1, 2-b] pyran-5, 6-dione), a natural product extracted from the lapachone tree (*Tabebuia avellanedae*), is a novel chemotherapeutic agent that has been shown to have anticancer and antiviral effects. However, the mechanism mediated of β-lapachone-induced cell death is unclear. Here we report that β-lapachone induced human endothelial cells underwent apoptosis determining with acridine orange staining, annexin-V labeling and propidium iodide uptaken by fluorescence microscopy and flow cytometry. Moreover, intracellular calcium influx and decrease of mitochondrial membrane potential (MMP) occurred in β-lapachone-induced apoptosis. Activation of calpain also involved in this process, result from western blotting showed that the large subunit of calpain cleaved into smaller fragments. Cotreatment with general caspase inhibitor zVAD-fmk failed to prevent apoptotic cell death. By contrast, addition of calpain inhibitors, ALLM (calpain II inhibitor) or ALLN (calpain I inhibitor), and intracellular calcium chelator, BAPTA, provided significant protection preventing apoptosis mediated by β-lapachone treatment.

In summary, we show that (1) β-lapachone mediated a unique proteolytic apoptotic pathway via calpain activation, and (2) calcium signaling and activation of calpain may play important keys in the mechanism of β-lapachone-induced human endothelial cell apoptosis.

Fig.1

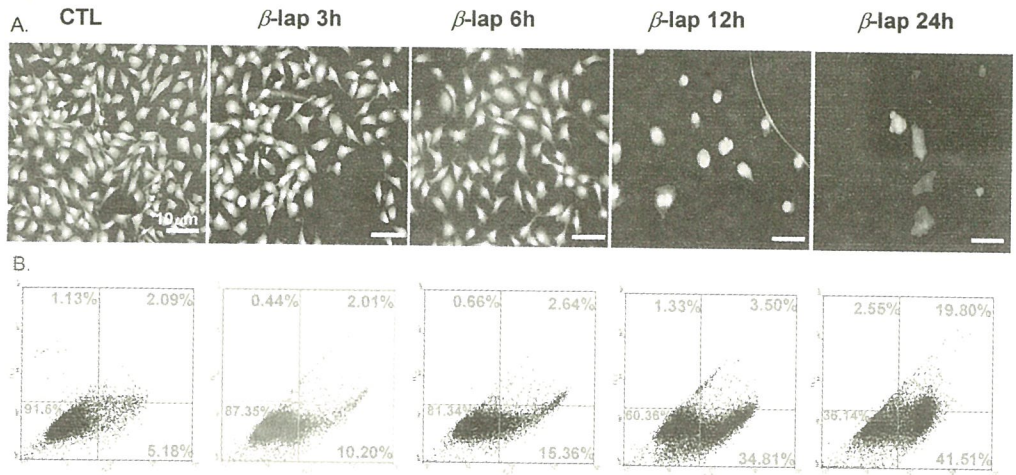

Fig. 2

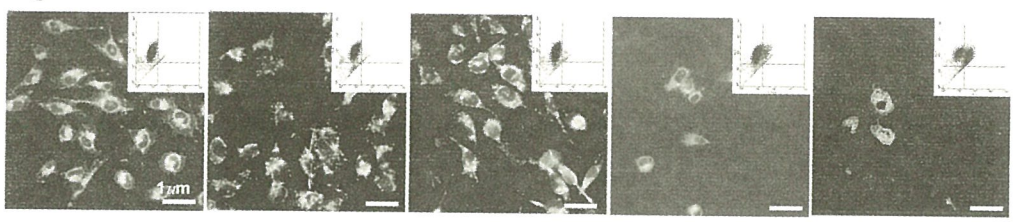

Fig.3

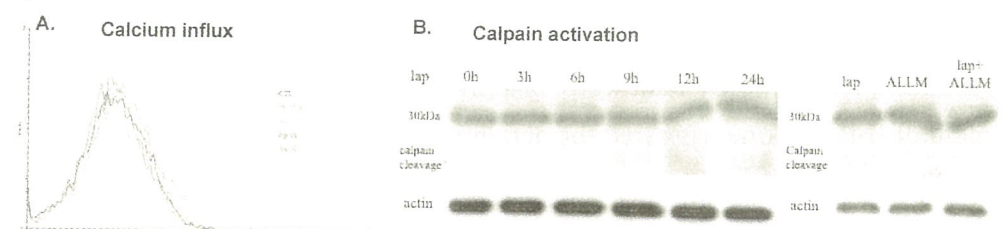

Fig. 4

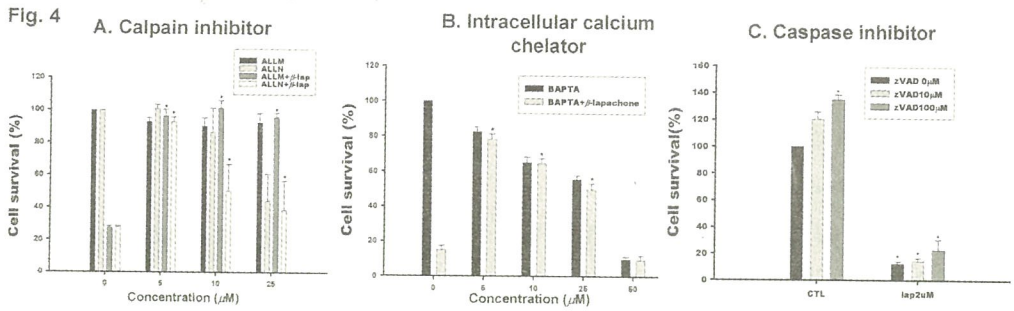

Fig. 1 Apoptotic analyses of endothelial cells after β-lapachone treatment . (A) AO stain and (B) Annexin-V/PI stain.

Fig. 2 MMP detection by JC-1 stain in endothelial cells following β-lapachone exposure.

Fig. 3 Apoptotic signaling in β-lapachone-mediated endothelial cell apoptosis. (A) calcium influx and (B) calpain activation.

Fig.4 Protection of endothelial cells from β-lapachone-mediated apoptosis by addition of (A) calpain inhibitor or (B) intracellular calcium chelator, but not of (C) caspase inhibitor.

Involvement of calcium signal and ERK, p38 and JNK activation in the mechanism of β-lapachone-mediated apoptosis on human prostate cancer cells

Lien, Yi-Chen (連宜珍)* ; Chau, Yat-Pang (周逸鵬)
Institute of Anatomy and Cell biology, School of medicine, National Yang-Ming University, Taipei, Taiwan, R.O.C.

Prostate cancer is the most commonly diagnosed neoplasm in western countries. However, this type of cancer is resistant to chemotherapy. Identification of anticancer chemicals for prostate cancer would be an important event. β-Lapchone (3,4,dihydro-2,2-dimethyl-2H-naphtho-[1,2-b]pyran-5,6- dione), a natural product extracted from the lapacho tree (*Tabebuia avellanedae*), has been shown to have anticancer and antiviral effects. In this study, we investigate whether β-lapachone exerts its cytotoxic effect to human prostate cancer cells (DU-145) and the signaling pathway underlies the mechanism of β-lapachone-mediated cell death. Our present results showed that cotreatment with general caspase inhibitor-z-VAD-fmk and calpain inhibitors, including ALLM or ALLN failed to prevent apoptotic cell death induced by β-lapachone. On the other hand, addition of NQO1 inhibitor (dicoumarol) or intracellular calcium chelator-BAPTA provided significant protection from apoptosis by preventing calcium efflux and calpain activation in DU-145 cells.Moreover, treatment of β-lapachone triggered the activation of ERK, p38 and JNK. Taken together, we suggest that the β-lapachone exerts its cytotoxic effect on DU145 cell line dependent on calcium signal and ERK, p38 and JNK pathways.

Fig. 1 Protection of HPC cells from β-lapachone-mediated apoptosis by addition of (A) NQO1 inhibitor or (B) intracellular calcium chelator ,but not of (C) caspase inhibitor and calpain inhibitor.

Fig. 2 Detection of calcium influx in HPC cells after β-lapachone treatment.

Fig. 3 Analyses of HPC cell apoptosis after cotreatment with BAPTA / dicoumarol and β-lapachone or treatment with β-lapachone alone by AO staining.

Fig.4 Calpain activation and ERK, p38 and JNK phosphorylation in β-lapachone-mediated HPC cell apoptosis .

Fig.1 A.

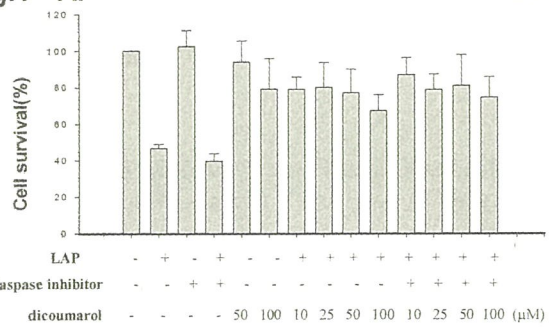

B.

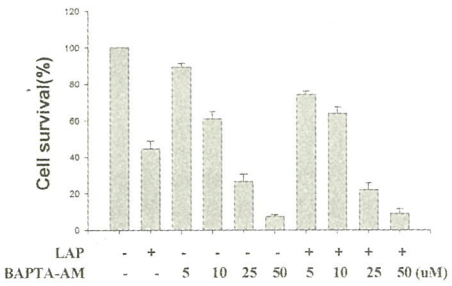

C.

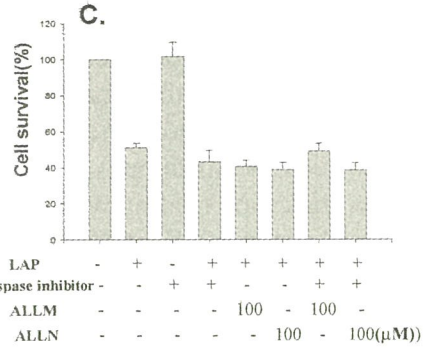

Fig.2

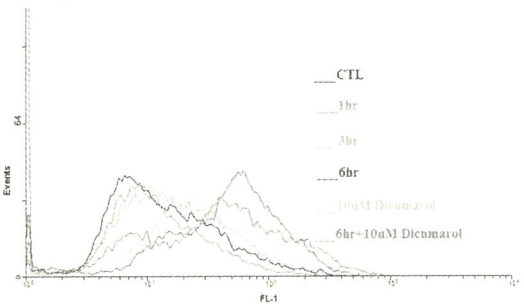

Fig.3

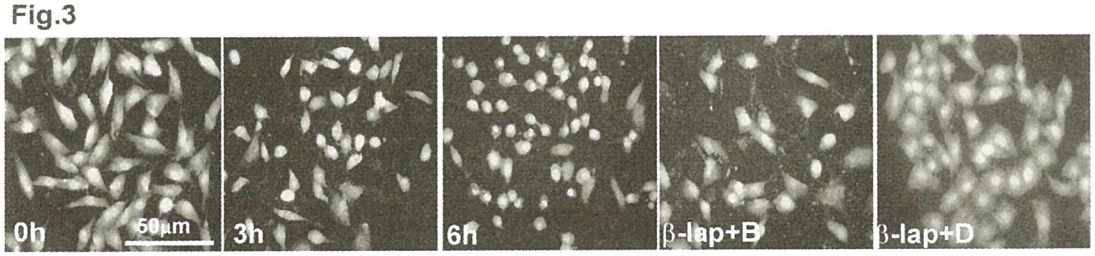

Fig. 4

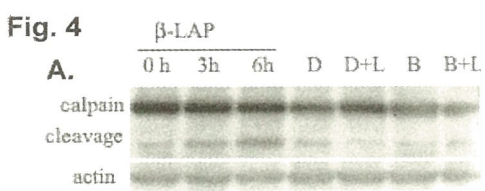

B.

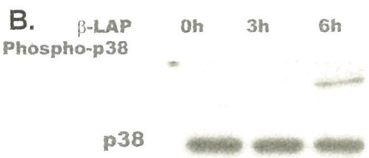

C.

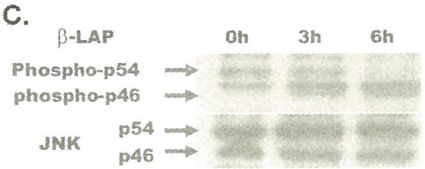

D.

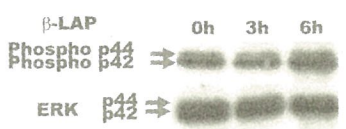

FINE STRUCTURAL OF POLLEN *NERVILIA* SPECIES IN TAIWAN

CHEN, Jenn-Yih(陳振義)[1];HSU, Hong-Kao(徐鴻皋)[2]and YEH, Mau-Shing(葉茂生)[1]

1 Department of Agronomy Science, National Chung-Hsing University, Taichung.
2 Department of Plant Pathology, National Chung-Hsing University, Taichung.

Nervilia is perennial plants of Orchidaceae. Totally fifty kinds, pertinence characters have reports but no relate to the fine structural of pollen In this studied, we collected 3 species: *N. plicata* (Andr.) Schltr., *N. aragoana* Gaud and *N. nipponica* Makino from Taiwan and observe pollens surface by SEM.

Fixed the specimens of anthesis. pick off the petals in 2.5% glutaraldehyde in 0.1M solution-phosphate buffer (pH 7.0) 3 hrs rinsed two times. in the same buffer added 5% sucrose each time 15 minutes, dehydrated in graded ethanol series (50,70,80,90,95,100%) 10 minutes each. Critical point dried the specimens, mounting the dried specimens on the stub with double- stick tape coating with gold (200nm). Observed with scanning election microscope (Topcon 150S) at 15 KV.

All of the collected species are similarity of appearances sizes and fold back strip figures on low. magnification (A.C.E) .Compare the fold back strip figures difference on high magnification (B.D.F). The *N. plicata* (Andr.) Schltr. have the largest of strip(B). *N. nipponica* Makino. have middle of strip (F). *N. aragoana* Gaud have the smaller of strip (D).The difference of the fold back strip structural on pollen surface were first report will could be the benefit for the taxonomy collate.

References：

(1)Argue, C. L. 1980 Amer. J. Bot. 67(1):68-87.
(2)Chen, S. J. and T. C. Huang. 1993. Taiwania 38:67-89.
(3)Hsiao, L. C. and C. S. Kuoh. 1995. Taiwania 40(3):299-316.
(4)Perez-Munoz, C. A, J. A. Jernstedt, and B. D. Webster. 1993a. Amer. J. Bot. 80:1183-1192.
(5)Perez-Munoz, C. A, J. A. Jernstedt, and B. D. Webster. 1993b. Amer. J. Bot. 80:1193-1202.

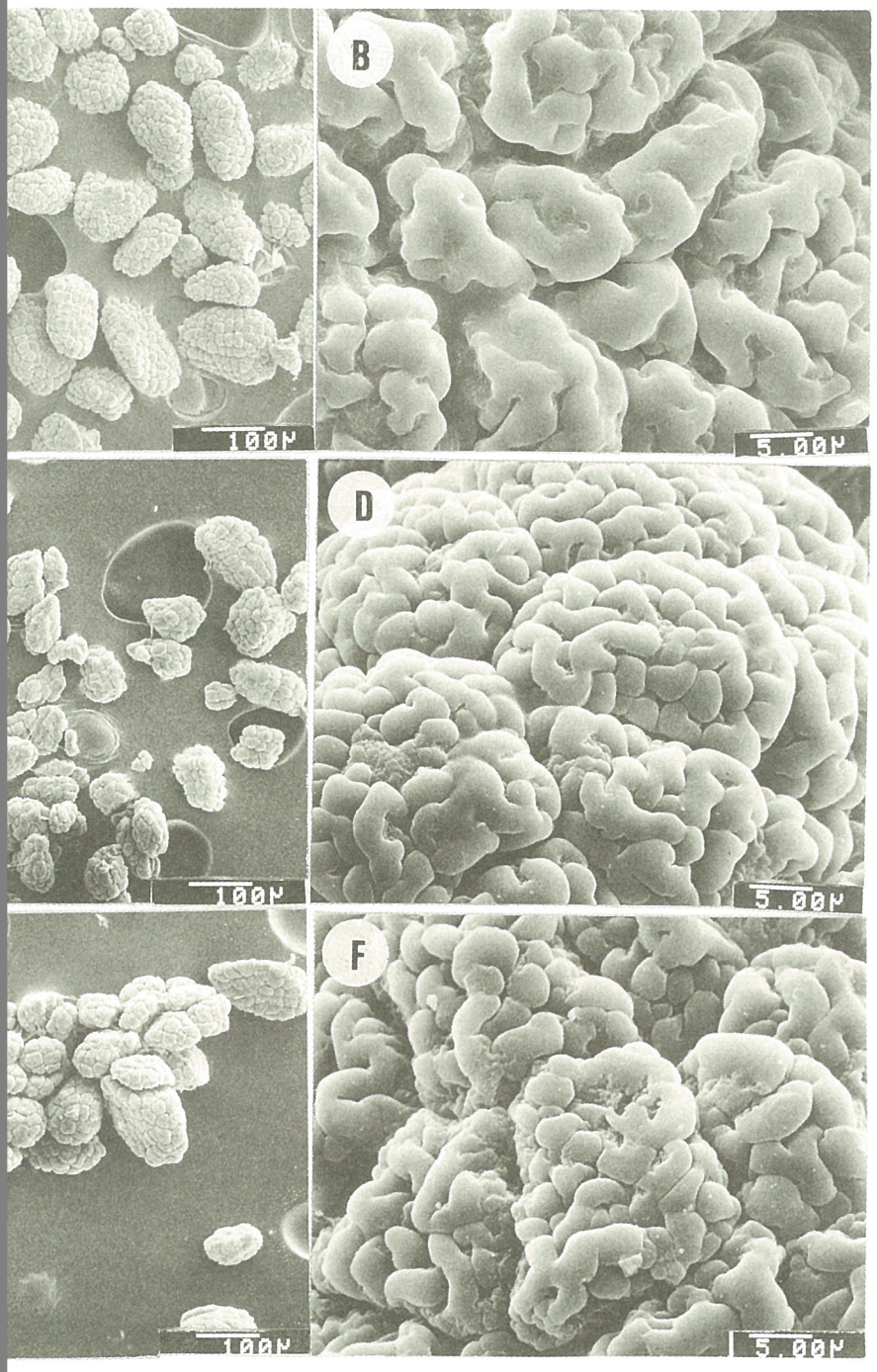

ural of pollen *Nervilia* species in Taiwan.
r.) Schltr.(100X bar=100μ) ; **B.** *N. plicata* (Andr.) Schltr.(2.00KX
aragoana Gaud(100X bar=100μ); **D.** *N. aragoana* Gaud(2.00KX
N. nipponica Makino (100X bar=100μ) ; **F.** *N. nipponica* Makino
μ)

EGG IDENTIFICATION OF MARINE FISHES, GROUPERS

HUANG, Jing-Duan [1] WU, Ching-Hsiang [1] LAIRD, Rebecca [2] DAWKINS, Roger [2] and YANG, Jui-sen [1]

1. Institute of Marine Biology, National Taiwan Ocean University, 202 Keelung, Taiwan
2. Center for Molecular Immunology and Instruments, The University of Western Australia, Australia

The kinds, composition, and density of marine fish egg are the basic information of fisheries biology and population studies. The identification of fish eggs became the important work in marine fish biology. Egg chorion ultrastructure has been studied by light and electron microscopy to provide useful characteristics in the identification of teleost fish eggs (Chen *et al.*, 1999; Li *et al.*, 2000). However, morphological ultrastractural feature is not sufficient to distinguish among every species of eggs. A cytochemical and molecular method would become another choice for the identification of fish eggs. Glycoproteins in fish egg chorions are involved as key components in the structural and functional organization of the chorion (Wassarman 1988). The glycoproteins in the chorions are a species-specific molecules and would be thought to be the first selected antigen materials for the antibody as the probe of egg identification. An immuno-probe againsta 97 KD glycoprotein in the egg chrion was developed for the identification of the egg of a grouper, *Epinephelus malabaricus*. The genome technologies were applied in studying the sperm receptor ZP3 of the groupers, *E. coioides* and *E. lanceolatus*. The gene-scanning profiles of the PCR products of grouper ZP3 showed a high species-specific character.

References:

1. Y. H. Li, C. C. Wu and J. S. Yang. 2000. J. Fish Biol. 56: 615-621.
2. L. Del Giacco, S. Diani and F. Cotelli. 2000. Dev. Genes Evol. 210(1): 41-46.
3. P. M. Wassarman, 1988. Ann. Rev. Biochem. 57: 415-442.

Fig. 1 *Epinephelus coioides* egg (a)and micropyle (b)

Fig. 2 *Epinephelus lanceolatus* egg (a)and micropyle (b)

Fig. 3 Gel scanning of PCR products of *Epinephelus coioides* ZP3

Fig. 4 Gel scanning of PCR products of *Epinephelus lanceolatus* ZP3

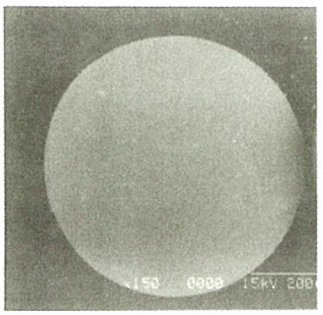

1a

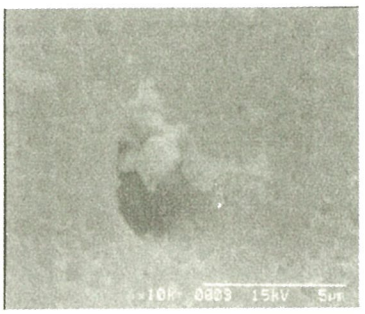

1b

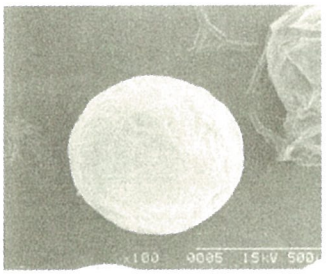

2a

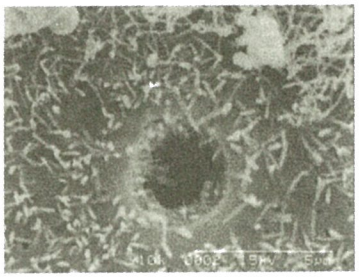

2b

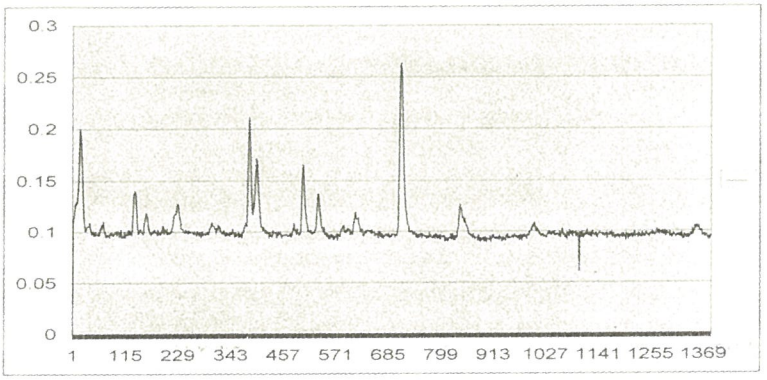
0.3
0.25
0.2
0.15
0.1
0.05
0
1 115 229 343 457 571 685 799 913 1027 1141 1255 1369

3

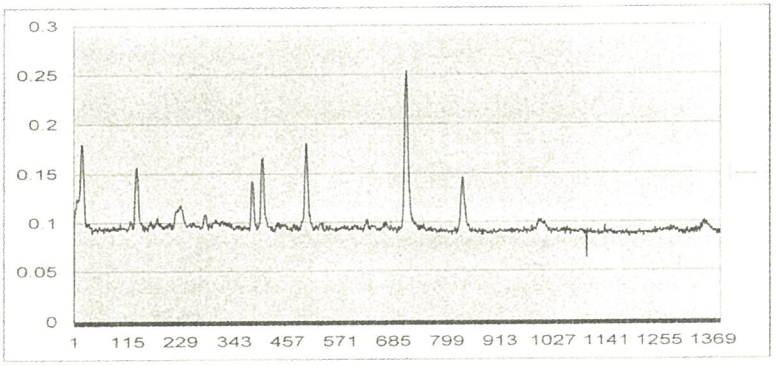
0.3
0.25
0.2
0.15
0.1
0.05
0
1 115 229 343 457 571 685 799 913 1027 1141 1255 1369

4

論文壁報展示

FABRICATION OF ELETROSTATIC PHASE PLATE IN TEM

Huang,Wei-Tsung (黃偉宗), Chen, Fu-Rong(陳福榮) and Kai, Ji-Jung (開執中)

Department of Engineering and System Science, National Tsing Hua University, Hsinchu, Taiwan 300, R.O.C.

ABSTRACT

The phase plate mechanism plays an important role in the high resolution of biological samples or the doping area of the materials with transmission electron microscope. Unfortunately, there are no proper methods to achieve the goal.

In light microscopy, the phase observation problem has been solved for a long time by Zernike. There have been several attempts to apply this technique to TEM, but most them are not be put into practice due to various problems such as charging, contamination, difficulties in positioning and fabrication.

Some use a thin, amorphous film of appropriate thickness with a small hole at the center that allowed the direct beam to travel through. However the phase shift of the electron wave could not be fully controlled due to variations in film thickness, charging, and unwanted scattering electrons. In order to construct a better phase plate, it is important to avoid using any materials in the pathway of the electron wave.

Our purpose is to fabricate an electrostatic phase plate which contains a ring electrode, shielded by earthed electrodes (see Fig.2). The phase shift, which is proportional to the potential integrated along the optic axis, is constant inside the ring. With the device in the back focal plane of the object lens (see Fig.1), we can construct a phase contrast electron microscope.

However, we use MEMS technology to produce the whole aperture holder with the phase plate on one aperture (see Fig.3).

REFERENCE

1. Ultramicroscopy Letter 63(1996)5-10, Akira Tonomura; Takao Matsumoto
2. Ultramicroscopy Letter 88(2001)243-252, Radostin Danev; Kuniaki Nagayama

Fig.1 The sketch of the electrostatic phase plate in TEM

Fig.2 upper shows the cross section of the phase plane which contains five layers. Three of them are electrode layers (gray) and two are insulators (red).

Fig.2 lower shows the plane view of the phase plate.

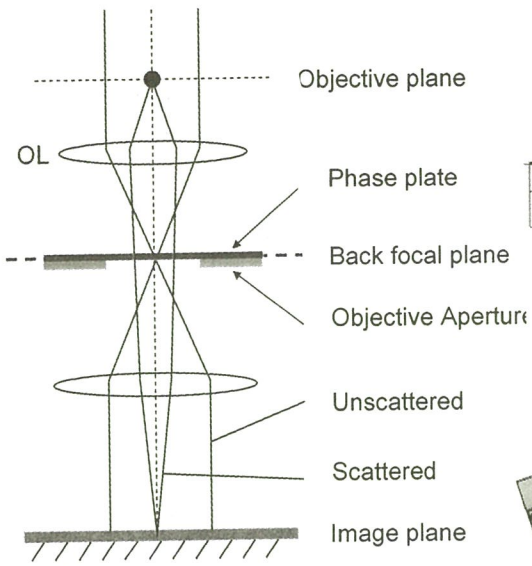

Fig.1

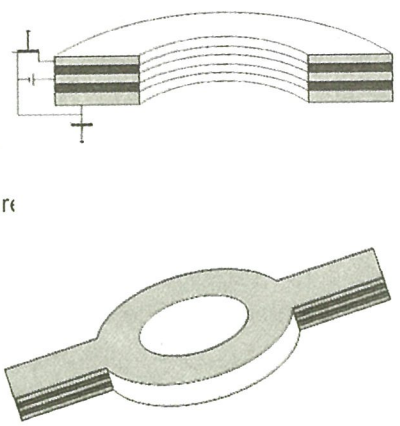

Fig.2

Fig.3 shows that we fabricate a holder with the phase plate to displace the JOEL aperture holder.

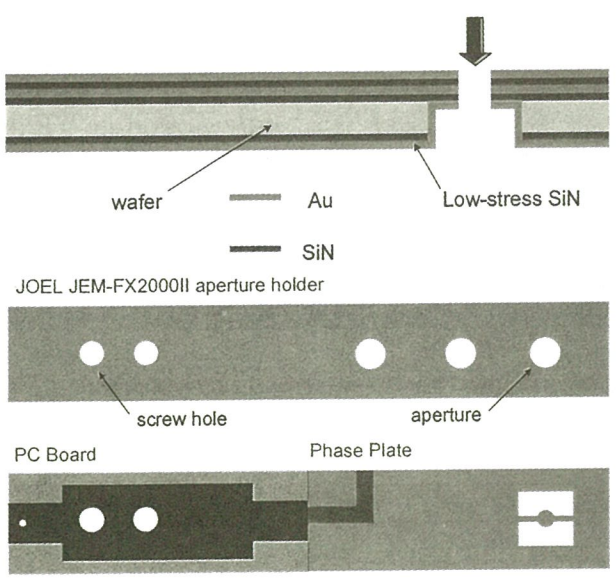

Vanadium oxide Nanowires for Electrochromic Devices

Cheng Keng-Jer(鄭耕哲), Kai Ji-Jung (開執中) and Chen Fu-Rong(陳福榮)

Department of Engineering and System Science, National Tsing Hua University, Hsinchu, Taiwan 300, R.O.C.

Electrochromic device are the most popular area of all swithcing technology. Thousands of patterns have been issued in last 3 decades. The major advantage of electrochromic materials are (1) they only require power during swithcing; (2) require a small voltage to switch(1-5v); (3) are specular under all conditions; (4) have continuous dimming; (5) have a long tern memory(12-48 hr). vanadium oxide has been widely investigated to use as starting and/or host material for fabrications of electrochromic device (ECD).

The growth techniques of vanadium oxide thin films have been had many reports, but studies on nanosize vanadium oxide are still rare. The benefit of using nanosize vanadium oxide is to shorten reaction time from minute order to second even milli-second order.

The growth method of nanowire is based on thermal evaporation of vanadium oxide powders (99.95%) without the present of catalyst. The vanadium oxide powders were placed at the center of Al_2O_3 boat and inserted in a horizontal tube furnace, where the temperature, pressure, and evaporation time were controlled. We kept the following parameter constant: (1) evaporation temperature, 650℃; (2) evaporation time, 8 hours; (3) chamber pressure,$3*10^{-3}$ Torr; (4) air flowing rate, 30 sccm. During evaporation, the products were deposited onto ITO glasses on an alumina plate placed at the downstream end of the quartz tube.

The deposited products were characterized and analyzed by scanning electron microscopy. Fig.1 showed the morphology of the vanadium oxide nanowires. The shape of the nanowires are column or belt like. The average dimension is 20+/-20 nm and length is up to 1 μm by the tunneling electron microscopy (TEM)(JEOL JEM-2000 FXⅡ) in Fig.2(a), and the high resolution TEM (HRTEM)(JEOL JEM-2010F Field Emission Gun TEM) show in Fig.2(b). The energy dispersive X-ray scattering(EDX) in Fig.3(a). The EDX data showed us the O and V peaks are too close to identify the component ratio. So we have to get X-ray diffraction (XRD) and TEM diffraction pattern to identify the structure. The growth of vanadium oxide is not controlled by the well known vapor- liquid- solid (VLS) mechanism instead of vapor-solid (VS) process. The morphology of vanadium oxide is very sensitive to the substrate temperature. The vanadium oxide electrochromic device showed in Fig.3(b).

Fig. 1 SEM image of vanadium oxide nanowires are on the ITO substrate .

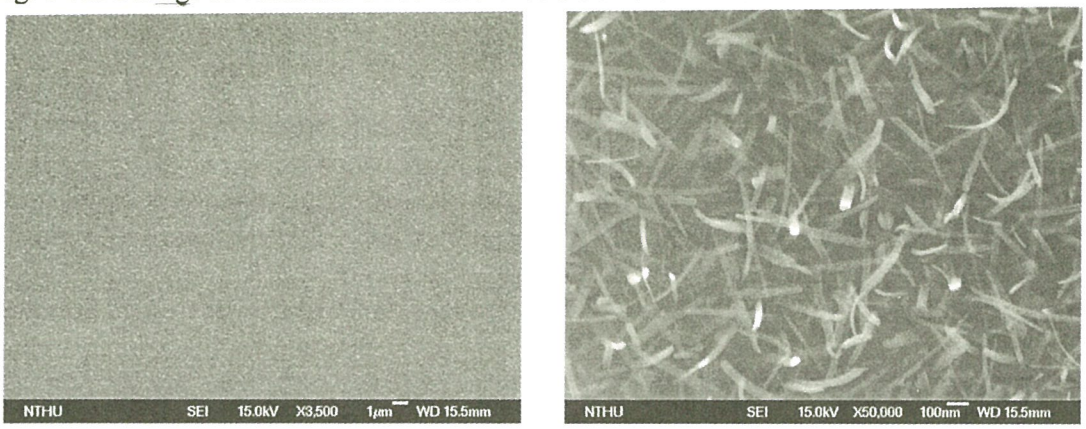

Fig. 2 (a)TEM image revealing the general morphology of the molybdenum oxide nanowires;(b) HRTEM image showing the structure detail of a nanowire.

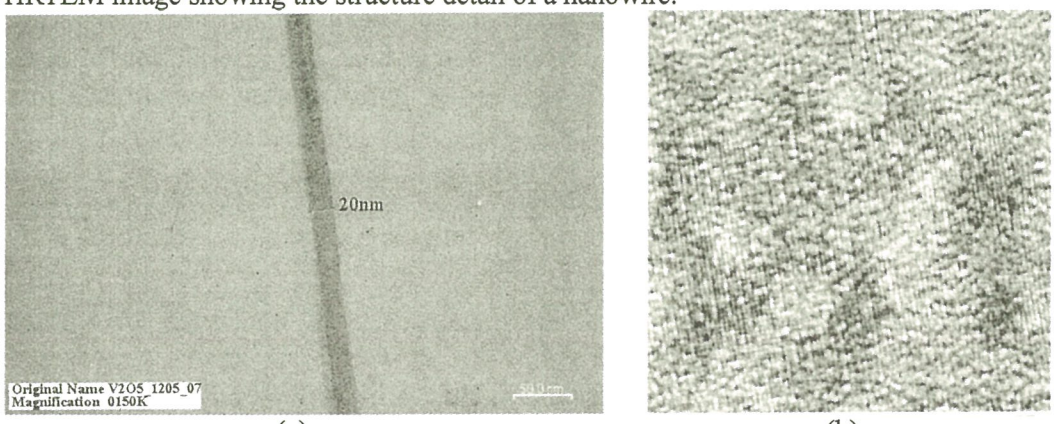

(a)　　(b)

Fig. 3(a) Energy dispersive X-ray spectroscope of single nanowire. Cu signal comes from the copper grid. (b) vanadium oxide electrochromic device.

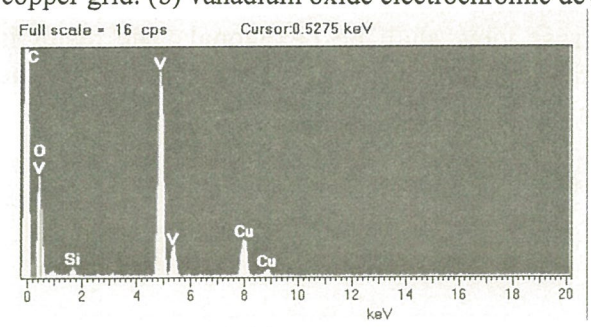

(a)

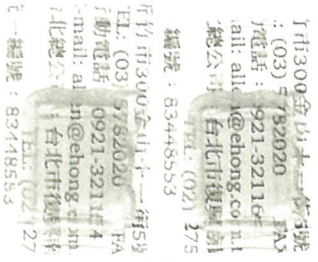

(b)

Zinc Oxide Nanowires Growth Controlled By Different Oxygen Pressure

Chen, Ko-Feng(陳科峯), Chen, Fu-Rong(陳福榮) and Kai, Ji-Jung (開執中)

Department of Engineering and System Science, National Tsing Hua University, Hsinchu, Taiwan 300, R.O.C.

1. Introduction

One-dimensional nanostructures such as carbon nanotubes and inorganic nanowires are expected for future application for electronic, optoelectronic, and nanoelectromechanical systems[1,2]. Fabrication of nanowires of Si, Ge, GaAs,InP and a variety of oxides has been reported[3]. Among these, zinc oxide (ZnO) has attached much attention because of its wide application for various optoelectronic devices. This material has a direct band gap of 3.3eV and a large exciton binding energy o f 6 0meV. Efficient e xcitonic U V l aser a ctions h ave b een d emonstrated at room temperature[4]. The understanding of the properties of this material is critical to successful device fabrication .We do a series of experiments to confirm the influence of oxygen pressure for fabrication of ZnO nanowires.

2. Experiment

The ZnO nanowires or nanorods were fabricated by the following procedure. The substrate (ITO glass) was cleaned by ethanol (C_2H_5OH), and then loaded on a quartz boat filled with metal zinc powder. The quartz boat was inserted into a quartz tube. The vertical distance between the zinc source and substrate was about 5 mm. The quartz tube was heated up to 450℃ under air ambient and then held this temperature for 2 hours. We changed the pressure of air (from 120Pa to 2200Pa,ie. Oxygen pressure from 24Pa to 440Pa) and then observed by scanning electron microscope(SEM).

3.Results

Fig.1~3 show the ZnO nanowires and nanorods grew under the air ambient 120Pa, 1800Pa, and 2200Pa respectively. The diameter of ZnO nanowires is increased with larger oxygen pressure. In Fig.2, the diameter of ZnO nanorods is about 200nm, and the tip of the ZnO nanorods is about 7nm. Because of the turn on field inverse to radius, it is beneficial for field emission. In Fig.3, cross view of ZnO nanorods looks like flowers. However, ZnO is Wurtzite structure and prefer orientation is (0001). Therefore, the cross view shall be hexagonal. The result is quite different with that, so it may be the unstable product, and we can identify the structure by TEM. It will be the big attribution for ZnO growth.

Reference

1.J. A. Hutchby, IEEE Circuits Devices Mag.,18,28(2002)
2.D. Routkevitch, IEEE Trans. Electron Devices,43,1646,(1996)
3.P. Yang, Int. J. Nanosci. ,1 ,1(2002)
4.P. Yang,Science,292,1897(2001)

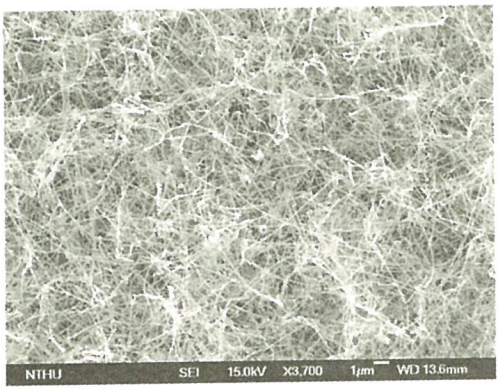

Fig.1(a)

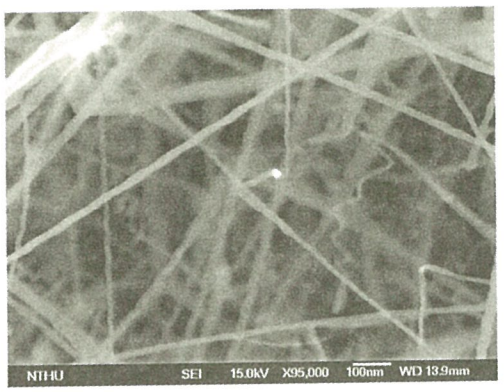

Fig.1(b)

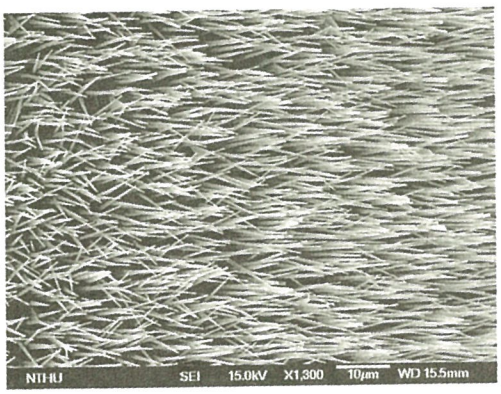

Fig.2(a)

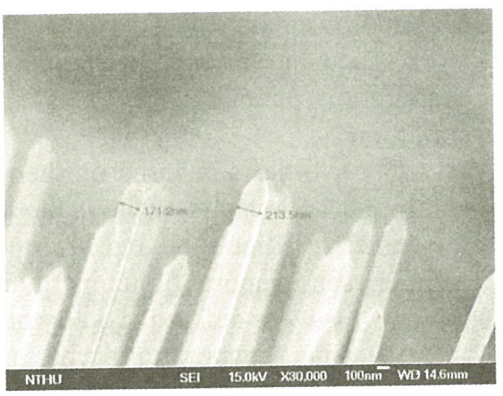

Fig.2(b)

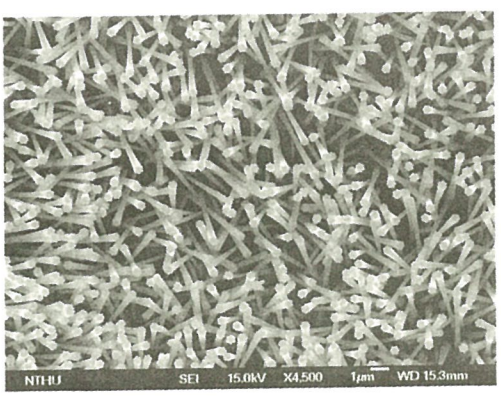

Fig.3(a)

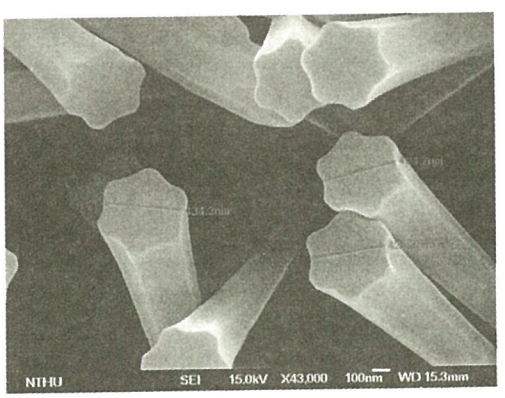

Fig.3(b)

Fig1~3 show the ZnO nanowires and nanorods grew under the air ambient 120Pa ,1800Pa and 2200Pa respectively. Fig.(b) is zoom out from the Fig.(a).

Zinc Oxide Nanorod Preparation by Thermal Evaporation Method

Lin, Sheng-Hui(林昇輝), Chen, Fu-Rong(陳福榮) and Kai, Ji-Jung (開執中)

Department of Engineering and System Science, National Tsing Hua University, Hsinchu, Taiwan 300, R.O.C.

Since the discovery of carbon nanotubes, one-dimensional nanomaterials have attracted global attention. one-dimensional nanomaterials reveal some novel characteristics that are different from those of the bulk materials and are great interest for potential nanodevice applications[1].

ZnO is a wide band-gap (3.37ev) compound semiconductor that is suitable for short-wavelength applications such as blue light and ultraviolet lasing. Besides, its exciton binding energy is~60mev at room temperature, substantially larger than that of ZnSe (22mev) and GaN(25mev)[2].

Much effort has been devoted to the development of the growth techniques for one-dimensional ZnO nanostructures[3]. Among the various methodologies, thermal evaporation method is favored for its simplicity and high quality products. In this work, Tacuchi experiment method was first used for choosing the adequate thermal evaporation parameters . Then fine tune these parameters to get the optimum condition.

Our synthesis is based on thermal evaporation of zinc powders (99.95%) under controlled parameters without the present of catalyst. The powders were placed at the center of silica tube and inserted in a horizontal tube furnace. Three parameters were chosen-evaporation temperature, argon gas flow rate, mole ratio of Ni/Zn. And three levels were defined. Totally nine experiments were carried out.

During evaporation, the products were deposited onto ITO glasses. The deposited products were characterized and analyzed by scanning electron microscopy (Fig 1). It revealed that ZnO nanowires are more vertical in high evaporation temperature and low Ar glow rate. But mole ratio of Ni/Zn didn't seem strong relation with nanowire structure. According to the Tacuchi's result, optimize the experiment parameters to get the vertical ZnO nanowire (Fig 2a). The dimension is about 500±50nm and length up to 2 μm. EDX indicated that the ratio of oxygen/zinc is about 0.82.

[1] Alireza Nojeh, Nano Lett 2003, 3, 1187.
[2] P. Yang, Adv. Mater. 2003, 15,353.
[3] Zhong L. Wang, Adv. Funct. Mater. 2003, 13, 9.

民國 93 年 01 月 17 日　　截稿日期：民國 92 年 12 月 18 日

Fig. 1 SEM images of zinc oxide nanorod in different condition.

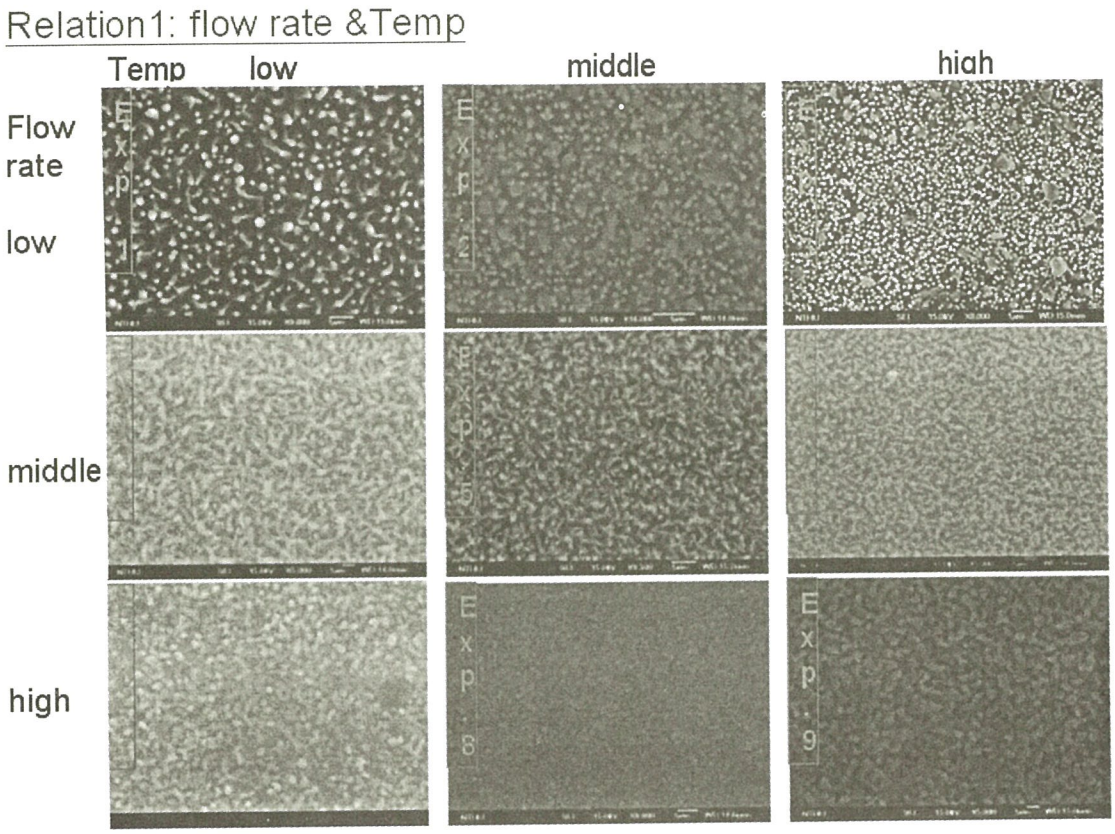

Fig. 2. A) SEM image revealing the general morphology of the vertical zinc oxide nanorods. B) EDX analysis.

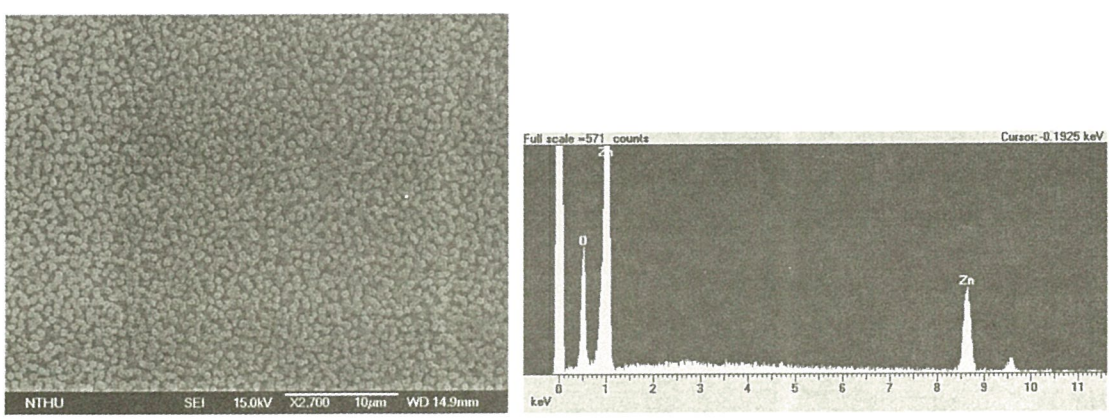

The study for Aluminum implanted Zinc Oxide nanowires.

Wu, Zong-Yi (吳忠益); Huang,Rong-Tan(黃榮潭);Jain,Wen-Bin(簡紋濱)
Chen, Fu-Rong(陳福榮) and Kai, Ji-Jung (開執中)

Department of Engineering and System Science, National Tsing Hua University, Hsinchu, Taiwan 300, R.O.C.

1. Introduction

ZnO is the promising candidate for future optical device such as the short wavelength light emitting, transparent conducting material due to wide bandgap (3.37ev) and high binding energy (60meV) larger than GaN (28meV) or ZnSe (19meV)[1]. Recently, ZnO nanowires have synthesized by vapor-phase transport process via the vapor-liquid-solid (VLS) mechanism [2] .In our study, we discover a new phenomenon that Al implanted ZnO nanowires became core-shell structure and the increasing diameter size followed the adding dose of Al.

2. Experiment

The powder of ZnO on the crucible was placed in the center of high temperature furnace, and the glass substrate with gold catalysts (40nm) was located at the downstream end of the furnace. The chamber was maintained at 200 Pa with a constant flow of pure Argon gas. Figure 1(a) shows the SEM image, ZnO nanowires were formed uniformly on the glass substrate after 12 hours growth.The samples were subsequently implanted Al^{+} ions at fixed energy of 20 keV and doses of 2×10^{16} cm^{-2}, 4×10^{16} cm^{-2} and 6×10^{16} cm^{-2}, respectively, as show in Fig.1(b.c.d).

3.Results

Figure 2 shows the TEM image of Al implanted ZnO nanowires. Apparently, the core-shell structure was formed. Figures 3&4 show the HRTEM images of the cross section structure of as-deposited and Al-implented ZnO nanowires. Compared Figs.3 and 4, core-shell structure was definitely existed in Al-implented ZnO nanowires. Besides, Al are most despersed on the peripheral of nanowire, that is, AlO_X surrounded the ZnO nanowire. The detail results will presented in conference.

民國 92 年 01 月 18 日　　截稿日期：民國 91 年　月　日

Fig. 1 SEM image of zinc oxide- nanowires are on the glass wafer substrate

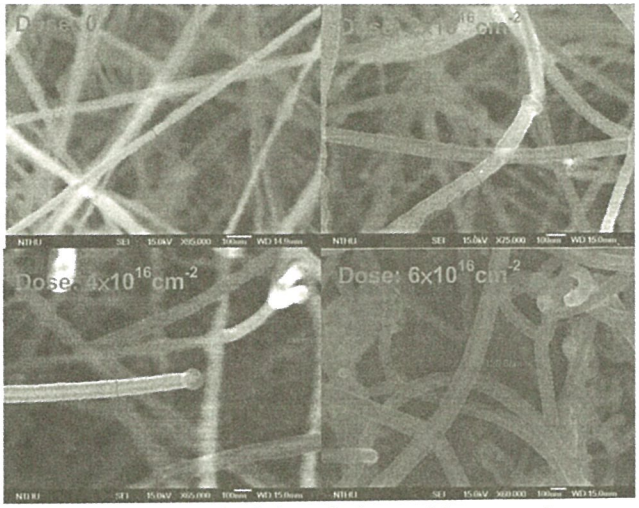

Fig .2 TEM image of Al doped zinc oxide nanowire.

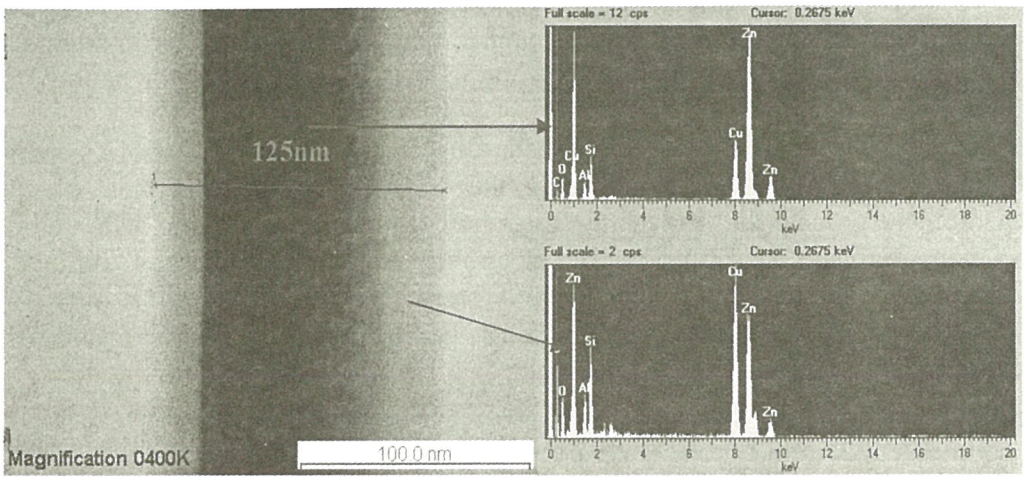

Fig.3 HRTEM image of the cross section structure of a zinc oxide nanowire .Fig.4 HRTEM image of the cross section structure of a Al implanted ZnO nanowire.

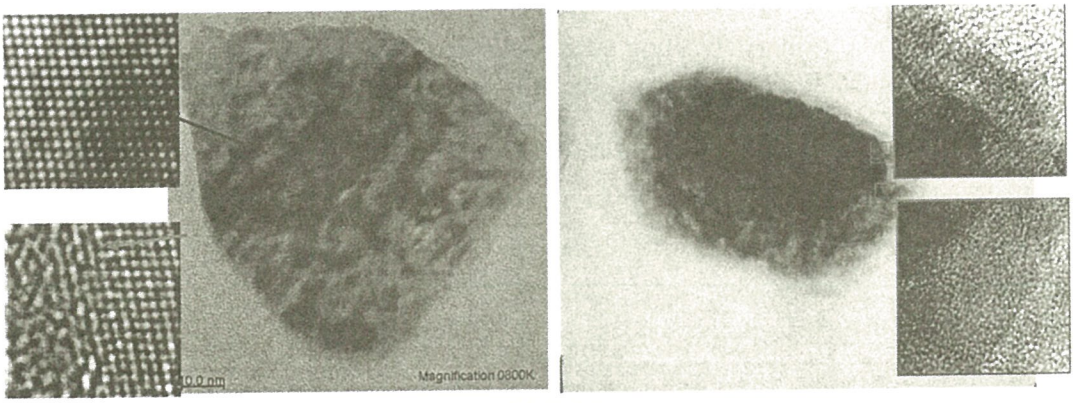

Elucidation of Nano-material Electrical Transport Properties by TEM-STM System

Liu, Yee-Lang(劉伊郎), Chen, Fu-Rong(陳福榮) and Kai, Ji-Jung (開執中)

Department of Engineering and System Science, National Tsing Hua University, Hsinchu, Taiwan 300, R.O.C.

Nano-materials have received considerable attention in recent years owing their unique properties from the bulk properties. However, conventional measurement instrumentation can not probe the nano-size particle, making it hard to obtain the electronic features. Such instrumentation can only acquire basic physical properties for regiment of nano-particles. However, obtaining the characteristics of individual nano-particles is still extremely difficult, especially for electronic property, a probe is necessary to contact with nano-particle, and the interference of the point contact between particle and probe is significant. As above, a parallel observation must be made during the measurement. In this manner, the transmission electron microscopy (TEM) and the scanning probe microscopy (SPM) is appropriate for nano-particle probing.

Based on the above, a nano-scale observation instrumentation system is required. It should be able to observe the variation of the specimen when the measurement process and can obtain the small signal from the nano-size materials. The conventional measurement of electronic transport properties applies the techniques of micro-electro-mechanical system (MEMS) to setup a micro-scale device and put the nano-materials on this device to obtain the characteristic of this material. But in this manner, the work needs a lot of time to prepare the device and the signals from point connect between the device and material is hard to define.

In this study, the I-V curve of RuO_2 and the other nanowires had been probed, the electronic properties could differ from the crystals. But there are also some problems need to be eliminated

[Ref.1] Guise,O.L.,Anher,J.W.,Jung etc.; Nano lett.2,191-193
[Ref. 2] Larsson,M.W.,Wallenberg,L.R. and Samuelson,L.;Microsco.and Microanal. 10,1-6

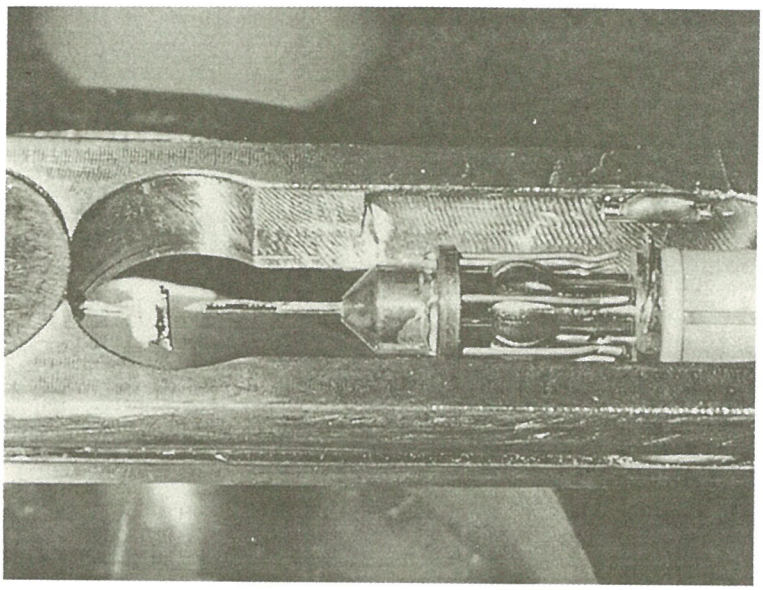

Fig. 1 STM system in the TEM holder

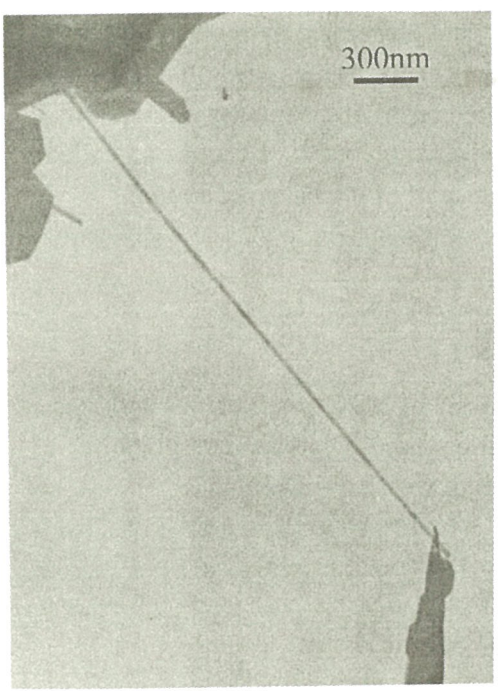

Fig. 2 TEM image of the tip contact with nanowire

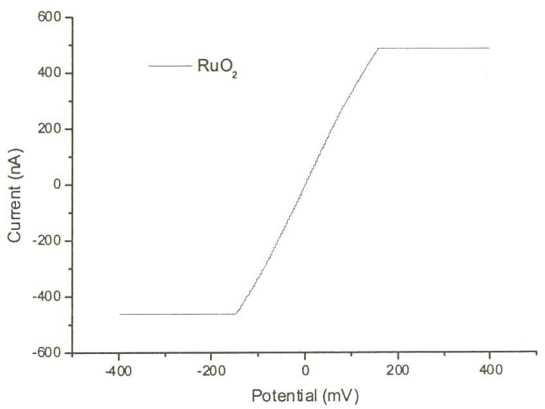

Fig. 3 I-V curve of RuO_2 nanowire

NSPORT OF

東福榮) and

a University,

in much of
nformation of
y samples of
ple, while the
erties, such as
through their
in the ability

of partially
ers, including
the intensity
ty derivative ,
the so-called
ation is

(a) and
crograph

94

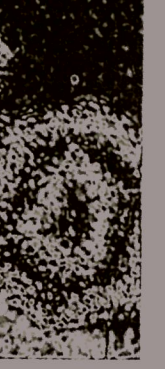

=-512nm, (b)
se,

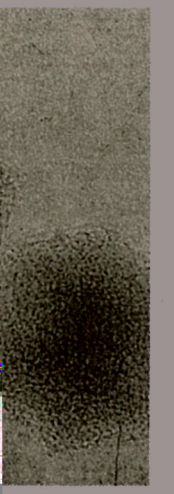

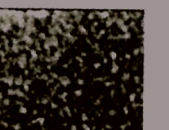

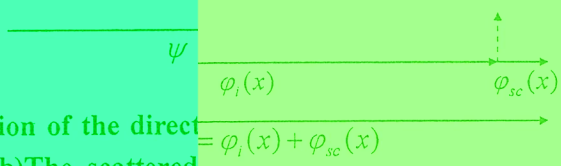

Fig. 1 (a)Vector addition of the direct
by $\pi/2$ or 90°. (b)The scattered
plate.[3]

wave φ_i and the scattered wave φ_{sc}
amplitude will shift 90° after inser

Thin film Phase Plate (Zernike Phase Pla

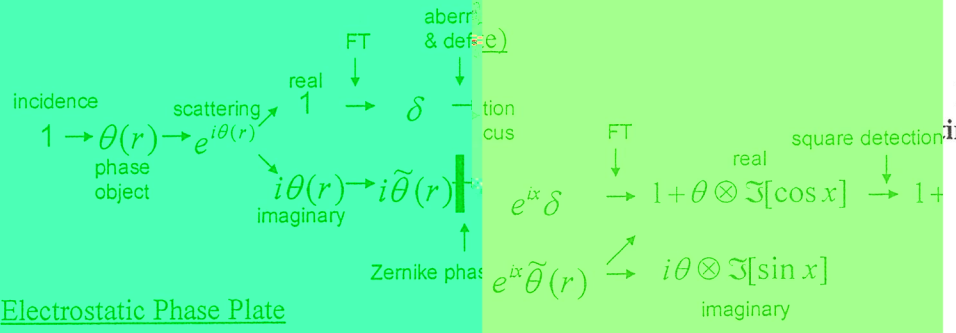

phase shifted
ing the phase

Electrostatic Phase Plate

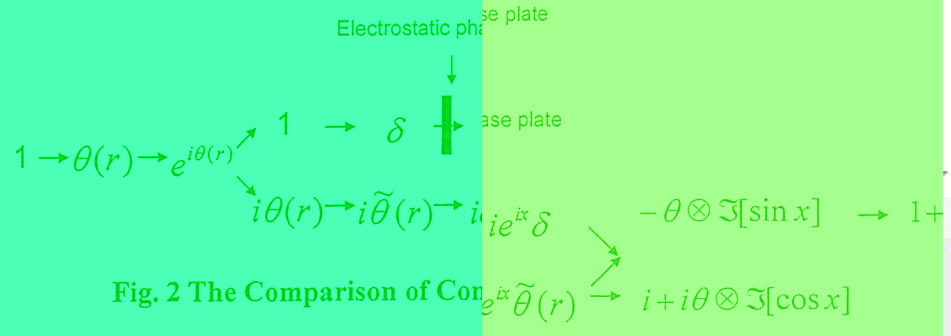

$I = \psi \bullet \psi^*$

$2\theta \otimes \Im[\cos x]$
real image

Fig. 2 The Comparison of Con

trast Transfer Mechanism of Weak C

$2\theta \otimes \Im[\cos x]$

bject

a. No Phase Contrast

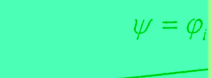

b. Phase Contrast

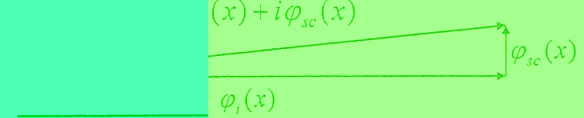

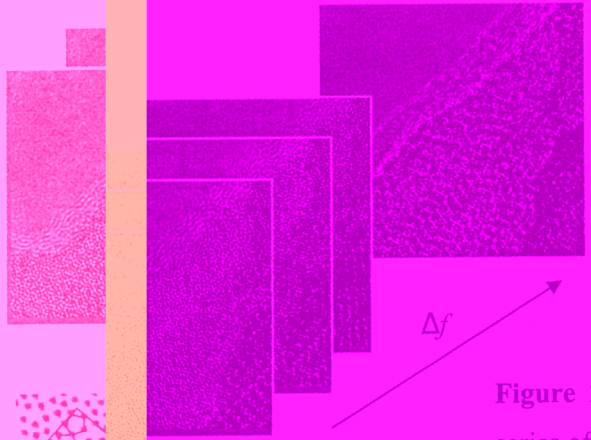

Figure 2. Scher
series of 30 expe

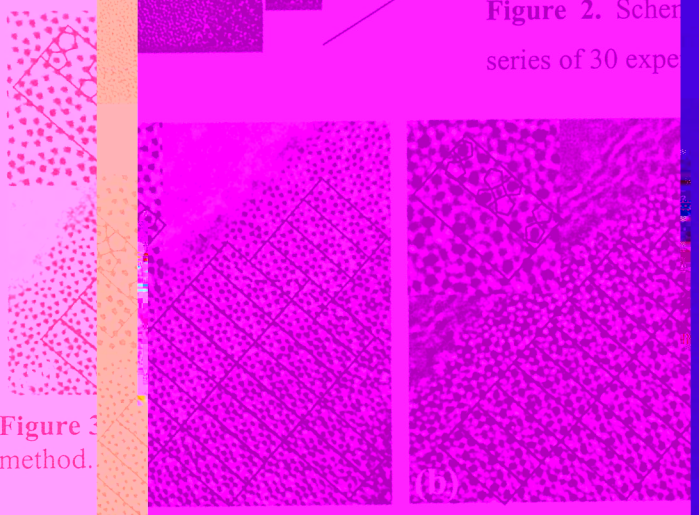

Figure 3
method.

Modulus and (b) phase of the restored exit wav
cell perimeters are marked in the full image ar

ocal

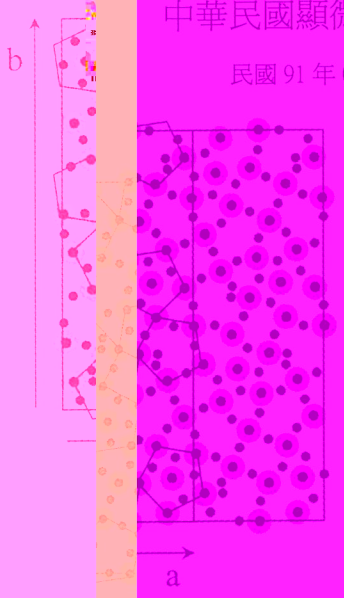

Figure 1. Two unit cells
$Nb_{16}W_{18}O_{94}$ viewed alon
represent cations (Nb, W
anions (O).

eft.

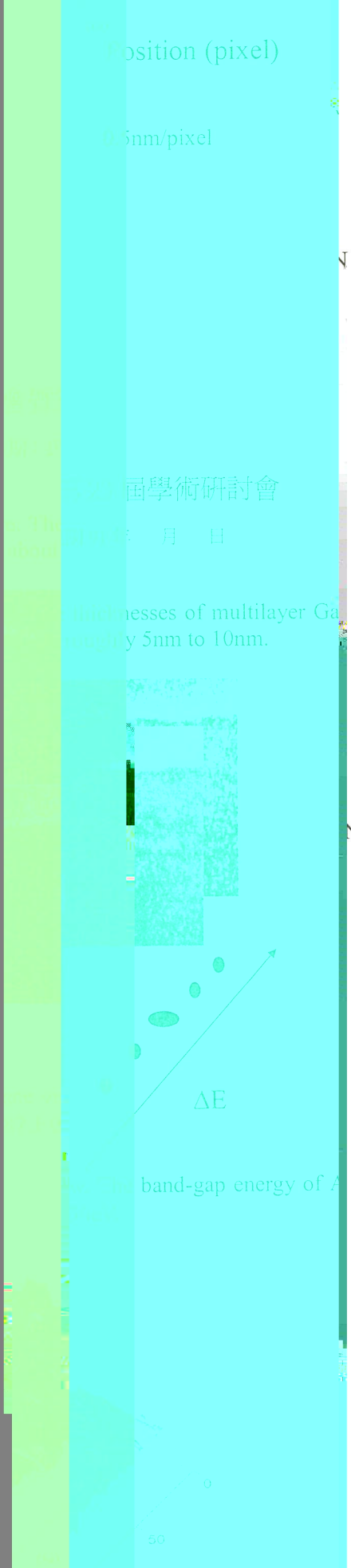
ΔE

INTERFACIAL CHARACTERISTIC STUDY OF MAGNETIC TUNNEL JUNCTION BY USING ENERGY FILTER TRANSMISSION ELECTRON MICROSCOPY

Huang, Rong-Tan [a](黃榮潭); Wu, Tien-Yuan [a](吳典原), CHEN, Fu-Rong [a](陳福榮)
KAI, Ji-Jung [a](開執中), Chang, Yin-Ming [b](張銀銘), and Lin, Minn-Tong [b](林敏聰)

[a] Department of Engineering and System Science, National Tsing Hua University, Hsinchu, Taiwan 300, R.O.C.
[b] Department of Physics, National Taiwan University, Taipei 106, Taiwan.

Energy Filter Transmission Electron Microscopy (EFTEM) was employed to characterize the local physical and electronic structure of FeO, α-Fe_2O_3, Fe_3O_4 and $CoFe/Al_2O_3/CoFe$ magnetic tunnel junction (MTJ). A double arctangent function background subtraction method [1] was improved and applied in MTJ. As we know the basic of energy electron loss spectrum [2], the spectrum will provide the distribution information of d-state electron of element at the L_3 and L_2 edge. It could represent the spectrum as followed type: Spectrum = background + two Lorentzian functions (L_3 and L_2). The background involved two parts: the continuous exponential decadency of the interaction between electron and substance, and 2p-state electron jump into unoccupied continuum state. The residual portion of the spectrum after subtract background will obtain the superposed result of two Lorentzian functions, i.e. the two function are the characteristic edges of L_3 and L_2. The L_3 and L_2 edge spectra are transitions from the $2p^{3/2}$ and $2p^{1/2}$ initial states to $nd^{5/2}$ and $nd^{3/2}$ final states [1]. We could evaluate the d hole number by integrating spectra intensity of L_3 and L_2 edges, as shown in Fig. 1(a)&(b) and Table 1.

As results of the EFTEM and four-point analysis, the MR ratio of MTJ was increasing with increasing annealing temperature up to 175 °C due to the improvement of uniformity and interface roughness between CoFe and Al_2O_3. However, the MR ratio was decreasing with the annealing temperature over 175 °C due to the degradation of element diffusion. Besides, by utilizing the double arctangent function background subtraction method, iron and oxygen would react and bond into FeO after 175and 200 °C, 30 min annealing. Moreover, the L_3/L_2 and

d hole ratio ($h_{5/2}/h_{3/2}$) increased with the elevating temperature, and the bonding state of iron oxide will approach to α-Fe_2O_3 at even more high temperature. The detail results will present at the conference.

REFERENCE:

1. P. A. van Aken, and B. Liebscher, Phys Chem Minerals, 29 (2002) 188.
2. C. Colliex, T. Manoubi, and C. Ortiz, Phys. Rev. B, 44 (1991)11402.

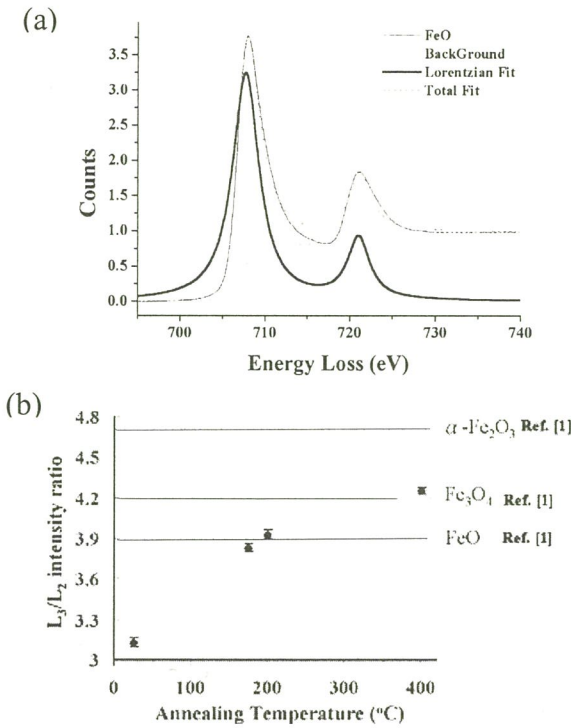

Fig. 1(a) The typical illustration diagram of the background subtraction process of iron oxide $L_{2,3}$ edge for 175 °C annealing.(b) The diagram of integrating L_3/L_2 spectra intensity ratio for different annealing temperature, in contrast to reference value.

Table 1

Sample	Ref. data (L_3/L_2)[1]	Exp. Data (L_3/L_2)
FeO	3.9	3.65
Fe_2O_3	4.7	4.65
Fe_3O_4	4.2	4.14

HRTEM Study of Helium Bubble Formation in SiCf/PyC/β-SiC Composites by Dual Beam Irradiation

T.S. Duh[a](杜定賢), K.M. Yin[b](殷開明), J. Y. Yan[b](顏精一), P.C. Fang[b](方伯傑), C.W. Chen[b](陳建文), F.R. Chen[b](陳福榮), J.J. Kai[b](開執中)
a:Institute of Nuclear Energy Research, Lung-tan, Tau-yuan 325
b:Center for Electron Microscopy, Department of Engineering and System Science, Nation Tsing-Hua University, Hsinchu 300

The formation of helium bubble in the advanced SiC composites, Tyranno-SA SiC/Py-C/β-SiC (TSA) and Hi-Nicalon Type-S SiC /Py-C /β-SiC (HNS), implanted with helium (He+, 2 MeV, 10000 appm) and irradiated by dual-beam (He+, 1.5 MeV, 1500/15000 appm and Si3+, 6 MeV, 10/100 dpa) was investigated in this study. The post-implantation annealing was carried out at 1000/1200/1400°C, and the dual-beam irradiation at 800/1000°C. For He implantation, the helium bubbles were observed clearly only in the SiC matrix in the case of annealing temperatures ≥ 1200°C. For dual-beam irradiation, no He bubbles were observed at dose of 10 dpa, but for doses up to 100 dpa, the He bubbles were observed in the matrix. Under these irradiation conditions, the TSA and HNS fibers showed a good microstructural stability against helium influence. In addition, diffusion modes that have been used for the diffusion of helium in nickel are suggested here to describe the diffusion behavior of He in SiC. Some of the experimentally observed behaviors of helium in SiC may be well understood in terms of these modes.

Helium Bubble Formation

Helium bubbles are formed by combining He atoms with vacancies, and most of them are formed at grain boundaries. The He diffusion mode in the case of forming He bubble should be via vacancy mechanism. Under irradiation the vacancy diffusion may be enhanced, and therefore might promote the He migration to grain boundaries. However the radiation-introduced defects, such as vacancy-clusters and cavities, may also trap the helium in the grain. Therefore, irradiation would not necessarily promote the formation of helium bubble on grain boundary. Under certain conditions, irradiation may suppress the formation of helium bubble in SiC. Experimentally, we can see the suppression effect on helium diffusion in SiC in this work and the other dual-beam study:

(1) For b-SiC after He implantation of 1000 appm at room temperature and annealing at 1050°C for 1 hour, helium bubbles were observed at grain boundaries already.

(2) The dual-beam result of this work, with irradiation condition of 10 dpa/1500 appm He at 1000°C, showed no helium bubbles in b-SiC (implying the suppression effect on helium diffusion in SiC).

(3) If the amount of free helium (i.e. the helium not trapped by defects) could increase, the helium bubbles might be formed in SiC. This may happen in the case of dual-beam irradiations with doses up to 100 dpa and helium grater than 6000 appm.

Post-Implantation Annealing

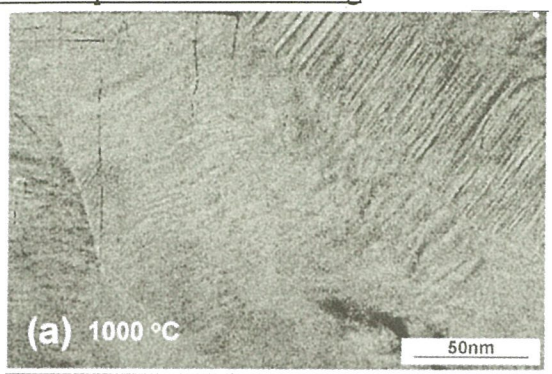

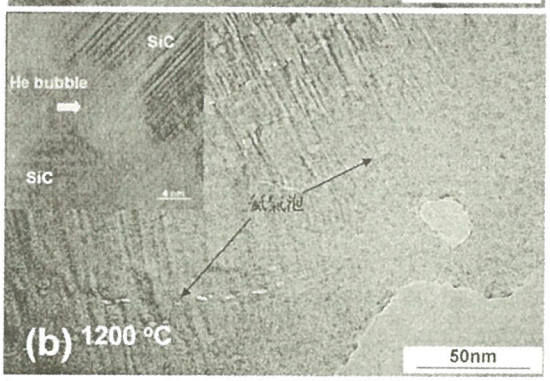

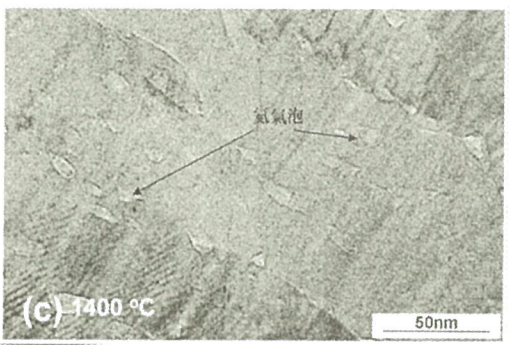

The helium bubbles were observed only in the matrix for annealing temperatures ≥ 1200°C, but for annealing temperature of 1000°C, they were too small to be observed clearly. Most of the helium bubbles accumulated along the grain boundaries. The average size of the helium bubbles was 3 nm for annealing at 1200°C, and 8 nm for annealing at 1400°C. None of the helium bubbles was observed in the carbon layers and fibers.

Dual Beam

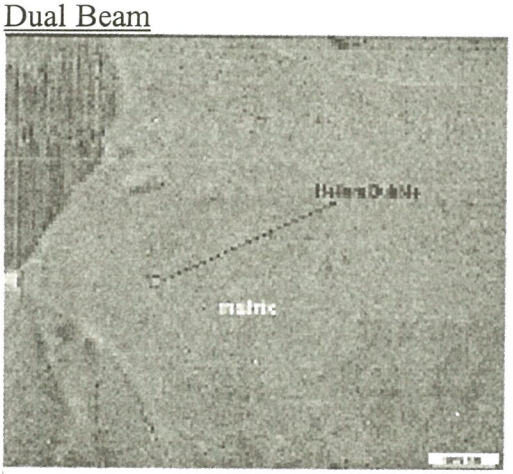

For dual-beam irradiation up to 100 dpa/15000 appm at an irradiation temperature of 1000°C, He bubbles were found in the matrix, but not in the fiber and carbon layer. For 10 dpa/1500 appm dual-beam irradiation, no He bubbles were observed in the SiC.

The improvement of HAADF image quality with wavelet de-noise method

YAN, Jing-Yi(顏精一); CHEN, Fu-Rong(陳福榮) and KAI, Ji-Jung (開執中)

Department of Engineering and System Science, National Tsing Hua University, Hsinchu, Taiwan 300, R.O.C.

Generally, the conventional transmission electron microscope (CTEM) is employed high coherent electron beam passing through the specimen and forms the image by the interference. According the image formation mechanism, the resolution is limited by the objective lens effect, defocus and dynamical scattering. Therefore, even employing shorter wave length source, the resolution is merely slight improved. The scanning transmission electron microscope (STEM) was invented by von Adenne [1]. The main feature of the STEM is moving the electron beam across the whole specimen and record all the scattered electron intensity to form the image. Generally, the image resolution of the STEM mode is restricted by the probe diameter. Howie proposed the high angle annular dark field (HAADF) detector to collect high angle elastic scattered electrons to form image [2]. Besides, the image contrast is determined atomic number without and phase problem. This is why HAADF imaging also called Z-contrast imaging. In this decade, HADDF STEM has become not only one of the most powerful tools to visualize material structure with atomic scale but also the candidate of sub-Å resolution microscope [3, 4]. Ideally, the relationship of the HAADF image and probe can be description by following formula in a non-dispersion approximation for localized Bloch states

$$I(R) = P^{eff}(R) \otimes O(R) \quad \text{.....(1)}$$

where $\otimes$ is convolution operation. $P^{eff}(R)$ and O(R) are denoted the PSF and objective function, respectively. The Figure 1 shows the diagram of the formation process. However, the electron beam current (intensity) is sacrifice when forming smaller probe size. The lower probe intensity will cause the obviously influence of noise in the Z-contrast image. Hence, the eq.(1) is not suitable for this situation due to the eq.(1) should be rewritten as:

$$I(R) = P^{eff}(R) \otimes O(R) + N(R) \quad \text{.....(2)}$$

where N(R) is the noise term. In this article, the wavelet de-noise method was employed to remove the additational noise and restore the image quality. The results are presented in the Figure 2.

Reference:

1. M. von Ardenne, Das elektronenmikroskop. Z. fur. Physik., **78**:318-339, 1988
2. A. Howie, Image contrast, J. Microsc. **117**:11, 1979
3. S. Lopatin, S. J. Pennycook, J. Narayan and G. Duscher, Z-contrast imaging of dislocation core at GaAs/Si interface, Appl. Phys. Lett., **81**:2728-2730, 2002
4. S. J. Pennvcook and L. A. Boatner. Nature. **336**:565. 1988

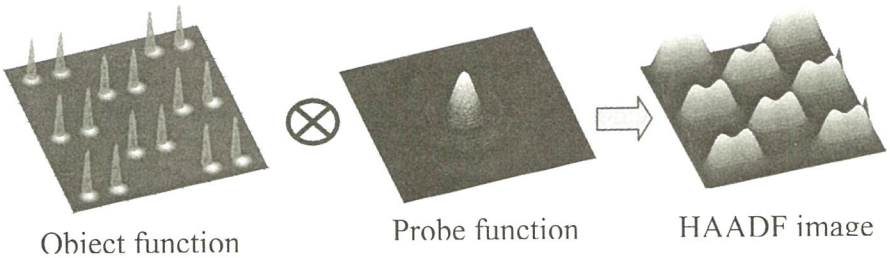

Figure 1: The diagram of STEM image formation

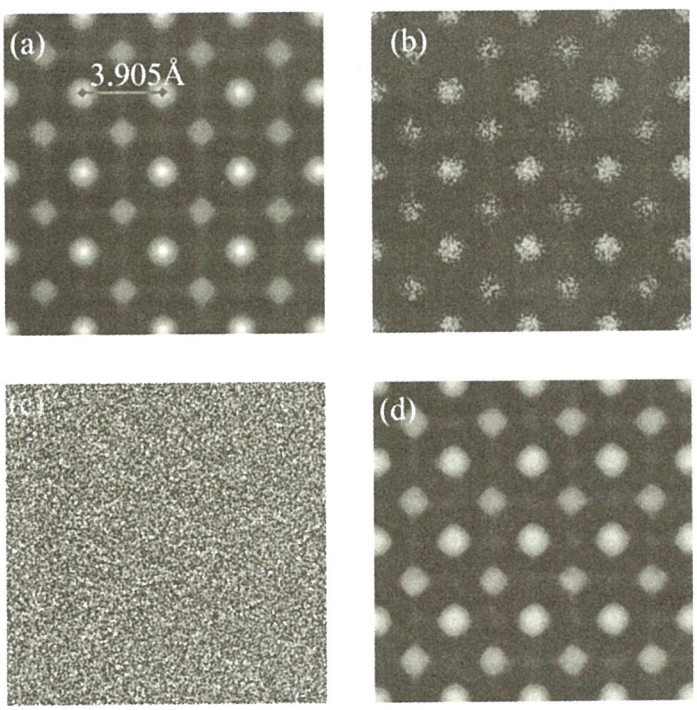

Figure 2: (a) Simulation $SrTiO_3$ [100] image (b) The noise added image (c) The removed noise (d) The de-noise image

The Study of Tungsten Oxide Nanowires Applied for Electrochromic Devices

Liao, Chia-Ching(廖家慶), Chen, Fu-Rong(陳福榮) and Kai, Ji-Jung (開執中)

Department of Engineering and System Science, National Tsing Hua University, Hsinchu, Taiwan 300, R.O.C.

Electrochromism, the reviersible change in optical properties when a material is electrochemically oxidized or reduced, has a long history of fundamental and practical interest. Commercial interest in electrochomism has centered around three main types of product : displays, mirrors and windows.

The WO_3 electrode is ubiquitous in electrochromic devices and is a common choise as the EC layer for electrochromic window. Tungsten trioxide is considered as the best cathodically-colored material. The electrochromic (EC) performance, reversible coloration of certain materials under double injection of ions and electrons, of transition metal oxides (TMO) such as tungsten oxide depends strongly on the nature and structure of these material.

The growth techniques of tungsten oxide thin films have been had many reports, but studies on nanosize tungsten oxides are still rare. In this paper, we have successfully grown the nanowire structure of tungsten oxide on the ITO glass substate and used it in the EC device.

Our synthesis is based on thermal evaporation of tungsten trioxide powders (99.9%) under controlled conditions without the present of catalyst. The desired oxide powders were placed at the center of and silica tube inserted in a horizontal tube furnace, where the temperature, pressure, and evaporation time were controlled.

The deposited products were characterized and analyzed by scanning electron microscopy in Fig.1 showed the morphology of the tungsten oxide nanowires and the cross-sectional view of the ITO glass substrate. It is apparently showed the shape of the nanowires are column like. We measure the average dimension and length which are 52±13nm and up to 5 μm by the tunneling electron microscopy (TEM)(JEOL JEM-2000 FXⅡ) in Fig.2(a). The high resolution TEM (HRTEM)(JEOL JEM-2010F Field Emission Gun TEM) in Fig.2(b) indicates the crystalline structure of the nanowires prepared in our experiment. On the other hand, we identified the composition of the nanowires in energy dispersive X-ray scattering (EDX) in Fig.3.

Finally, we have made a electrochromic device (ECD) used the tungsten oxide nanowires as the EC layer. Fig 4. show the ECD can be converted from transparent into deeply blue colored by proton (or cation) injection from a suitable electrolyte or ion conductor.

trate; and the

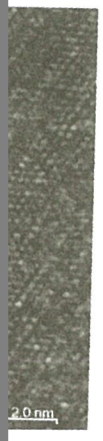

anowir ; (b)

ice.

EFFECT OF Zr IN CAST HIGH-ENTROPY 10-COMPONENT AlTiVCrFeCoNiCuZrMo (Mo-10) ALLOY

Huang, Hung-Hsiang[1], Hsu, Tung[1], and Chen, Swe-Kai[2]

[1] Department of Materials Science and Engineering, National Tsing Hua University, Hsin-Chu 300, Taiwan
[2] Materials Science Center, National Tsing Hua University, Hsin-Chu 300, Taiwan

INTRODUCTION

High entropy alloys, unlike conventional alloy composed of several components with one or two dominant elements, contains equi-mole fraction component elements. The Gibb's free energy with large and negative value at high temperatures, due to large and negative value of $T\Delta S$, results in the name of "high entropy alloy." Some microstructure characteristics of AlTiVCrFeCoNiCuZrMo alloy (Mo-10) and AlTiVCrFeCoNiCuMo (Mo-9) alloy are reported.

EXPERIMENTAL

Both Mo-10 and Mo-9 alloys were made by arc-melting in a water-cooled copper mold with Ar atmosphere protection. Purities of all constitutional elements are above 99%. As-cast samples were polished, etched with aqua regia and then observed with the scanning electron microscope (SEM). Elemental analysis was also performed on the SEM/EDS instrument. The crystal structures were determined by X-ray diffraction (XRD).

RESULTS and CONCLUSION

Fig.1 is the XRD patterns of Mo-10 and Mo-9. Mo-9 has only one BCC (a=2.945 Å) phase, whereas Mo-10 has one BCC (a=3.004 Å) and one FCC (a=4.25 Å) phases. Fig. 2 is the typical dendritic structure of Mo-10, in which the light dendrite is Mo-, V-, Cr-rich phase while the dark interdendrite is Zr-, Fe-rich. A third phase, the gray nodular areas are Ni-, Al-, Ti-, Cu-, Co-rich. The SEM image of Mo-9 (Fig. 3) also shows three phases, but the dendritic structure is less prominent than that in Mo-10. Figs. 4 and 5 are higher magnification SEM images of Mo-10 and Mo-9, respectively.

ACKNOWLEDGEMENT

We thank the support by NSC grant No. NSC-92-2120-E-007-010.

REFERENCES

1. Chang, C.W., and Hsu, T., and Chen, S.K., Proceedings of the 23th R.O.C. Symposium on microscopy, Jan 2003, M-P-5
2. Yeh, J.W., Lin, S.J., Hsu, T., Gan, J.Y., Chen, S.K., Shun, T.C., and Chiao, C. W., "Novel Materials for the New Century," in Proceedings of the Congress, Chinese Institute of Mining and Metallurgy Engineering, Taipei, Nov. 2002, pp. 13-24.

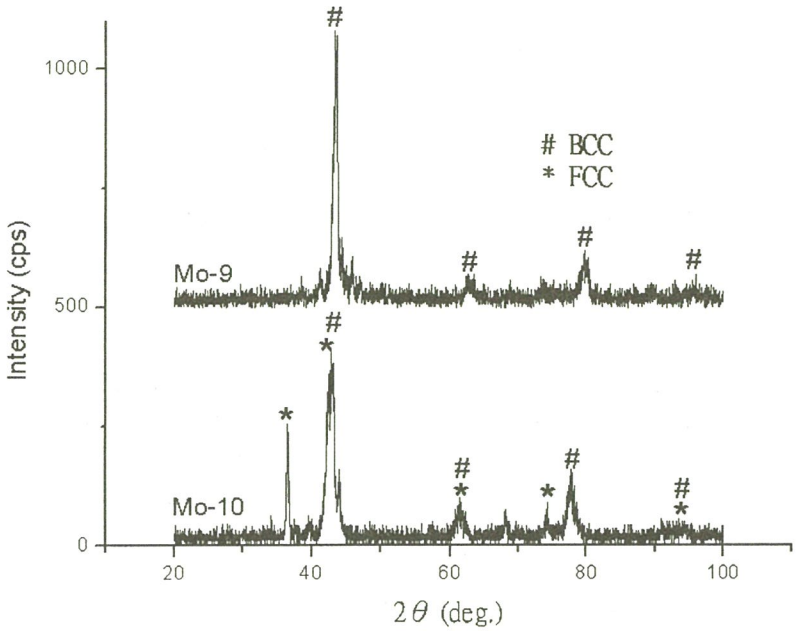

Fig. 1. XRD patterns of as-cast Mo-10 and Mo-9 alloys.

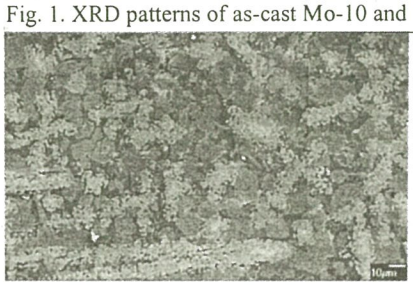

Fig. 2. SEM image of the etched Mo-10 alloy.

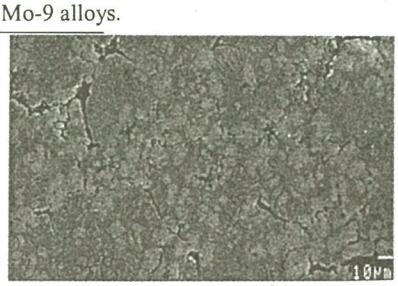

Fig. 3. SEM image of the etched Mo-9 alloy.

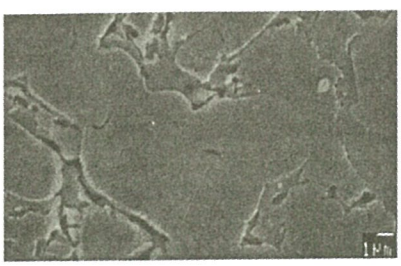

Fig. 4. SEM image of the etched Mo-10 alloy.

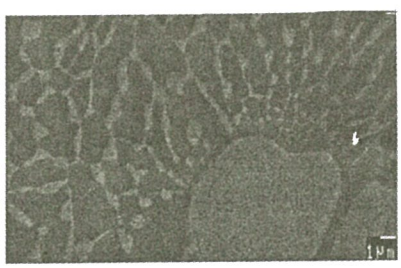

Fig. 5. SEM image of the etched Mo-9 alloy.

EFFECTS OF Cr DOPING ON THE MICROSTRUCTURE AND FERROELECTRICITY OF $Bi_{3.25}La_{0.75}Ti_3O_{12}$ FILMS

CHANG, Tian-Lin (張天麟) and LIN, Wen-Tai (林文台)

Department of Materials Science and Engineering, National Cheng Kung University, Tainan.

Ferroelectric thin films have attracted great interest in recent years for applications in integrated nonvolatile ferroelectric random access memories. $(Pb,Zr)TiO_3$ thin films with Pt electrodes show severe polarization fatigue during electric field cycling. Recently, it was reported that $Bi_{3.25}La_{0.75}Ti_3O_{12}$ (BLT) thin films with Pt electrodes show good fatigue endurance and larger ferroelectricity.[1] Incorporation of higher-valent cations such as V^{5+} and W^{6+} into the Ti^{4+} site of BLT lattices can reduce the amount of oxygen vacancies and thus result in an increase of remanent polarization ($2P_r$).[2] The ionic radii of Cr^{6+}, 0.044 nm, is much smaller than that, 0.0605 nm, of Ti^{4+}, dissatisfying the tolerant factor for forming a substitutional solid solution of $(Bi_{3.25}La_{0.75})(Ti_{3-x}Cr_x)O_{12}$ ($BLTC_x$), therefore, it is interesting to explore the effect of Cr doping on the ferroelectricity of BLT films.

The $BLTC_x$ films with 10 mol% excess Bi were fabricated on Pt(100 nm)/Ta(7.5 nm)/SiO_2/Si(100) substrates using a chemical solution deposition (CSD) method. The Pt/Ta multilayer was deposited by electron-gun evaporation. The $BLTC_x$ and Bi_2O_3 precursor solutions were spin coated onto the substrates at 4000 rpm for 30 s, respectively. The thickness of the $BLTC_x$ films was about 250 nm. The Pt/$BLTC_x$/Pt capacitors were annealed at 750℃ for 10 min in air.

Figure 1 shows the change of $2P_r$ as a function of the Cr concentration (x) in the $BLTC_x$ films. The $2P_r$ of $BLTC_x$ films decreases from 30 $\mu C/cm^2$ at x = 0 to 9.2 $\mu C/cm^2$ at x = 0.03. XRD analysis showed that no second phase was formed in the $BLTC_{0.03}$ films and the lattice constant of $BLTC_{0.03}$ was somewhat smaller than that of BLT films, indicating that Cr ions were substitutionally incorporated into the Ti site of the BLT lattice. The SEM micrographs in Fig. 2 show that as the Cr concentration (x) was increased up to 0.03 the shape of some grains changed from rod to plate, indicating the formation of c-axis preferred orientation. BLT films have a large and a quite small polarization along the a and c axes, respectively. Furthermore, the remained rod grains became slim. The decrease of grain size can enhance the domain pinning effect, resulting in polarization suppression. In addition, the doping of smaller-radius Cr^{6+} into the Ti^{4+} site of the BLT phase may reduce the distortion of the TiO_6 octahedra, resulting in the decrease of $2P_r$. On the other hand, the doping of higher-valence cation Cr^{6+} into the Ti^{4+} site of BLT phase can reduce

the amount of oxygen vacancies in the films and thereby mitigate the pinning effect of oxygen vacancies on the domain walls and grain boundaries, resulting in a larger $2P_r$. In the present study, therefore, upon Cr doping the effects of reduction of the grain size and formation of the c-axis preferred orientation are dominant over that of reduction of the amount of oxygen vacancies, resulting in the degradation of the $2P_r$ of BLT films.

1. Park, B.H., Kang, B.S., Bu, S.D., Noh, T.W., Lee, J., and Jo, W.; Nature, 1999 (401) 682.
2. Noguchi, Y and Miyayama, M.; Appl. Phys. Lett., 2001 (78) 903.

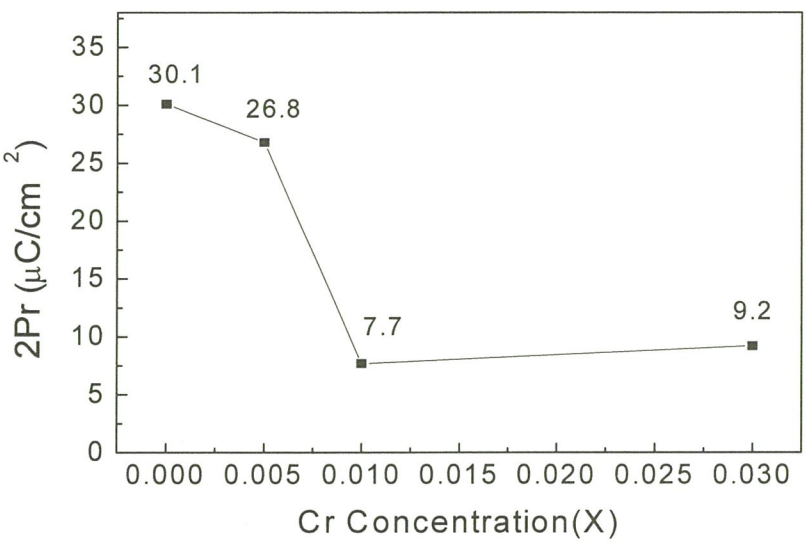

Fig. 1 2Pr vs. Cr concentration 750°C-annealed in BLTCx films.

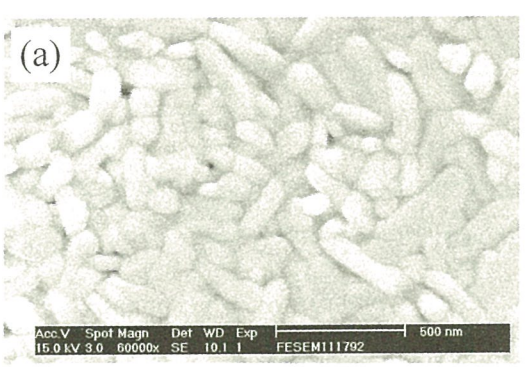

Fig. 2 (a) SEM micrograph of 750℃-annealed BLT films.

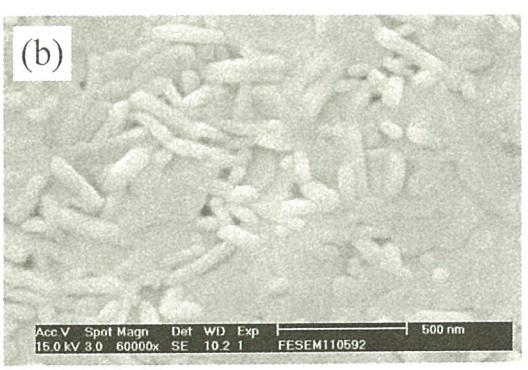

Fig. 2 (b) SEM micrograph of 750℃-annealed $BLTC_{0.03}$ films.

Characterization of Ta_2O_{5-X} thin films Prepared by RF magnetron sputtering

PAI, Yi-Huo (白益豪); LU, Chih-Jung (盧志榮) and SHIEU, Fuh-Sheng (薛富盛)

Department of Materials Engineering, National Chung Hsing University, Taichung 402, Taiwan

Thin films of tantalum pentoxide (Ta_2O_{5-X}) were deposited on polyethylene terephthalate (PET) substrates by RF magnetron sputtering with different oxygen flow ratios ranging from0.6 ~ 1.25. Microstructure of the films was investigated by transmission electron microscopy (TEM) and field-emission scanning electron microscopy (FE-SEM).

Selected area diffraction (SAD) patterns of the Ta_2O_{5-x} films with different O_2/Ar flow ratios of 0.6, 0.8, and 1.25 are shown in Fig. 1(a), (b), and (c), respectively. It can be seen that the oxide films grown at low oxygen flow ratios of 0.6 and 0.8 are amorphous. In contrast, it consists of a mixture of crystalline and amorphous phases at high O_2/Ar flow ratio of 1.25. A 3-dimensional view of the SAD pattern of Fig. 1(c) is shown in Fig. 1(d), in which the sharp 001 reflection of Ta_2O_5, indicating a crystalline structure, is readily seen.

A TEM bright field image of the Ta_2O_{5-x} films prepared at O_2/Ar flow ratio of 1.25 is shown in Fig. 2(a). The film consists of nanocrystalline grains uniformly distributed within an amorphous matrix. Figure 2(b) is the cross-sectional TEM image of the films. For comparison, the intensity profiles of the diffraction rings in the SAD patterns of Fig. 1(a)-(c) are shown in Fig. 3. The 001 reflection of the Ta_2O_5 phase, which has an orthorhombic structure, from the specimen prepared at high O_2/Ar flow ratio of 1.25, corresponding to a *d* spacing of 0.388 nm, is easily discernible from that of the other specimens. Figure 4 shows the FE-SEM image of the Ta_2O_{5-x} films deposited at an O_2/Ar flow ratio of 1.25 for 60 min. The surface morphology of the coatings shows a cellular morphology, in which small grains (about 18 nm) aggregate and microcracks are present among the aggregates.

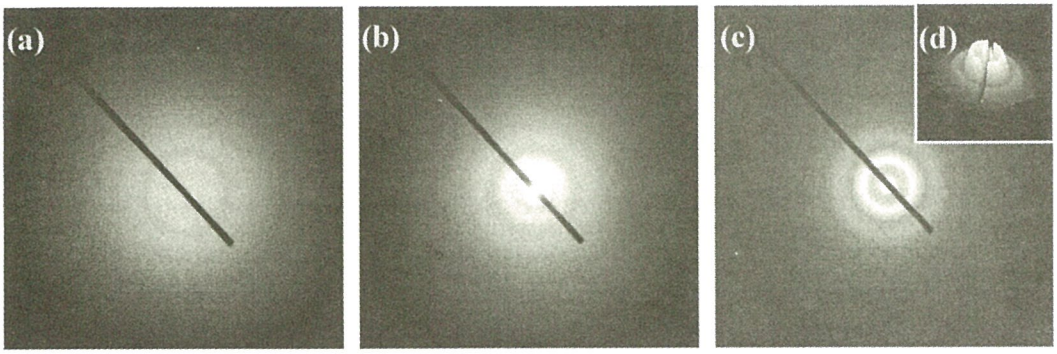

Fig. 1. Selected area diffraction patterns of the oxide films prepared at O_2/Ar flow ratios of (a) 0.6, (b) 0.8, and (c) 1.25, respectively, (d) A 3-dimensional view of the diffraction pattern in Fig. 1(c).

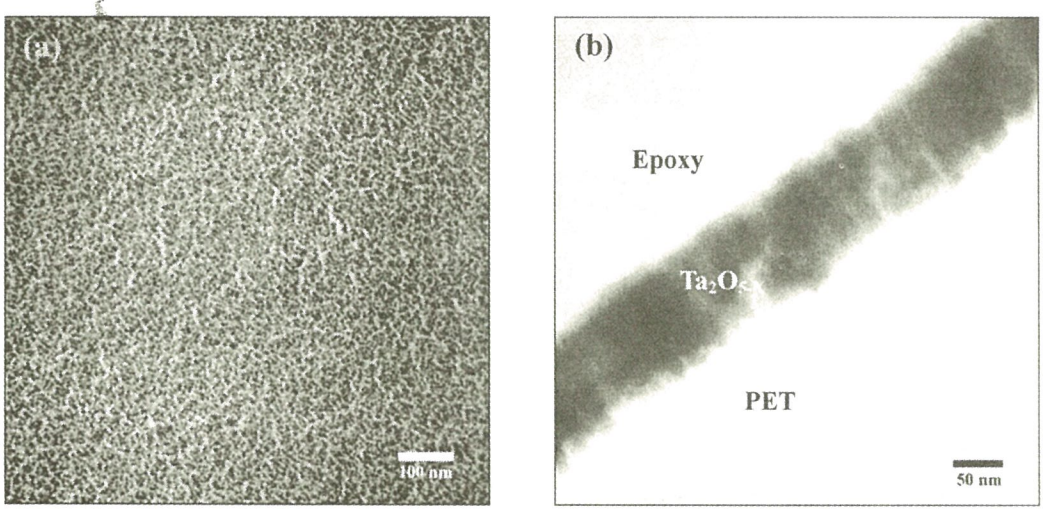

Fig. 2. (a) Plan-view and (b) cross-sectional and TEM bright field images showing the microstructure of the oxide film prepared at O_2/Ar flow ratio 1.25.

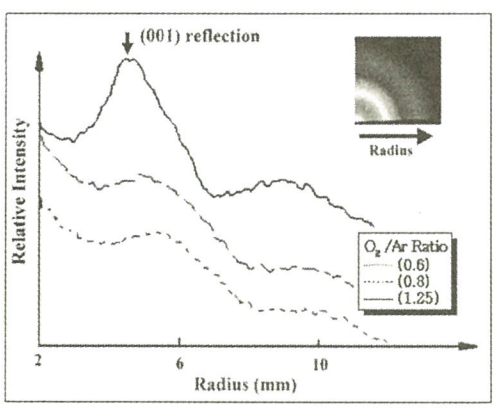

Fig. 3. Radial distributions of the intensity profile in the SAD patterns of Fig. 1(a)-(c).

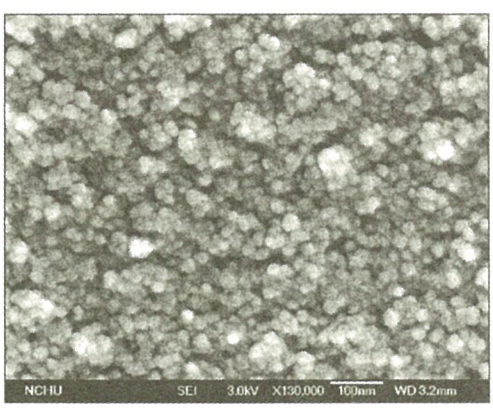

Fig. 4. FE-SEM image showing the surface morphology of the oxide film prepared at O_2/Ar flow ratio 1.25.

tion On A MoTiVCrFeCoNiCuAlZrC
anical Alloying

g[1], and Chen, Swe-Kai[2]

Science and Engineering, National Tsing
300, Taiwan
, National Tsing Hua University,

, contrary to the conventional alloys with
ent(s) as the matrix, have no major
number of component elements, all at
t higher temperatures, e.g., ≥ melting
ave high TΔS term so as to have a high
ergy value, consequently the name
report results of microstructure of the
eCoNiCuAlZrC (Mo-10-C) alloy made
IA).

ders of Mo, Ti, V, Cr, Fe, Co, Ni, Cu, Al
give the desired composition of
and mixed in a glove box under a pure
A process was performed in a high-energy
r different milling time. The morphology
examined by means of scanning
. The structural changes with the milling
xamined by X-ray diffraction (XRD).

NCLUSION

change of particle size distribution of
g time. The particle sizes become more
0 h. In Fig. 5 are the XRD patterns of as
FeCoNiCuAlZrC powders. The as
s a polycrystalline mixture of Mo, Ti, V,
with all intensity peaks present. Milling
e of MA increases, all the peaks
nent metals tend to decrease in
lisappeared. After 20 hours the alloy
phousized. Further experiments of even
sequent sintering/annealing are planned.

MENT

C grant No.NSC-92-2120-E-007-010

T., Gan, J.Y., Chen, S.K., Shun, T.C.,
l Materials for the New Century", in
ess, Chinese Institute of Mining and
g, Taipei, Nov 2002, pp. 13-24.
, and Chen, S.K., Proceedings of the
n microscopy, Jan 2003, M-P-5

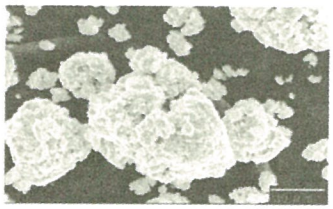

Fig. 1. SEM micrograph of powders milled for 2 h.

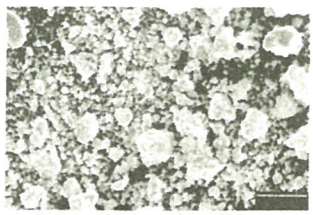

Fig. 2. SEM micrograph of powders milled for 4 h.

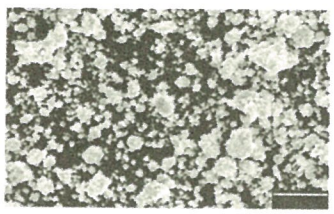

Fig. 3. SEM micrograph of powders milled for 10 h.

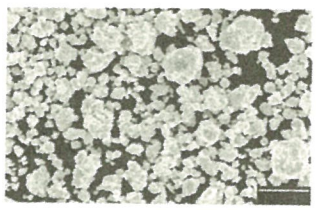

Fig. 4. SEM micrograph of powders milled for 20

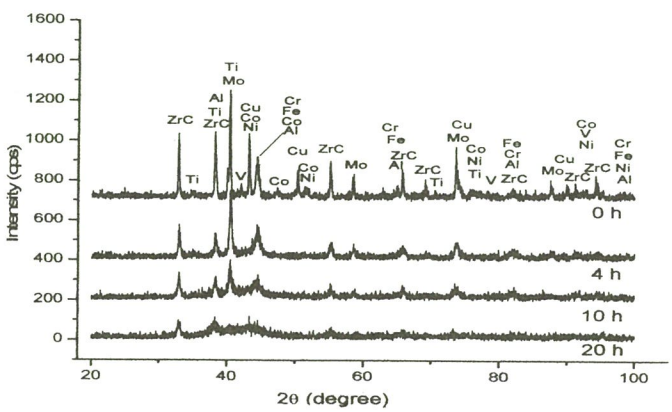

Fig. 5. XRD patterns of MoTiVCrFeCoNiCuAlZrC powders prepared at various time periods of mechanical alloying (MA) showing decreasing intensity with increasing time of MA.

SYNTHESIS and GROWTH of PENTAGONAL COPPER NANORODS

WANG, Jen-Hung[1] (王仁宏); CHEN, Chih-Hung[2] (陳智宏); Chiu, Cheng Jie[2] (邱正傑)and CHEN, Lih-Juann[1] (陳力俊)

[1]Department of Materials Science and Engineering, National Tsing Hua University, Hsinchu, Taiwan
[2]Nanmat Technology Co., LTD., Kaohsiung, Taiwan, Republic of China

One-dimensional metal nanowires and nanorods have attracted increasing interest due to their unique physical properties and diversity for potential electronic and photonic device applications. Among all metal nanowires and nanorods, copper nanowire is the most promising materials for interconnection. However, pure single Cu nanowires and nanorods are hard to prepare owing to the ease of oxidation of Cu in the synthesis process. The better-known methods to fabricate copper nanowires and nanorods are chemical solution-phase syntheses and electrochemical deposition of copper inside polymer channels and anodic aluminum oxide. In the present study, we introduce metalorganic chemical vapor deposition method as a new Cu nanorod growth method which does not involove metal catalyst. The advantages of MOCVD methods are low temperature process, large area growth, and no metal catalyst.

Cu(hexafluroacetylacetonate)$_2$(Cu(hfac)$_2$), which is a kind of deep blue commercial precursor for synthesizing Cu nanorods and was provided by Nanmat Corporation. Ar was the carrier gas to transport Cu(hfac)$_2$ vapor in the CVD chamber and the flow was 10-30 sccm. The reaction temperature of substrates (TaN wafer) was 350-500 ˚C. Field emission scanning electron microscopy (JEOL-6500) clearly revealed the general morphology of the Cu nanorods. TEM (JEOL-2010) was used to characterize the crystal structure of Cu nanorods.

Figures 1(a) and 1(b) show the SEM images of the Cu nanorods grown onto TaN substrate. The length of the Cu nanorod was about 1-2 μm. The density of Cu nanorods is very high and the distribution is rather uniform. Five-fold symmetry of Cu nanorods was found from top view SEM images as shown in Figs. 2(a) and 2(b). Figure 3(a) shows TEM dark field image of the Cu nanorod, and it was found that a high density of parallel stacking faults was formed along the growth direction of the Cu nanorod. The width of the Cu nanorod was about 50 nm from TEM analysis. The structure of the Cu nanorod was single crystalline by diffraction pattern analysis as shown in Fig. 3(b).

Cu nanorods with five-fold symmetry were successfully synthesized by MOCVD method. In previous studies, gold nanorods were assumed to evolve from multiply twinned particles (MTPs) with a decahedral shape. However, these studies did not provide any evidence to confirm that cross sections of these nanorods indeed exhibited a pentagonal shape. In the present study, Cu nanorods with pentagonal shape was observed due to the Cu nanorods mostly grown vertically on the substrate as shown in SEM images.

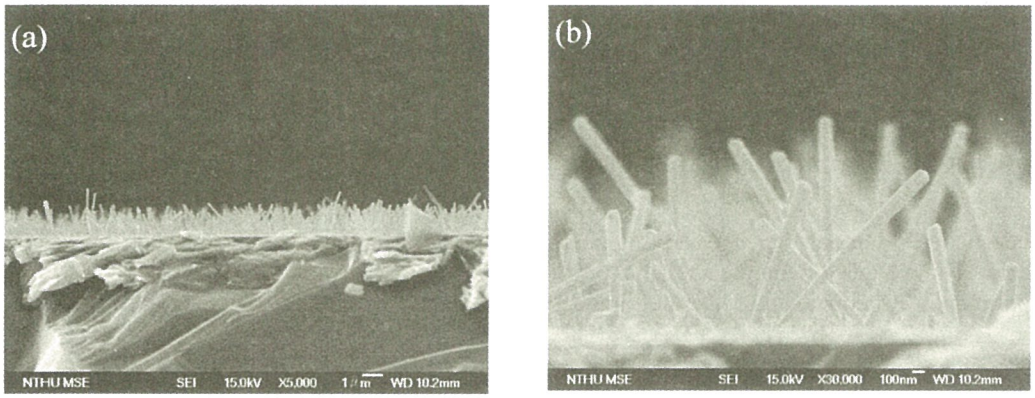

Fig.1(a) and (b) SEM images of Cu nanorods grown on TaN substrate.

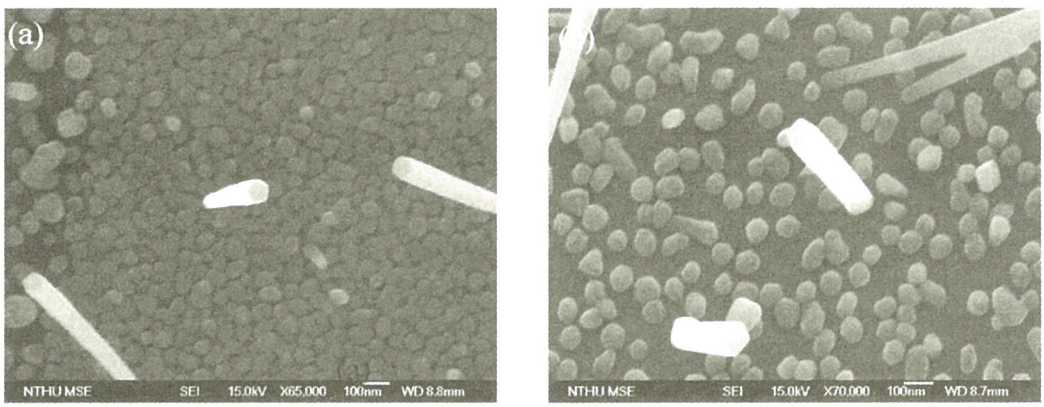

Fig. 2(a) and (b) SEM images of Cu nanorods (top view), and the pentagonal shape of the Cu nanorods was found.

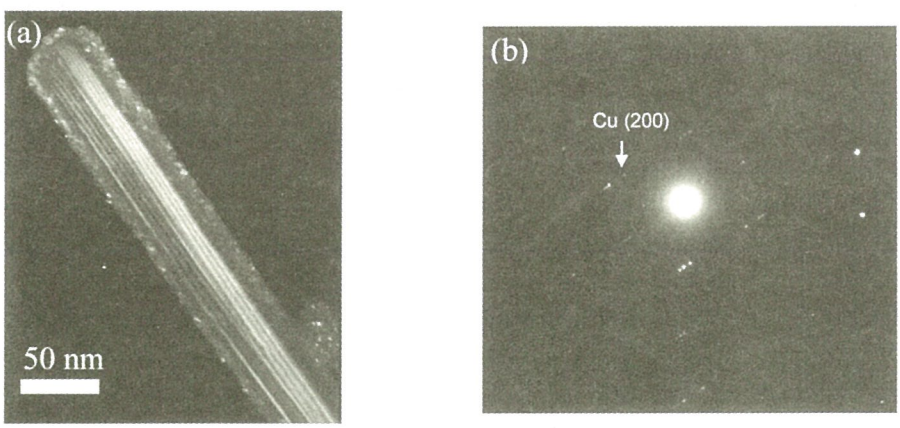

Fig. 3(a) TEM dark field image of the Cu nanorod, (b) diffraction pattern of the Cu nanorod.

SELF-ASSEMBLED HEXAGONAL Au AND Ag PARTICLE NETWORKS ON SILICON FROM Au AND Ag NANOPARTICLE SOLUTIONS

LU, Ming-Yan[1](呂明諺); SU, Pai-Ying[1](蘇百櫻); LIANG, Ju-Ming [2](梁鉅銘); HU, Jung-Chih[1](胡榮治); CHENG, Shao-Liang[3](鄭紹良) and CHEN, Lih-Juann[1](陳力俊)

[1]Department of Materials Science and Engineering, National Tsing Hua University, Hsinchu, Taiwan
[2]National Nano Device Laboratory, Hsinchu, Taiwan
[3]Department of Chemical and Material Engineering, National Central University, Taoyuan, Taiwan

Metal nanoparticles have been widely investigated due to their unique applications in diversified fields. Many two-dimensional (2-D) arrays of metal nanoparticles by self-assembly were successfully formed. In this study, we report the self-assembly of hexagonal network of Au and Ag particles from Au and Ag nanoparticle solutions as well as its underlying mechanism and technical implications.

The colloidal Au and Ag nanoparticles were synthesized by a two-phase method. Dispersion solutions of Au and Ag nanoparticles were prepared with 5.36 g and 5 g of nanoparticles/liter (g/l) of toluene, respectively. A 10-μl droplet of dispersive solution of nanoparticles was drop-cast with a micro-pipet on a 5 mm x 5 mm n-type (001)Si wafer. The solvent was evaporated while placing the substrate in an air-extracting apparatus with appropriate airflow, humidity and temperature. Heat treatments were carried out in a three-zone diffusion furnace in N_2 ambient.

Figure 1 shows the TEM image of the Au@TOAB-DT nanoparticles. The average size of the Au nanodots was 4.9 nm. Regular hexagonal network was found to form in drop-cast samples by self-organization with a wide range of conditions. An example is shown in Fig. 2. After annealing at 400 ℃ for 60 min, the integrity of honeycomb networks was still maintained. However, the ribbons of honeycomb networks were found to thin down as well as to become disconnected. An example is shown in Fig. 3. After annealing at 800 ℃ for 1 h, the ribbons of honeycomb start to aggregate to the intersections which is attributed to the coarsening of Au structure driven by minimizing the total surface energy. For annealing at 1000 ℃ for 60 min, Au atoms from hexagonal skeleton aggregated further at the intersections. An example is shown in Fig. 4.

The eutectic point for the Au-Si system is known to be as low as 363 ℃. XTEM images revealed the presence of a thin layer of oxide at the Au/Si interface and relatively small Au particles as shown in Fig. 5. The oxide interlayer stabilized the Au particles so that the mixing of Au with Si and rapid diffusion into the underlying Si are prevented. Figure 6 shows the SEM images of Ag networks after annealing at different temperatures. With increasing annealing temperature, the ribbons of honeycomb aggregate to the intersections gradually. The phenomenon is rather similar to the formation of Au networks.

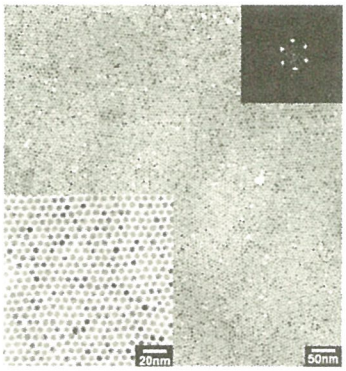

Fig.1 TEM image of Au@TOAB -DT nanoparticle superlattice showing a long-range ordered and uniform in size 2-D array structure. Inset is a magnified view of the selected region of the superlattice. Another inset is the FFT pattern of the selected area.

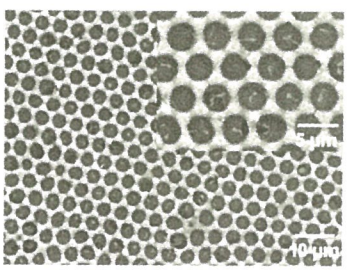

Fig.2 SEM image of a 5.36 g/l Au nanoparticles deposited sample. The inset shows magnified view of selected area.

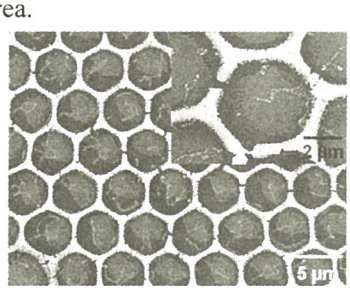

Fig. 3 SEM image of 5.36 g/l Au nanoparticles deposited sample annealed at 400 ℃ for 60 min. The inset shows magnified view of one of the hexagons.

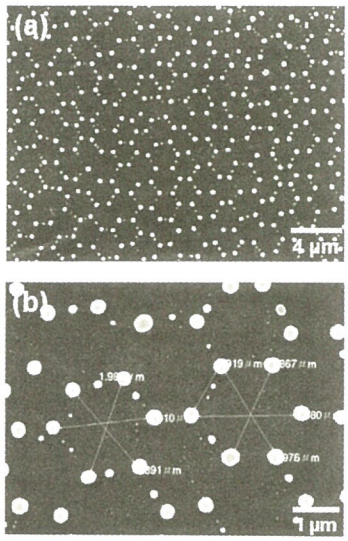

Fig. 4 (a) SEM image of Au nanoparticles deposited sample annealed at 1000 ℃ for 60 min, (b) magnified view of selected area in (a).

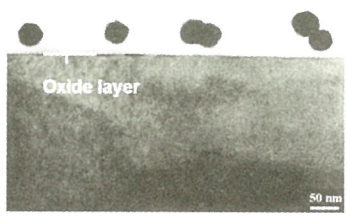

Fig. 5 XTEM image showing the presence of a thin layer of oxide at the Au/Si interface.

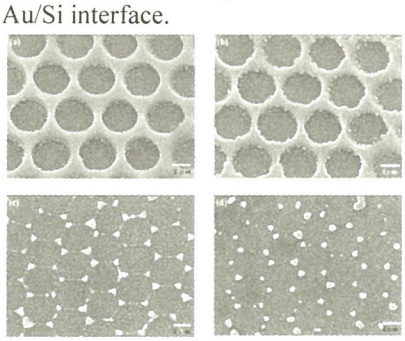

Fig. 6 SEM images of Ag networks(a) as-deposited and after annealing at (b) 400 ℃, (c) 600 ℃ and (d) 700 ℃ for 60 min.

SYNTHESIS OF NOVEL BLUE LIGHT-EMITTING $Si_{1-X}Ge_X$ OXIDE NANOWIRE NETWORKS ON $Si_{0.8}$ $Ge_{0.2}$.

WU, Te-Hui(伍得惠), HE, Jr-Hau(何志浩), CHEN, Lih-Juann (陳力俊)

Department of Materials Science and Engineering, National Tsing Hua University, Hsinchu, Taiwan.

Synthesis of novel blue-light $Si_{1-X}Ge_X$ oxide nanowires catalyzed by the self-assembled hexagonal Au particle networks has been achieved by thermal annealing at 1080 ℃ for 5 min. The TEM and EDX studies indicated that the nanowires possess an amorphous structure and are composed of Si, Ge, and oxygen. The photoluminescence spectra showed that the $Si_{1-x}Ge_x$ oxide structure emits blue light with a peak at around 415 nm, which is in the blue light wavelength region.

Au honeycomb structure on a 5 mm x 5 mm $Si_{0.8}$ $Ge_{0.2}$ wafer was drop-cast from the Au nanoparticle solution, which was synthesized by a two-phase method. After three steps thermal annealing in a quartz tube at 400 ℃ for 30 min, 800 ℃ for 60 min, and 1080 ℃ for 5 min in N_2 ambient, the hexagonal $Si_{1-X}Ge_X$ oxide nanowire networks was obtained. The photoluminescence properties of synthesized nanowires were measured using a He-Cd laser in the spectral range of 350-800 nm with a wavelength of 325 nm as the excitation source. Morphology and structure of grown nanowires have been examined by TEM and SEM analysis.

The honeycomb structure of Au nanoparticles on $Si_{0.8}Ge_{0.2}$ wafer was first obtained. After heat treatments, the hexagonal Au particle network was obtained, as shown in Fig. 1. As the annealing temperature increased to 1080 ℃ and maintained for 5 min, the nanowires catalyzed by the hexagonal Au particles were formed, as shown in Fig. 2. The top-view image and cross-sectional image of the nanowires are shown in Fig. 3. The chemical composition of the nanowires is about Si:Ge:O＝20:2:11 determined from EDS analysis. Figure 4 shows the TEM image of the $Si_{1-X}Ge_X$ oxide nanowires, which are shown to possess an amorphous structure. It is widely recogined that the intensive light emission from Si oxide nanowires can be attributed to the oxygen deficiency ($O_3 \equiv Si - Si \equiv O_3$), and the structural defects were radiative recombination centers in the amorphous Si oxide nanowires. The PL spectra of the synthesized Si_xGe_{1-x} oxide nanowires was analysed. An example is shown in Fig. 5. The nanowires have a strong blue emission peak centered at 415 nm, which is in the blue-light wavelength region. As a result, the light-emitting property of such synthesized $Si_{1-x}Ge_x$ oxide nanowires was distinct from the Si oxide nanowires which have the PL wavelength around 450~ 550 nm.

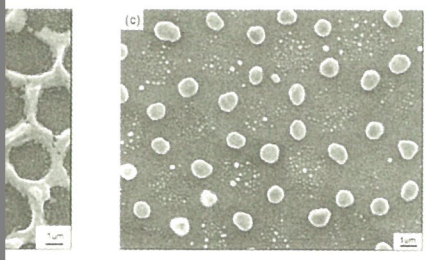

anoparticle solution on $Si_{0.8}Ge_{0.2}$
) min. (c) The hexagonal Au particle
800 ^{o} C for 60 min.

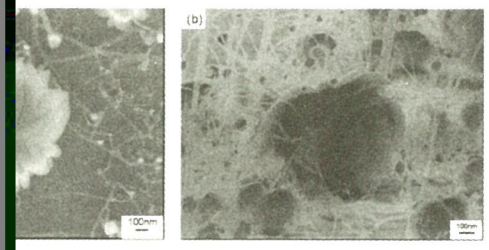

Top-view image and (b) the
ss-sectional image of oxide
nowires catalyzed by the hexagonal
particles.

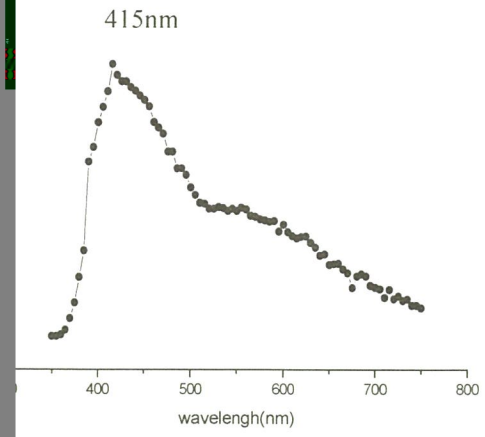

Room temperature PL spectrum of
Si_xGe_{1-x} oxide nanowires.

The study of Nickel implanted Gallium Nitride

Hsu, Chen-Feng(徐振峰), Huang,Rong-Tan(黃榮潭), Chen, Fu-Rong(陳福榮) and Kai, Ji-Jung (開執中)

Department of Engineering and System Science, National Tsing Hua University, Hsinchu, Taiwan 300, R.O.C.

Diluted magnetic semiconductors (DMSs) have long been of great interest as they combine the two large branches in condensed matter physics; semiconductor and magnetism. By using nonequilibrium growth conditions of low-temperature molecular beam epitaxy (LT-MBE), a Ⅲ-Ⅴ based DMS, ferromagnetic (Ga,Mn)As was successful prepared. Magnetotransport measurements revealed that the magnetic transition temperature can be as high as 110K [1]. Studies on the Ⅲ-Ⅴbased DMSs have become one of the fascinating subjects in the research fields of semiconductors and magnetic materials.

Currently, in addition, little is known about the properties of GaN doped with impurities that might induce ferromagnetic behavior. Some initial reports have appeared on microcrystalline $Ga_{1-x}Mn_xN$ with Mn contents up to x = 0.005 which exhibited ferromagnetic behavior [2,3].

In our study, the undoped GaN with a thickness of 2.5 μm was grown by metal-organic chemical deposition on a (0001) sapphire substrate, followed by a grown of 10-nm-thick Ni. Ni^- ions were implanted into the Ni(10nm)/undoped GaN films with an energy of 72keV and does of 5×10^{16} cm^{-2}, following we remove the Ni(10nm) film by wet etching.

Based on the transport-of-ions-in-matter(TRIM) simulation, we discovery that the buffer layer of 10-nm-thick Ni film not only reduce most of damage induced by ion implantation in the GaN but also lose less of dose as shown in Fig.1(a)(b). Fig.2(a) shows TEM image of the cross sectional view of the Ni-implanted GaN. The HRTEM image of Ni-implanted GaN shown in Fig.2(b) indicates that there is less distortion of the lattice in Ni-implanted GaN film and no amorphous layer formed. Fig.2(c) shows the SADP from the implanted region. We only observed the diffraction of the GaN hexagonal crystal structure and there are no obvious extra spots from secondary phase formation.

Reference

[1] H.Ohno, Science 281, 951 (1998)
[2] W. Gebicki, J. Strzeszewski, Appl. Phys. Lett. 76, 3870 (2000)
[3] M. Zajac, R. Doradzinski, Appl. Phys. Lett. 78, 1276 (2001)

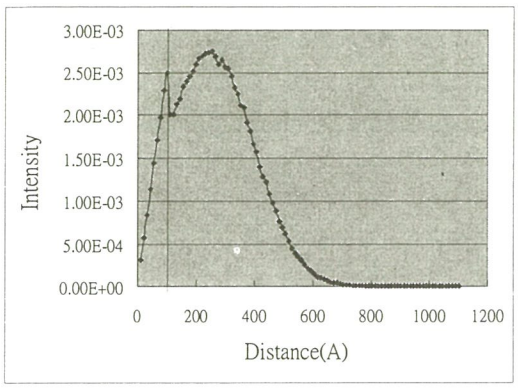

Fig. 1(a)

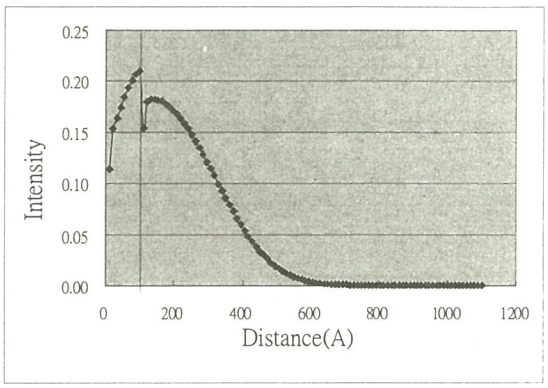

Fig. 1(b)

Fig. 1 TRIM simulation of ion range distribution (a) and vacancy distribution (b) for Ni doped Ni(10nm)/GaN films

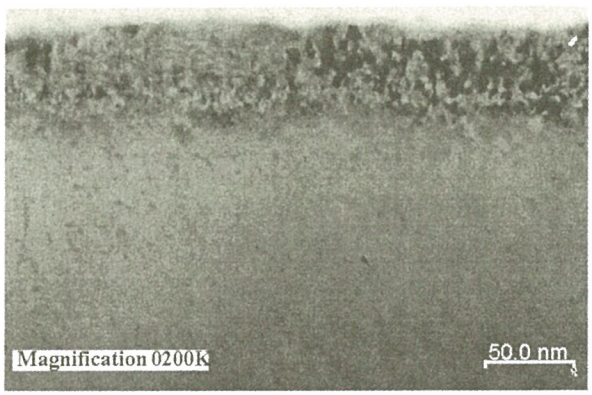

(a)

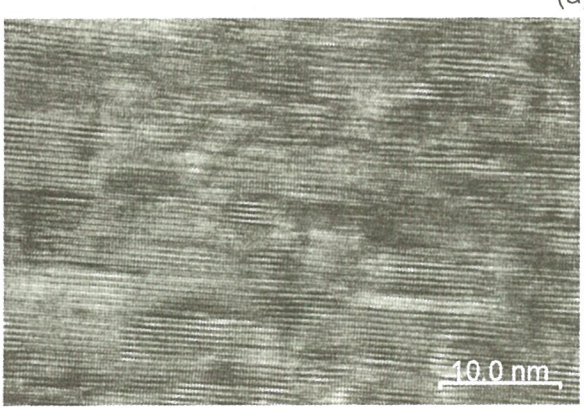

(b)

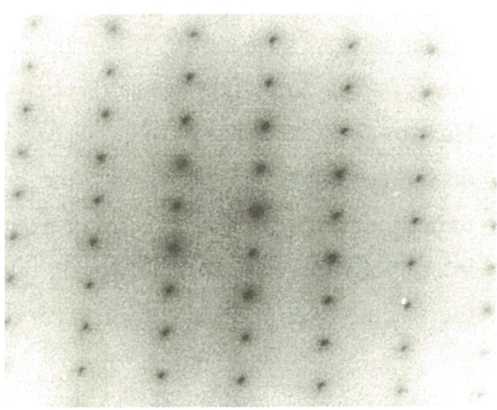

(c)

Fig. 2 (a) TEM image of Cross sectional view of Ni-implanted GaN
(b) HRTEM image of Ni-implanted GaN, showing no amorphous layer formed.
(c) SADP from the implanted region, showing no second phase formed.

OXIDATION BEHAVIOR OF TiN WITH A Ti INTERLAYER ON STAINLESS STEEL

SHIAO, Ming-Hua (蕭銘華)[1] ; WANG, Ching-Chiun (王慶鈞)[2] ; SU, Chien-Ying (蘇健穎)[1] and SHIEU, Fuh-Sheng (薛富盛)[2]

[1]Precision Instrument Development Center, National Science Council, Hsinchu
[2]Department of Materials Engineering, National Chung Hsing University, Taichung

TiN thin films with a Ti interlayer were deposited by hollow cathode discharge ion plating on AISI 304 stainless steel. Characrerization of the TiN coatings oxidized in air at temperatures of 600 ℃ in air for 30 min was carried out by transmission electron microscopy (TEM).

A cross-sectional TEM image of the as-deposited titanium nitride coating with a Ti interlayer on steel substrate is shown in Fig. 1. The TiN coating with a Ti interlayer is mainly composed of columnar grains, and a very good epitaxial relation between these two layers. A close look at the Ti-steel interfacial region, there exists a thin layer which thickness is approximately 15 nm, it is believed that composed of Fe_2Ti intermetallic phase based on the SAD pattern[1-2]. It is interesting that there is a pit on the surface of steel substrate due to electropolishing and the later deposited Ti layer and TiN coating grew along the morphology of the steel surface.

Figure 2 shows the cross-sectional electron micrograph of a TiN-coated specimen oxidized at 600℃ in air for 30 min. The porous TiO_2 oxide layer, about 275 nm in thickness, is present on the coating surface, but it retains the columnar structure as the TiN coating. The center of the coating still retains the columnar structure as well as the as-deposited TiN coating. It can be distinguished from the image contrast in Fig. 2 around the Ti-steel interface, there are two distinct regions appearing in the Ti interlayer. Heat-treatment has made the base part of the columnar Ti grow into equiaxed grain structure due to grain growth. It is noted that the region of Fe_2Ti intermetallic phase becomes thicker undergo grain growth after heat-treatment. Interdiffusion was occurred between the Ti interlayer and steel substrate during the heat treatment, resulted in a different contrast within the Ti interlayer and a diffusion layer of Ti about 100 nm in depth under the steel surface.

References

(1)Wen , L. S., Jiang , X. and Si , C. Y. ; J. Vac. Sci. Technol., A 1986 (4) 2682.
(2)Shieu , F. S., Cheng , L. H., Shiao , M. H. and Lin , S. H. ; Thin Solid Films 1997 (311) 308

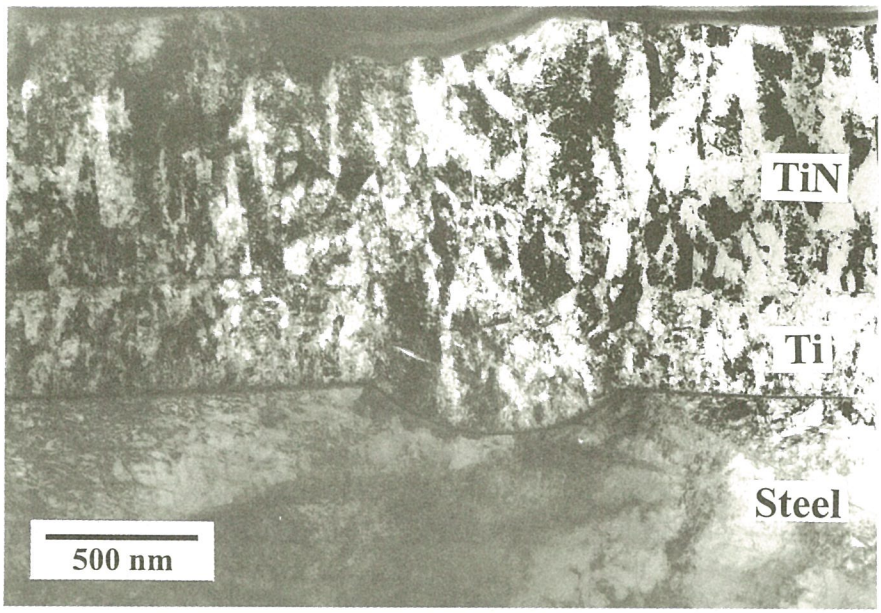

Figure 1. Cross-section TEM micrograph of the as-deposited TiN coating.

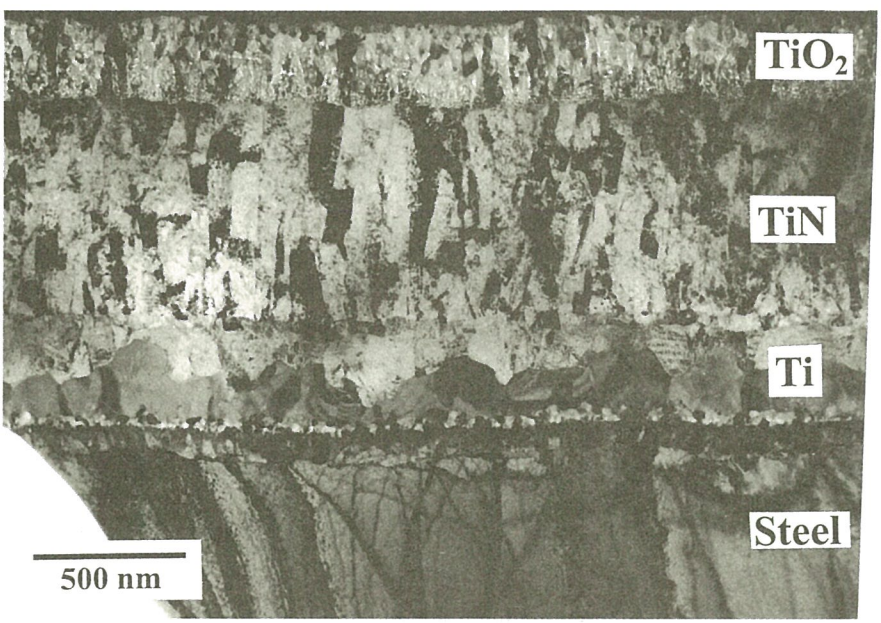

Figure 2.Cross-sectional TEM micrograph of the 600℃ oxidized specimen.

The Investigation of Interface and Electrical Properties in GaAs Wafer Bonding

Ji-Hao Cheng[1] (鄭季豪), Hao Ouyang[1] (歐陽浩) YewChung Sermon Wu[2] (吳耀銓), and Chen-Lun Lu[2] (盧正倫)

[1]Department of Materials Engineering, National Chung-Hsing University, Taichong, Taiwan 402, R.O.C.
[2] Department of Materials Science and Engineering, National Chiao-Tung University, Hsinchu 300, Taiwan

ABSTRACT

Using energy-filter transmission electron microscopy (EFTEM), we investigated the microstructure of the interface fabricated after twist-bonding(90°and 180°) two N and P-type GaAs wafers respectively at a series of annealing temperatures to evaluate the electrical performance of the compliant substrate[1]. We observed the interface defect (fig.1) by high-resolution EFTEM and employed convergent electron beam with size of 5~7nm to study the microstructures and oxygen distribution around the interface(fig.2). The electronic structure of the bonding interface was studied by the nano-beam electron energy loss spectrum (EELS). And the oxygen EELS mapping was obtained by two methods: the jump-ratio mode and three windows mode (fig.3)[2]. The high-angle annular-dark field (HAADF) image, which was also called "z-contrast image", was acquired in the mode of scanning transmission electron microscopy (STEM) in order to understand the distribution of oxygen near the interface. Energy dispersive x-ray spectroscopy (EDS) line-scan (fig.4) will also used to confirm the oxygen distribution. At last, we analyze the overall result which was obtained by TEM along with the electrical properties (I-V curve). We find that in addition to the intrinsic difference in the electrical performance of both the N and P-type wafers, the oxygen diffusion and oxides in the interface will affect the overall electrical performance.

REFERENCE

1.Y.H. Lo, Appl. Phys. Lett. 59, 2311, 1999

2. Transmission Electron Microscopy and Diffractometry of Materials, B. Fultz, J.M. Howe, 2002.

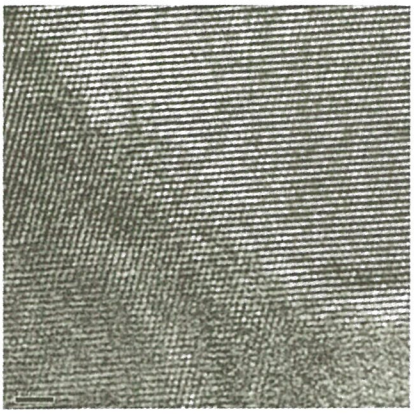

Fig. 1 zero-loss image

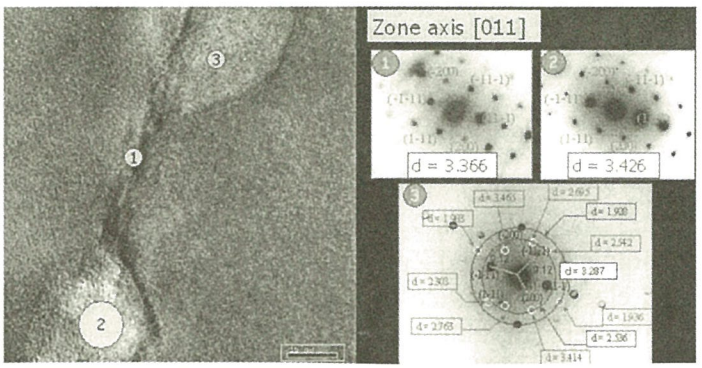

Fig. 2 convergent-beam diffraction

(a) EDS linecan　　(b) HAADF (z-contrast) image

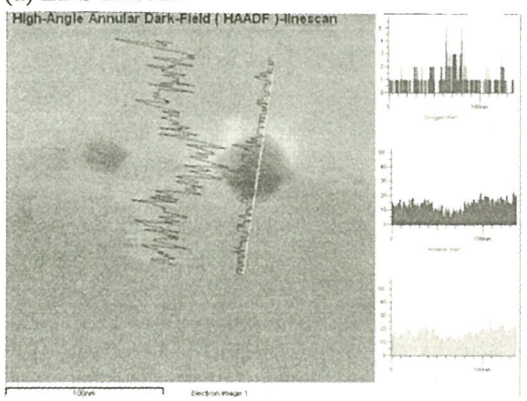

Fig. 3　EDS linescan and HAADF (z-contrast) image

(a) Jump-ratio mode　　(b) Three window mode

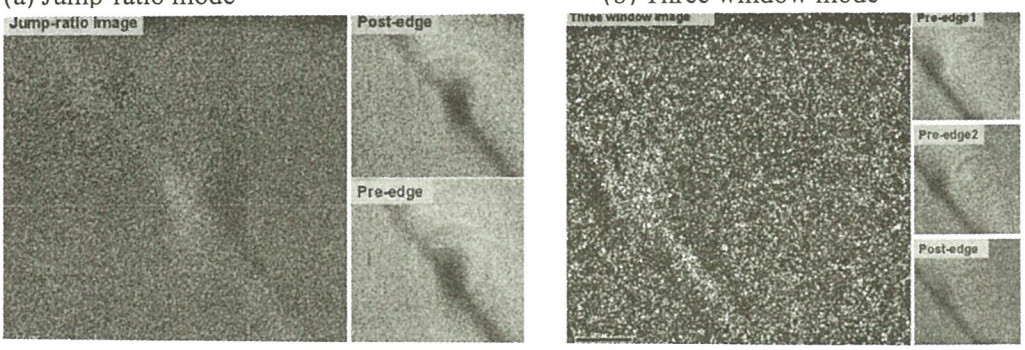

Fig. 4　two EELS mapping (a) jump-ratio mode　(b) three window mode

ZnO nanodrill growth

CHIU, Hsu-Feng (邱旭鋒); HE, Jr-Hau (何志浩); YANG, Tzu-Hsien (楊子賢); WANG, Jen-Hung (王仁宏) and CHEN, Lih-Juann (陳力俊)

Department of Materials Science and Engineering, National Tsing Hua University, Hsinchu, Taiwan.

Shape, size, and orientation are the most important consideration for nano-materials. 1-D ZnO has many structures such as nanowires, nanobelts, and nanotubes. Aligned ZnO nanostructures are finding potential applications for optical and electronic devices like laser, light emitting diodes, sensors, nanoresonators and cantilevers. In addition, field-emission devices have been reported due to their great physical properties, including its wide band gap (3.37 eV) and large binding energy. There are many different methods to grow ZnO. In this paper, we report the growth of nanodrill structure with 10-150 nm width and 1-2 μm length.

The fabrication process was carried out in an alumina tube. The source materials were mixed pure ZnO and graphite powder (molar ratio 1:1) and placed in an alumina boat at the high temperature zone. The temperature was between 500 °C and 1200 °C in the two zone alumina furnace and the holding time was 90 min. The pressure was fixed in 200 Pa with the flow consisting of Ar 25 sccm and O_2 5 sccm. The reduced Zn vapor formed from the source material in the high temperature zone flowed to the sapphire substrate at the low temperature zone. The temperature, pressure, flow, and the source quantity also influenced the shape. Hexagonal ZnO epi-layer has grown along the special directions.

Figures 1 and 2 are the cross-section SEM image. Figure 1 shows the growth of nanowires along three directions. Figure 2 shows the drill-like morphology of ZnO. The outer drill shape could be induced from the defects in the inner crystal. The defects bend the adjacent lattice. From Fig. 3 the TEM image shows the length to be about 10-150 nm and width about 1-2 μm. Figure 4 is the high-resolution TEM image showing the single crystal phase in the nanodrill and the presence of defects. Figure 5 shows the 2-D lattice image. The lattice spacing between adjacent lattice planes is approximately 0.26 nm corresponding to the distance between two (002) crystal planes, confirming [001] as the preferred growth direction for ZnO nanowire in the nanodrill.

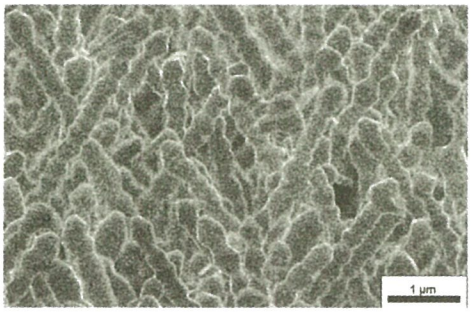

Fig. 1. Cross-section SEM image showing ZnO rods along three directions.

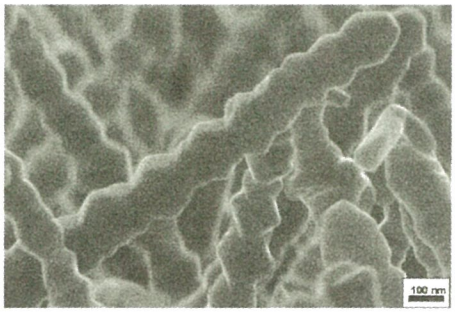

Fig. 2. Cross-section SEM image showing the nanodrill structure.

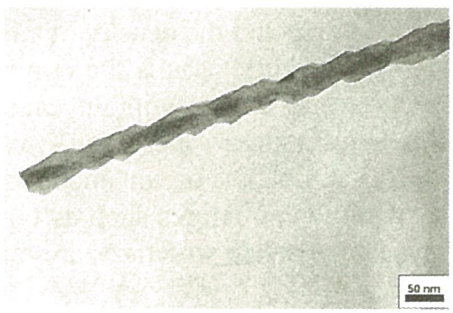

Fig. 3. TEM image showing the nanodrill is about 100 nm wide and 2 μm long.

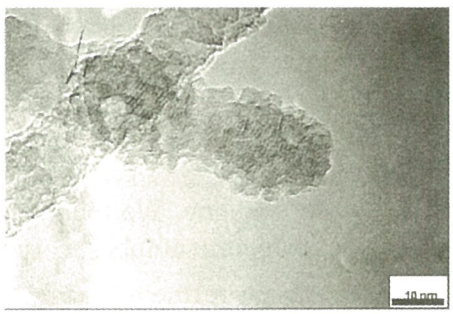

Fig. 4. HRTEM image showing the crystallinity of ZnO

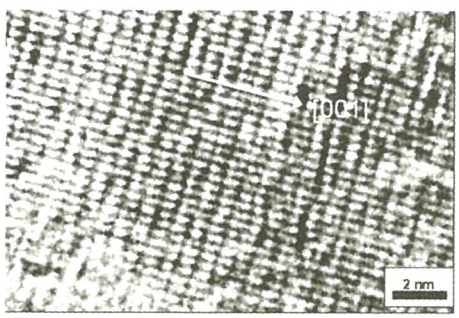

Fig. 5. The HRTEM image showing the growth direction is along [0011]

GROWTH OF CONED-SHAPED CARBON NANOTUBES BY ARC DISCHARGE IN ANODE

LIN, Chih-Jen(林智仁); KUNG, Sheng-Chin(龔聖欽); HSU, Chih-Ming(許智明); LI, Bean-Jon(李秉璋); LAI, Hong-Jen(賴宏仁)

Materials Research Laboratories, Industrial Technology Research Institute, Hsinchu.

Abstract:

Since multi-walled carbon nanotubes (CNT) were developed in 1991[1], CNTs have been receiving attention for their unique characteristics and their potential for use in various applications. Various synthesis methods of CNTs are developed. One of the main methods for producing CNTs is the DC (direct current) arc discharge between two graphite electrodes in a buffer atmosphere. Typically the buffer atmosphere is helium, and formation of a nanotube-containing deposit on the cathode. Several factors, such as the species of the buffer atmosphere and the density of carbon vapor, influence the growth of CNTs. The pressure of the buffer gas is the dominant factor in the chamber. This study presents the CNTs production without catalytic metals by DC arc discharge performed in ambient helium at low-pressure (~ $5x10^{-2}$ torr). After arc discharge, observation of several forms of CNTs is on the anode rather than in that on the cathode. We found that different carbon structures such as typical nanotubes, cone-shaped nanotubes, carbon capsules and awl-like structures are on the anode.

Fig.1 showed the FE-SEM image of CNTs with diameters of approximately 15~30nm and 1~5 μm long. It is almost free of defects as shown in Fig. 2 from the high-resolution electron microscopy (HREM) image. Fig.3 and 4 presented the HREM and field emission scanning electron microscopy (FESEM) images of by-product in the deposit such as awl-like structure, respectively. Fourier transformation method calculated the cone angle of these structures is approximately 20°. The calculation agrees the 19.2° cone angle for graphitic cones with five pentagons [2]. Fig.5 showed the possible mechanism of the formation the structures. If the stream of carbon atoms that are moving toward a growing structure ceases or fluctuates, the unclosed matrix can close because the number of unsaturated carbon bonds must be reduced as shown in Figs. 5a and 5b. Circular graphitic particles, capsules, and polyhedrons are formed under this condition. In contrast, the perfect graphite structures without defects are prone to stacking regularly into helical structures with a closed faceted end, as depicted in Figs. 5c and 5d. The growth of carbon materials, such as nanotubes or conical-shaped carbon, seems to be dominated by dangling bonds, which are the violent fluctuations of the stream of carbon atoms.

Reference:

1. S. Iijima, Nature, 1991 (56) 354.
2. P. J. F. Harris, 75 "Carbon Nanotubes and Related Structures" 1999.

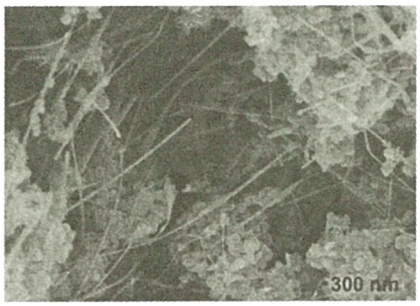

Fig. 1 SEM image of the anode deposit

Fig.2 TEM image of the nanotube with defect free structure by the nanotube and the capsule

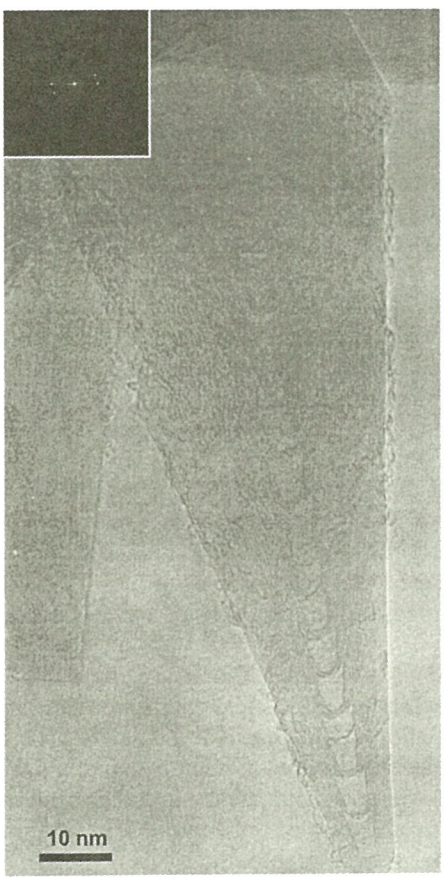

Fig. 3 HRTEM image of the awl-like structure nanotubes.

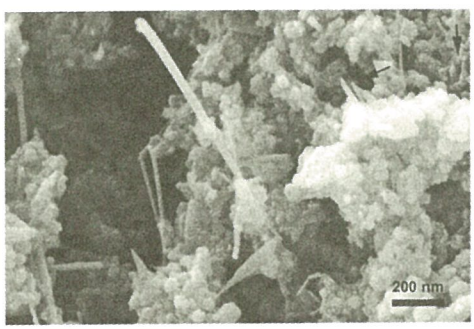

Fig. 4 FESEM image of the awl-like structure nanotubes.

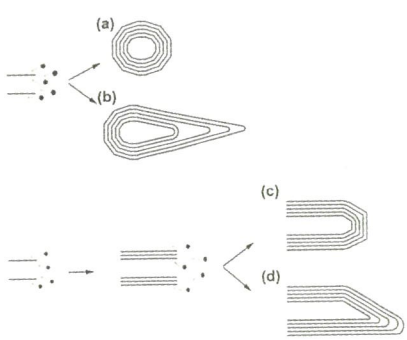

Fig. 5 Mechanism of growth of deposit on the anode

NEW GENERATION TECHNOLOGY OF SPECIMEN PREPARATION FOR TRANSMISSION ELECTRON MICROSCOPE：APPLICATION IN HIGH DENSITY OPTICAL STORAGE MEDIA

Lo, Shen-Chuan(羅聖全)；Chiang, Cheng-Cheng (江正誠)；Lin, Chih-Jen(林智仁)；Chen, Shu-Chen(陳淑貞)；Lin, Li-Jiaun(林麗娟)；Horng, Jain-Long(洪健龍)

Microstructure and Characterization Lab., Materials Research Laboratories, Industrial Technology Research Institute, Hsinchu.

Abstract：

Blu-ray disc (BD) has been rapidly developed as 25 GB high-density storage media. Recently, a super-resolution near-field structure (super-RENS) disk is one of the most promising technologies for a subterabyte optical storage of approximately 200 GB storage capacities. The discs usually consist of several layers in a sandwich type structure with layer thickness around or below half hundred nanometers. A typical high-density storage disc consists of a protective layer followed by a reflective layer (e.g. Al or Ag alloy), dielectric (e.g. ZnS-SiO_2)/ phase change recording (e.g. Ge-Sb-Te or Ag-In-Sb-Te)/dielectric sandwich structure and a polycarbonate substrate. Introducing more layers to recording layer (recording/ ZnS-SiO_2/ PtO_X/ ZnS-SiO_2/ recording) with chance its recording mechanism can improve the disc properties such as carrier-to-noise ratio (CNR)[1].

Good TEM specimens with thinner (~40nm) and large electron transparent area are more important for advanced TEM characterization. Using the advanced TEM techniques such as energy-filtering TEM (EFTEM) and high angle-annular dark field (HA-ADF) can confirm the recording mechanism in high-density optical storage media. In the past years, several cross-sectional TEM specimen preparation of optical disc such as tripod (T-tools) method, focus ion beam (FIB) method and ultramicrotomy are often used for TEM microstructure characterization [2,3]. However, both FIB and ultramicrotomy methods cannot provide large electron transparent area and have artifact problem. Now the advanced TEM specimen preparation technology with T-tools, low angle (~2°) and low energy (0.5~1kV) ion milling method has been successfully to prepare the high-density optical storage media TEM cross-section specimens.

Fig.1 showed the cross-sectional TEM image of typical optical storage media preparation by advanced TEM specimen preparation. Investigation showed that this preparation method is successfully and allows for detailed studies on layer morphology and layer composition identified. Fig.2 showed the high-resolution TEM image of A area which across the recording layer to corroborate the interface between the dielectric layer and recording layer. The image revealed there is an unknown layer near upper recording layer. Further, advanced analytical methods using HA-ADF technique (Fig.3) can be applied to gain detailed, spatially resolved knowledge on the chemical composition of disc.

Reference:

[1]. Kim, J. et al.；Appl. Phys. Let., 2003 (83)9 1701.

[2]. Giannuzzi, L.A. et al.；Micron, 1999 (30) 197.

[3]. Zhang, H. et al.；Micron, 2002 (33) 515.

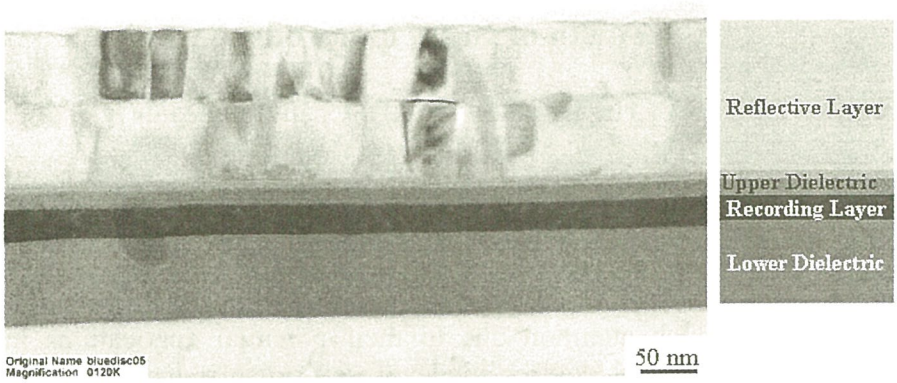

Fig.1 Clear cross-sectional TEM image of high-density storage optical media.

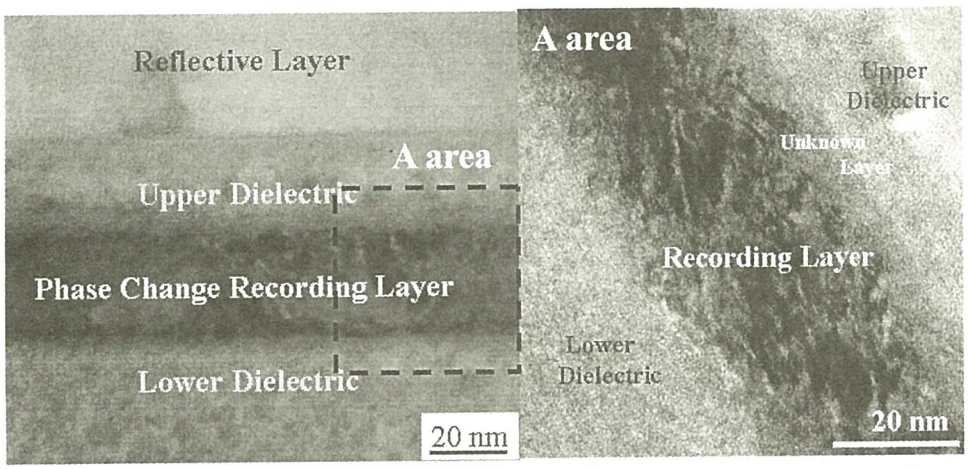

Fig.2 The HREM image of A area which revealed a very clear and sharp interface morphology.

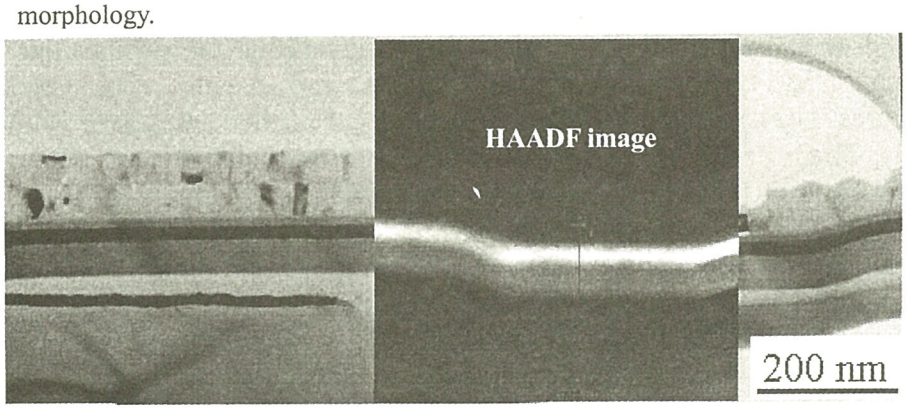

Fig.3 HA-ADF image of the interface across the recording layer. The bright feature correspond to the recording layer of Se alloy.

Growth of In_2O_3 nanorods

Hsin, Jheng-Lun (辛正倫)；He, Ji-Hau(何志浩)；Chen, Lih-Juann(陳力俊)

Department of materials science and Engineering, National Tsing Hua University, Hsinchu

Growth of self-organized semiconducting nano-structures that possess quantum effects has attracted much attention due to their potential applications in many different devices. The optical devices made of self-organized quantum materials influence their properties by their size effects. The characteristics of the devices have therefore been enhanced. In the present study, direct band gap, semiconducting In_2O_3 nanorods have been grown in the vacuum furnace. Several types of In_2O_3 with novel shape have been formed. Previous methods to fabricate In_2O_3 nanowires were focused on vapor-liquid-solid (VLS) mechanism and anodic aluminum membrane (AAM). VLS method can form nanowires that is straight and more than several microns long with a catalyst at its end and nanowire array could be formed by AAM. In our experiment, we employed the silver film as a catalyst and successfully grew the pyramid-like In_2O_3 nanorods.

A vacuum furnace with vacuum better than 1 torr was used. Single crystal, 1-30Ω-cm, (001) oriented silicon wafers were used as substrates. Prior to the loading into the furnace, the wafer was cleaned by standard RCA process and 1 nm silver film was evaporated on the substrate by an E-beam system. The sample was placed at the downstream and the In_2O_3 powder at the upstream. The samples were annealed at 700 ℃-900 ℃ at 4.5 torr. A JEOL-200CX scanning transmission electron microscope (STEM) and a JEOL-6500 scanning electron microscope (SEM) were used to study the microstructures and to determine the compositions of the samples.

Figures 1 (a), (b) and (c) show SEM images of the samples revealing In_2O_3 nanorods. Their sizes were around 30-50 nm and the lengths were about 200-400 nm. The shape of the wires was pyramid-like and became sharper at the tip. The In_2O_3 nanorods were well aligned as shown in Fig 1 (c). Diffraction pattern analysis indicated that the nanorods are In_2O_3, with (211), (222), (400) and (440) diffraction spots. Figures 3 (a) and (b) show that the ends of the nanorods are narrow and the nanorods are single crystalline.

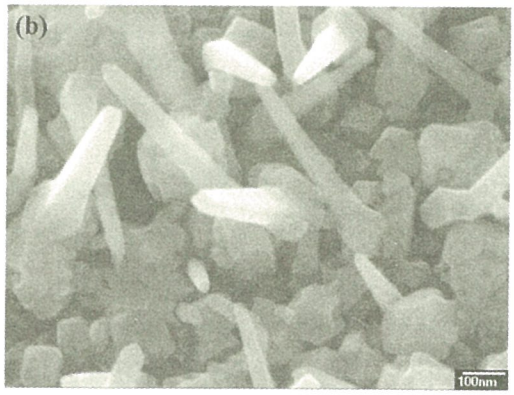

I image of In_2O_3 nanorods, (b) magnified view of (a).

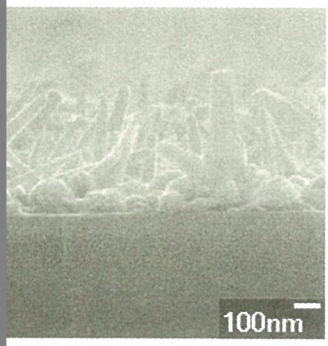

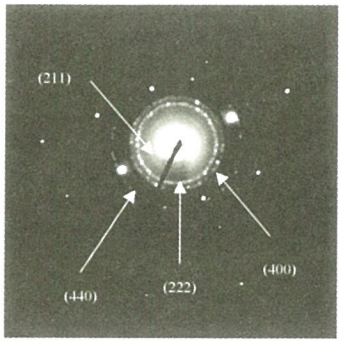

sectional image of (a).

Fig 2. Diffraction pattern of the sample shown in Fig 1

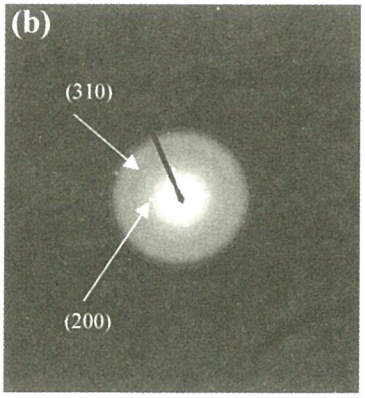

I image of In_2O_3 nanorods. (b) Selection diffraction pattern of (a).

Growth of nanowires on self-assembled hexagonal Au particle networks

CHIANG, Tian-Fu[1](蔣天福); CHENG, Shao-Liang[2](鄭紹良) and CHEN, Lih-Juann[1](陳力俊)

[1]Department of Materials Science and Engineering, National Tsing Hua University, Hsinchu, Taiwan
[2]Department of Chemical and Material Engineering, National Central University, Taoyuan, Taiwan

In recent years, research interest in nanostructures and nanomaterials has grown as a result of their unique electronic, optical, and mechanical properties, which are different from those of the corresponding bulk materials, and thus their potential application in nanoscale electronics and optical devices. SiO_x nanowires, as candidates for photoluminescent materials, have been synthesized by various methods. In the present study, well-defined growth of the SiO_x nanowires at the novel self-assembled hexagonal Au particle networks using a vapor transport process was observed.

Novel self-assembled hexagonal networks with discrete Au particle on different substrate have been synthesized. A vapor transport process was used for the growth of SiO_x nanowires. A mixture of Si and SiO_2 powders in a certain ratio (1:1 Si/SiO_2) was placed in an alumina boat as the source material and positioned at the high-temperature (1200 ^{0}C) zone of the furnace. The nanowires were deposited onto different substrates, which include Si(111) and Al_2O_3 (0001), located at the low-temperature (900 ^{0}C) zone of the furnace. The carrier gas was an Ar flow with the rate of 50 sccm. Morphological characterizations of the samples were carried out using scanning electron microscopy (SEM).

Figure 1 shows the SEM image of the SiO_x nanowires which attach to a single catalytic Au particle. Gold particles display highly catalytic activity for the growth of the nanowires. Figures 2(a)-(e) show the morphology of SiO_x nanowires grown at the fixed position of self-assembled Au particle network on Si(111) substrate for different growth times. After growth at 900 ℃ for 2 h, the short SiO_x nanowires grow on Au particle. After further growth at 900 ℃ for 3 h, more SiO_x nanowires grow and the length of nanowires become longer. The formation process of the nanowires is closely related to a vapor-liquid-solid (VLS) mechanism.

Figures 3(a)-(d) show the morphology of SiO_x nanowires grown at the self-assembled hexagonal Au particle network on Al_2O_3 (0001) substrate for 10 h. Well-defined growth of the SiO_x nanowires at the novel self-assembled hexagonal Au particle networks was observed. The facet of the Au particle was found apparently on the Al_2O_3 (0001) substrate. These morphology on the Al_2O_3 (0001) substrate is different from those on the Si(111) substrate. The above results show that SiO_x nanowires is easier to grow on the Si substrate than on the Al_2O_3 substrate. It is attributed the supply of Si or O element from Si substrate. On the Al_2O_3 substrate, only Si vapor and residual oxygen can promote the growth of the nanowires.

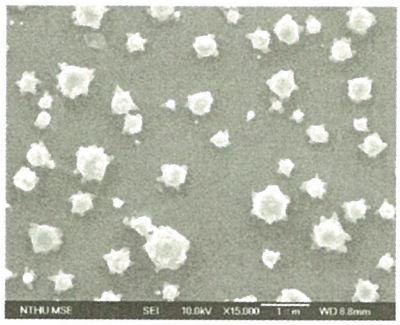

Fig.1 SEM image of the SiO_x nanowires attached to a single catalytic Au particle.

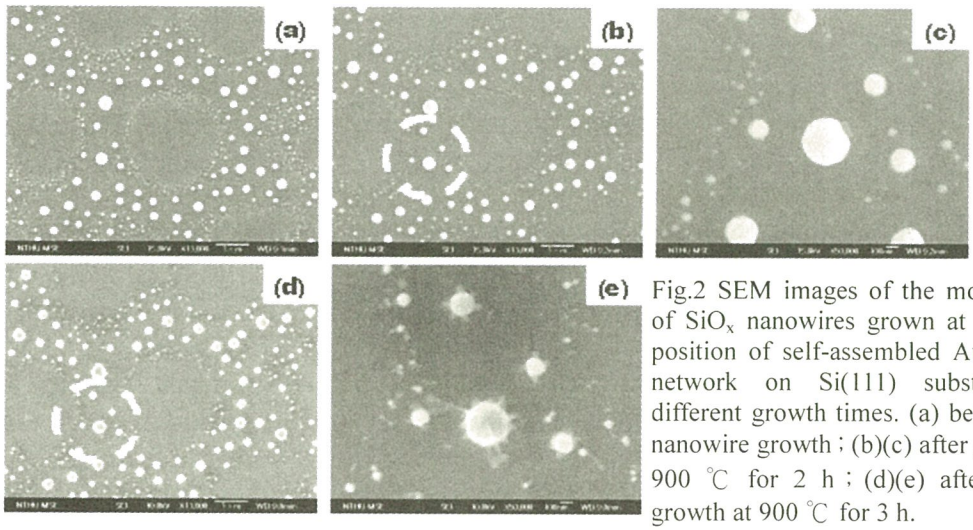

Fig.2 SEM images of the morphology of SiO_x nanowires grown at the fixed position of self-assembled Au particle network on Si(111) substrate for different growth times. (a) before SiO_x nanowire growth ; (b)(c) after growth at 900 ℃ for 2 h ; (d)(e) after further growth at 900 ℃ for 3 h.

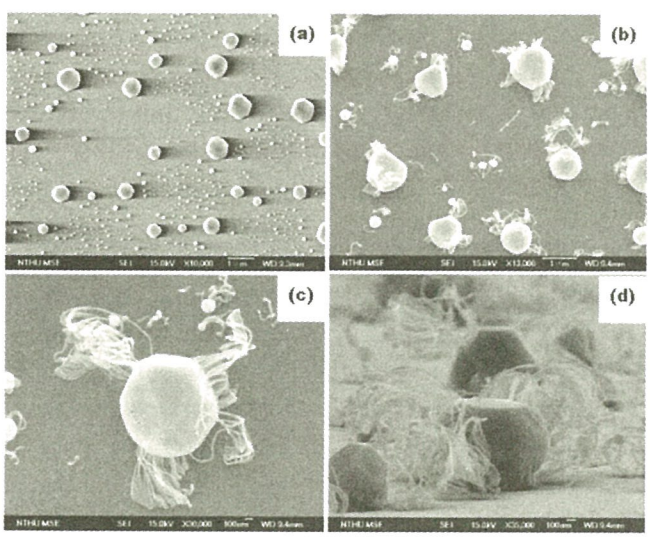

Fig. 3 SEM images of the morphology of SiO_x nanowires grown at the self-assembled hexagonal Au particle network on Al_2O_3 (0001) substrate. (a) before SiO_x nanowires growth ; (b)(c)(d) after growth at 900 ℃ for 10 h.

Growth of Silicon Oxide Nanostructures on Self-Assembled Hexagonal Au Particle Networks on Silicon

SU, Pai-Ying[1](蘇百櫻); LU, Ming-Yan[1](呂明諺); LIANG, Ju-Ming [2](梁鉅銘); CHENG, Shao-Liang[3](鄭紹良); HU, Jung-Chih[1](胡榮治) and CHEN, Lih-Juann[1](陳力俊)

[1]Department of Materials Science and Engineering, National Tsing Hua University, Hsinchu, Taiwan
[2]National Nano Device Laboratory, Hsinchu, Taiwan
[3]Department of Chemical and Material Engineering, National Central University, Taoyuan, Taiwan

Self-assembly is one of the few practical strategies for making ensembles of nanostructures. It will therefore be an essential part of nanotechnology. In this paper, we demonstrate the growth of silicon oxide nanostructures on well-ordered Au particle networks.

Gold nanocrystals were synthesized using a two-phase method. Dispersion solutions of Au nanoparticles were prepared with 5 g of gold nanoparticles/l of toluene. A 10 μl droplet was drop-cast with a micro-pipet on a 5 mm x 5 mm (001)Si wafer and 100-nm-thick SiO_2/(001)Si. The solvent was evaporated while placing the substrate in an air-extracting climate box with appropriate airflow, humidity and temperature. Heat treatments were carried out in a three-zone diffusion furnace in N_2 ambient.

Regular honeycomb network was found to form in drop-cast samples by self-organization with a wide range of conditions. An example is shown in Fig. 1. In samples annealed at 1000 ℃ for 60 min, regular hexagonal Au network was observed to form as shown in Fig. 2.

Two kinds of structures were found in samples annealed at 1100 ℃ for 60 min. The first is like bean sprout at each of the Au particle site and the second is of flowery appearance. Examples are shown in Figs. 3 (a) and (b).

The nanowires were found to be composed of Si and O from the EDS analysis of TEM samples. The bean-sprout-like and flowery structures were found to grow on relatively thin (10 nm) and thick (100 nm) Si oxide, respectively. The bean-sprout-like structure was also found to grow from Au particle on 100-nm-thick SiO_2/Si substrate occasionally.

Figures 4 (a) and (b) show the SEM images of the same area annealed at different temperature in N_2 ambient. It can be clearly seen that, the skeletons of honeycomb were aggregated to the intersections completely with some smaller particles dispersed at the interior of the hexagonal structure after annealing at 1000 ℃ for 75 min as shown in Fig. 4 (a). Regular hexagonal network with cleaner interior was observed after annealing at 1090 ℃ for 30 min as shown in Fig. 4 (b). On the other hand, the interior small Au particles inside the Au particle network may be cleaned up by high temperature annealing since the small particles tended to permeate through the oxide layer.

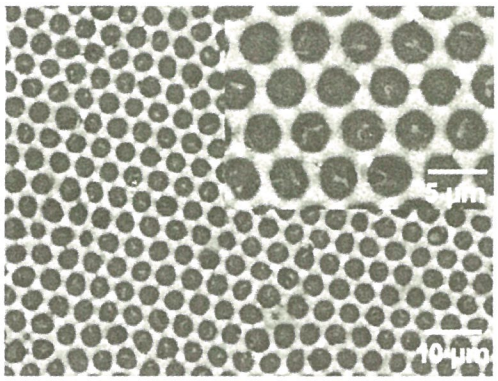

Fig.1 SEM image of a 5.36 g/l Au nanoparticles deposited sample. The inset shows magnified view of selected area.

Fig. 2 SEM image of Au nanoparticles deposited sample annealed at 1000 ℃ for 60 min.

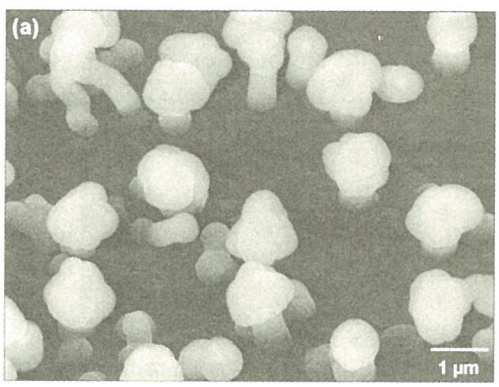

Fig. 3 (a) SEM image of a sample annealed at 1100 ℃ for 60 min showing the bean sprout-like structures.

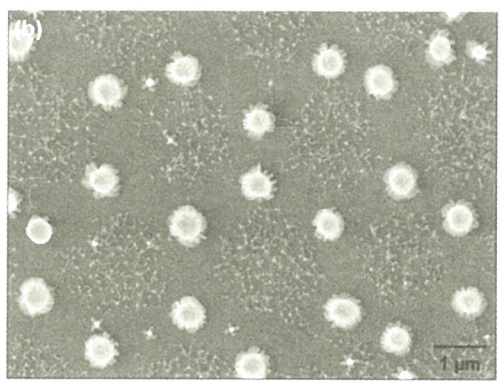

Fig. 3 (b) SEM image of a sample annealed at 1100 ℃ for 60 min with a flower-like structures on Au particles.

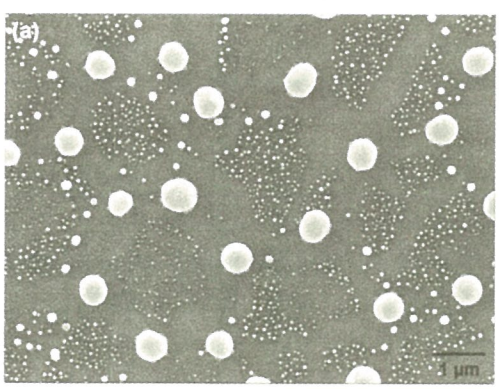

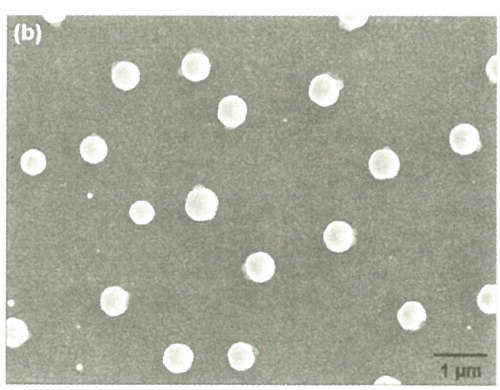

Fig. 4 SEM image of the same area of a sample annealed at (a) 1000 ℃ for 75 min, (b) 1090 ℃ for 30 min.

THE REACTION WOOD OF *Swietenia macrophylla* King

LEE, Chin-Mei (李金梅)[1]; KUO-HUANG, Ling-Long (黃玲瓏)[2]; CHIEN, Ching-Te (簡慶德)[3] and TSAI, Ching-Ju (蔡磬竹)[4]

[1] Division of Forest Utilization, Taiwan Forestry Research Institute; [2] Institute of Ecology and Evolutionary Biology, University of Taiwan; [3] Division of Forest Silviculture, Taiwan Forestry Research Institute; [4] Department of Forestry, National Taiwan University.

Environmental factors may cause the production of wood with special structure and properties. Reaction wood is a variation of normal wood structure that is mostly assumed to be a response to the reorientation of a woody axis from its usual position, whether the cause is natural or artificial. In this work, the formation and structure modification of reaction wood in the horizontally growing 1-2 year trunks of *Swietenia macrophylla* king were studied. *Swietenia macrophylla* formed diffuse porous wood. In the vessel elements of last year wood, tyloses occurred. Some starch grains were found in the ray parenchyma (Fig. 1). The shoot apex of trunks grew upwards obviously after the trunks were laid horizontally. In the curved part of trunks after 4 months horizontal position, tension wood with many gelatinous fibers occurred in the upper side (Fig. 2 and 3), while in the opposite wood only some thin-gelatinous- layered fibers were found (Fig. 4 and 5). Many starch grains occurred in the most ray parenchymatous cells. After 10 months horizontal position, the trunks formed obvious tension wood eccentrically (Fig. 6). The eccentric rate decreased from the basal part to apex of trunks. In the tension wood, almost all the axial fibers were found to be gelatinous fibers. These fibers formed cellulose-rich, thick-gelatinous- layered in the secondary wall, in addition to the usual lignified layer (Fig. 7). Nevertheless, in the opposite wood, fibers were only with the lignified secondary wall (Fig. 8). High tensile released growth strain was measured on the upper surface of the curved part. Gelatinous fibers shorten at maturation and induce longitudinal tension strains in the region of the axis in which they occur. The occurrence of gelatinous fibers and frequent correlation of these fibers with increased tension strains result the movements of trunks[(1)]. It is interesting to note that in the tension wood only few starch grains were found in the axial ray parenchyma, however, in the opposite wood many starch grains occurred. The distribution of carbon source in the tension woods is functionally allocated.

References

(1) Wilson, B.F. and Archer, R. R. 1977. Reaction wood: induction and mechanism of action. Annu. Rev. Plant Physiol. 28: 24-43.

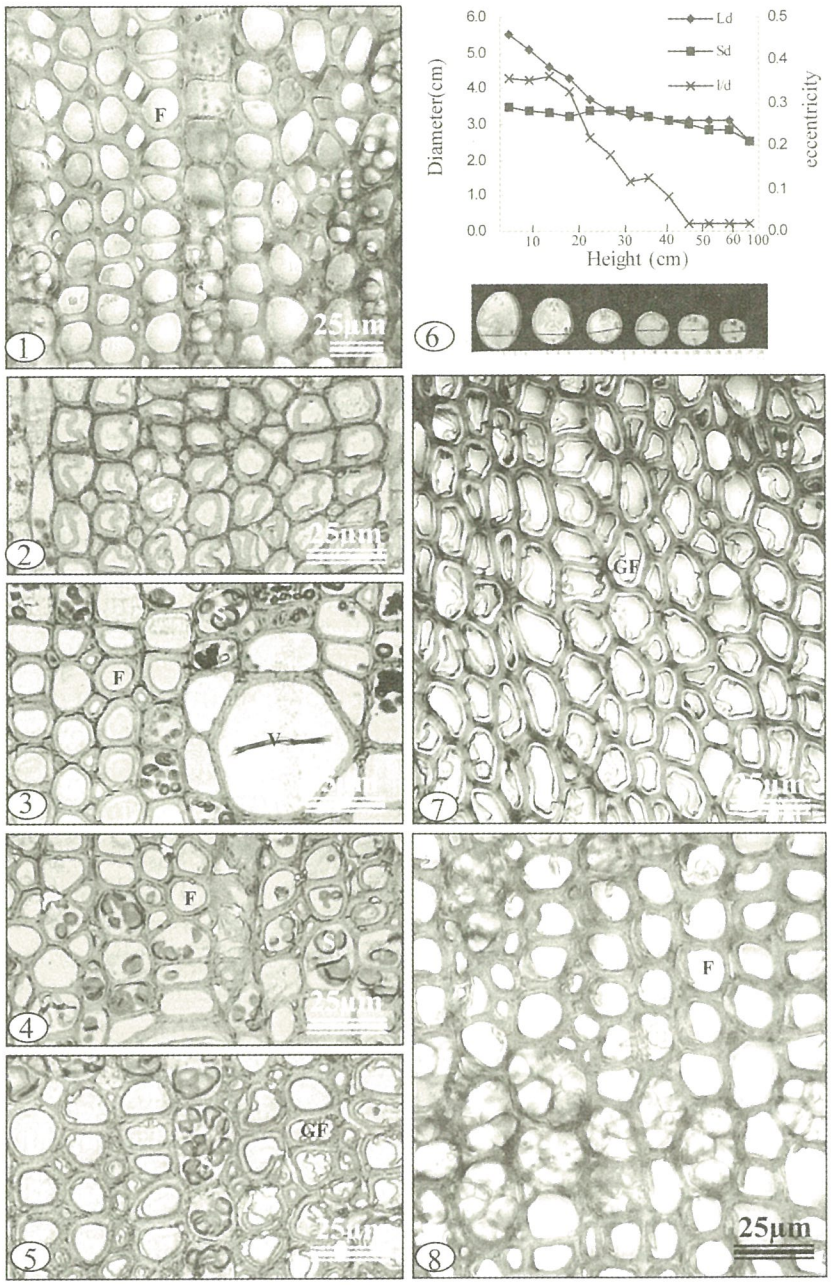

The Light Microscope of *Swietenia macrophylla*

Fig.1. Cross section of the wood in control.

Fig.2 and 3. C.S. of tension wood horizontally positioned for 4months.

Fig.4 and 5. C.S. of tension wood horizontally positioned for 4months.

Fig.6. The trunks horizontally positioned for 10 months with obvious eccentrically tension wood.

Fig.7. C.S. of the tension wood horizontally positioned for 10 months.

Fig.8. C.S. of the opposite wood horizontally positioned for 10 months.

IALITIS VIRUS HELICASE WITH

ang-Jiun(王長君)*

ute of Biology and Anatomy, National
.C.

ito-borne flavivirus and causes a serious
Southeast Asia every year. Nowadays,
important topics of the public-health
n of intracellular membranous
nbrane structure, and membrane vesicle
se JEV-induced structures were rich
reservoirs of viral proteins (1,2).
rotein 3 (NS3) of JEV was associated
rotubule rearrangement during JEV
NS3 that interacts with microtubule,
FP fused with the protease domain of
of NS3 (GFP-NS3 163-619) and the
ressing plasmids were transfected into
od. The GFP alone was localized in the
80 was present dispersive small spots in
ligomerization of NS3 protease. Both
dently distributed with microtubules.
63-619 were co-localized with
ating that the helicase domain of NS3
tubules. Large aggregation was formed
transfection, and meanwhile
n and still together with NS3,
of microtubules. These results
ubules by its helicase domain and

C.T., Huang, Y.L. and Chen, L.K.

, Chiou, C.T. and Chen, L.K. (1998)

C.L., Lin, Y.L. and Wang, J.J. (2003)

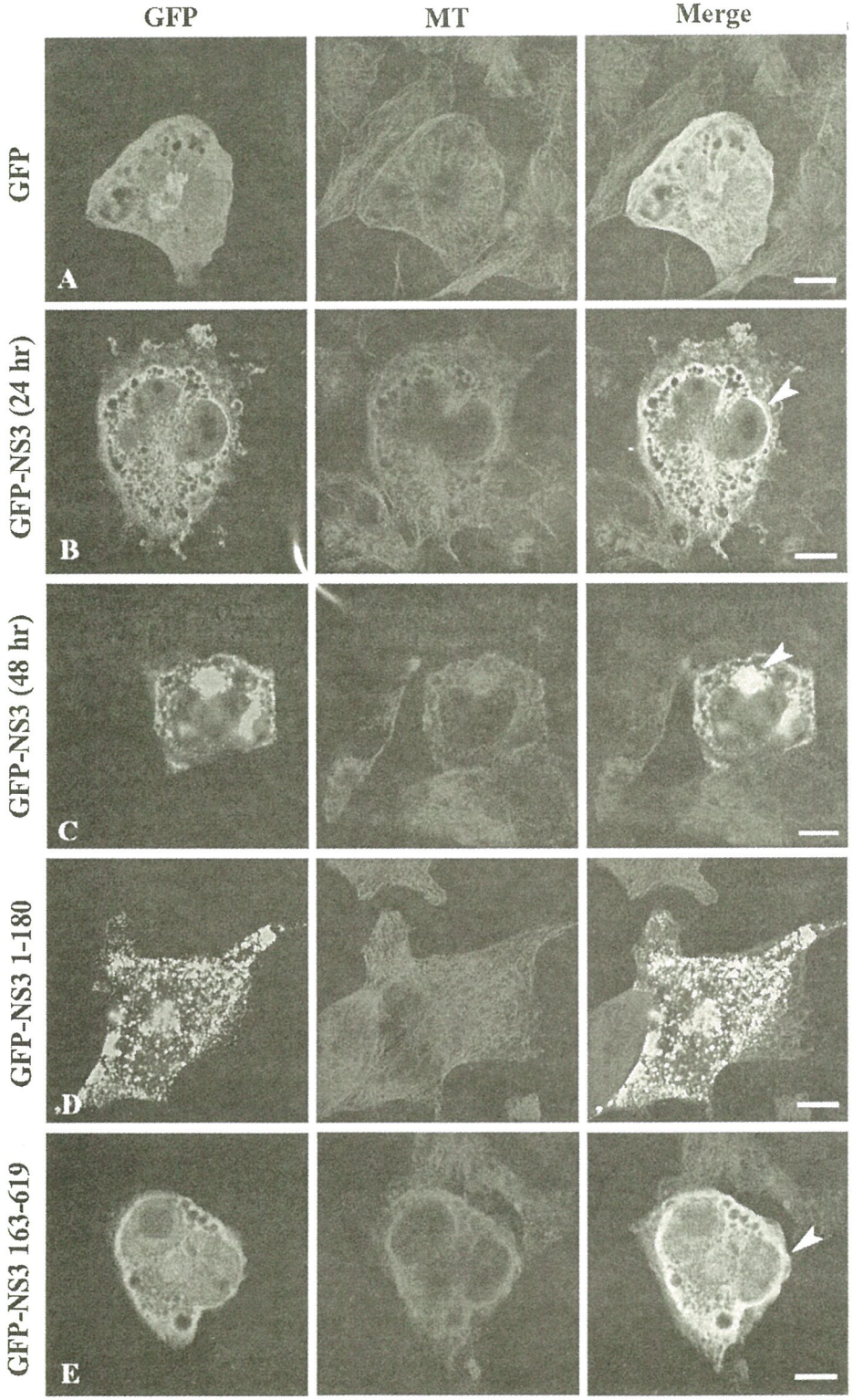
GFP
MT
Merge
GFP
GFP-NS3 (24 hr)
GFP-NS3 (48 hr)
GFP-NS3 1-180
GFP-NS3 163-619
A
B
C
D
E

HISTAMINE-INDUCED PLASMA EXTRAVASATION, EDEMA FORMATION, AND SEROUS CELL SECRETION IN RAT TRACHEA

CHANG, Jui-Hsin (張瑞炘) and HUANG, Hung-Tu (黃宏圖)

Department of Biological Science, National Sun Yat-Sen University, Kaohsiung, Taiwan

The tracheal epithelium of specific pathogen-free rats consists mainly of serous cells and ciliated cells (1). Calcitonin gene-related peptide (CGRP) is present in secretory granules of serous cells (2). Capsaicin degranulates these cells causing release of CGRP into the tracheal lumen (2). The present study sought to investigate the effect of exogenous histamine on plasma extravasation, edema formation, and serous cell secretion in the trachea of rats. A high dose of histamine (18 μ mol/ml/kg) was administered i.v. India ink (1ml/kg) was injected as a tracer to label the leaky vessels. Tracheal whole mounts and tissue sections were processed for light (Fig. 1A & B) and scanning electron microscopy (SEM) (Fig. 1C-F). One hour after histamine, plasma leakage and subepithelial edema (Fig. 1B) was extensive. The area density of India ink-labeled blood vessels was 21.6±1.7% (n=6). Saline, the vehicle of histamine, produced only a little extravasation. In histamine-treated rats, the apical surface of serous cells protruded into the tracheal lumen with many globular elevations and one to several deep pits, which were evidence of granule exocytosis (Fig. 1D-F). It is concluded that histamine triggered the inflammatory response that was associated with the degranulation of serous cells for the exocytotic release of CGRP.

References

(1) Huang, H. T., Haskell, A., McDonald, D. M.; Anat. Embryol. 180 (1989) 325-341.
(2) Baluk, P., Nadel, J. A., and McDonald, D. M.; Am. J. Respir. Cell Mol. Biol. 8 (1993) 446-453

Fig. 1. A: Saline treatment. The mucosal surface epithelium is consisted of serous cells (arrowhead) and ciliated cells. B: Histamine treatment. Edema (*) is prominent and the venule is labeled with India ink (arrow). C: Saline treatment. SEM showed the surface of serous cells (SC) and ciliated cells (CC). D: Histamine caused the serous cells (arrow) to protrude. E: Globules (arrow) and pits on the surface of serous cells after histamine. F: Complex pit after compound exocytosis (arrow).

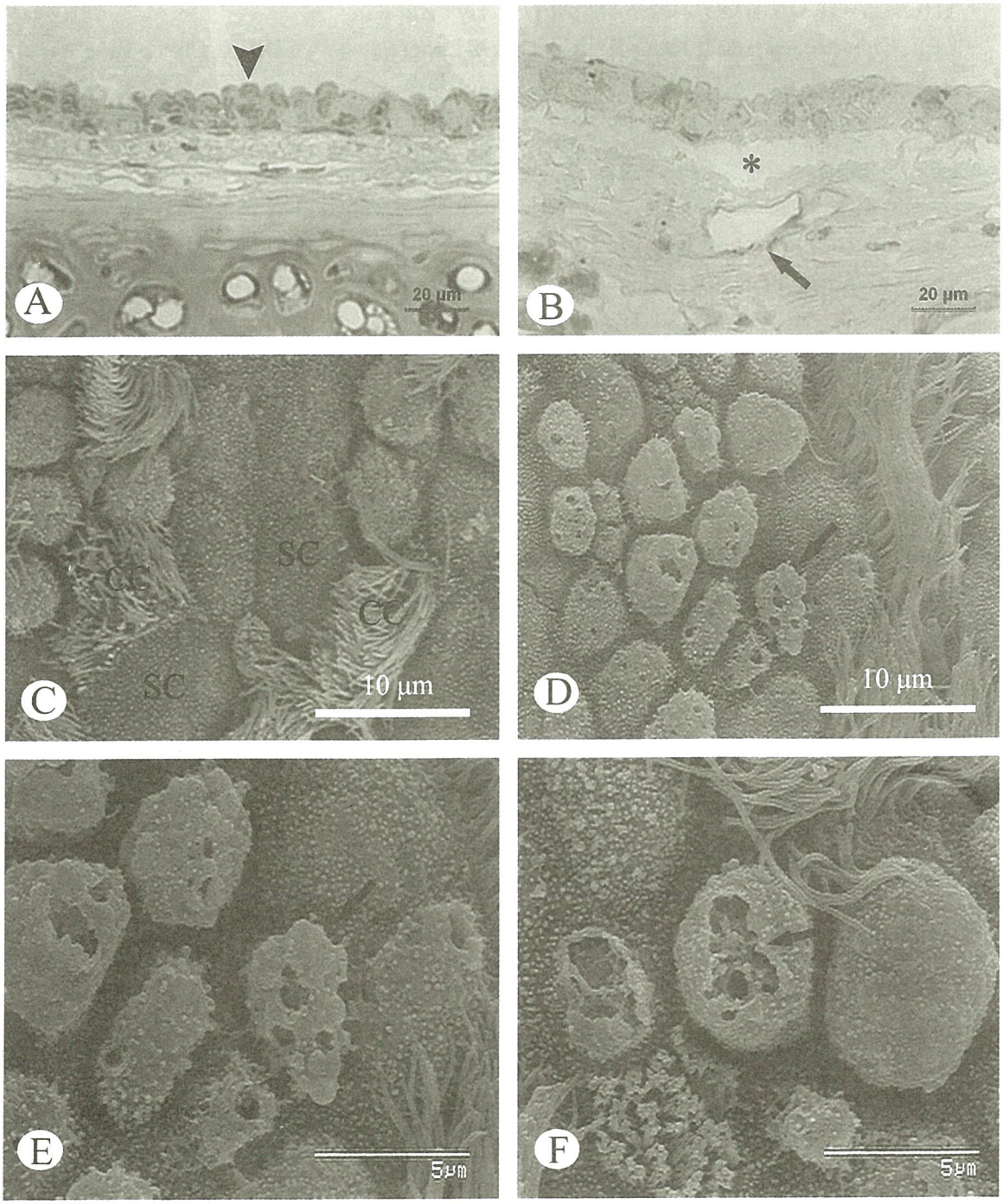
A
20 μm
B
20 μm
C
SC
CC
CC
SC
10 μm
D
10 μm
E
5μm
F
5μm

THE REACTION WOOD OF *Swietenia macrophylla* King

LEE, Chin-Mei(李金梅)[1]; KUO-HUANG, Ling-Long(黃玲瓏)[2]; CHIEN, Ching-Te(簡慶德)[3] and TSAI, Ching-Ju(蔡磬竹)[4]

[1] Division of Forest Utilization, Taiwan Forestry Research Institute; [2]Institute of Ecology and Evolutionary Biology, University of Taiwan; [3]Division of Forest Silviculture, Taiwan Forestry Research Institute; [4]Department of Forestry, National Taiwan University.

Environmental factors may cause the production of wood with special structure and properties. Reaction wood is a variation of normal wood structure that is mostly assumed to be a response to the reorientation of a woody axis from its usual position, whether the cause is natural or artificial. In this work, the formation and structure modification of reaction wood in the horizontally growing 1-2 year trunks of *Swietenia macrophylla* king were studied. *Swietenia macrophylla* formed diffuse porous wood. In the vessel elements of last year wood, tyloses occurred. Some starch grains were found in the ray parenchyma (Fig. 1). The shoot apex of trunks grew upwards obviously after the trunks were laid horizontally. In the curved part of trunks after 4 months horizontal position, tension wood with many gelatinous fibers occurred in the upper side (Fig. 2 and 3), while in the opposite wood only some thin-gelatinous-layered fibers were found (Fig. 4 and 5). Many starch grains occurred in the most ray parenchymatous cells. After 10 months horizontal position, the trunks formed obvious tension wood eccentrically (Fig. 6). The eccentric rate decreased from the basal part to apex of trunks. In the tension wood, almost all the axial fibers were found to be gelatinous fibers. These fibers formed cellulose-rich, thick-gelatinous- layered in the secondary wall, in addition to the usual lignified layer (Fig. 7). Nevertheless, in the opposite wood, fibers were only with the lignified secondary wall (Fig. 8). High tensile released growth strain was measured on the upper surface of the curved part. Gelatinous fibers shorten at maturation and induce longitudinal tension strains in the region of the axis in which they occur. The occurrence of gelatinous fibers and frequent correlation of these fibers with increased tension strains result the movements of trunks [(1)]. It is interesting to note that in the tension wood only few starch grains were found in the axial ray parenchyma, however, in the opposite wood many starch grains occurred. The distribution of carbon source in the tension woods is functionally allocated.

References

（1）Wilson, B.F. and Archer, R. R. 1977. Reaction wood: induction and mechanism of action. Annu. Rev. Plant Physiol. 28: 24-43.

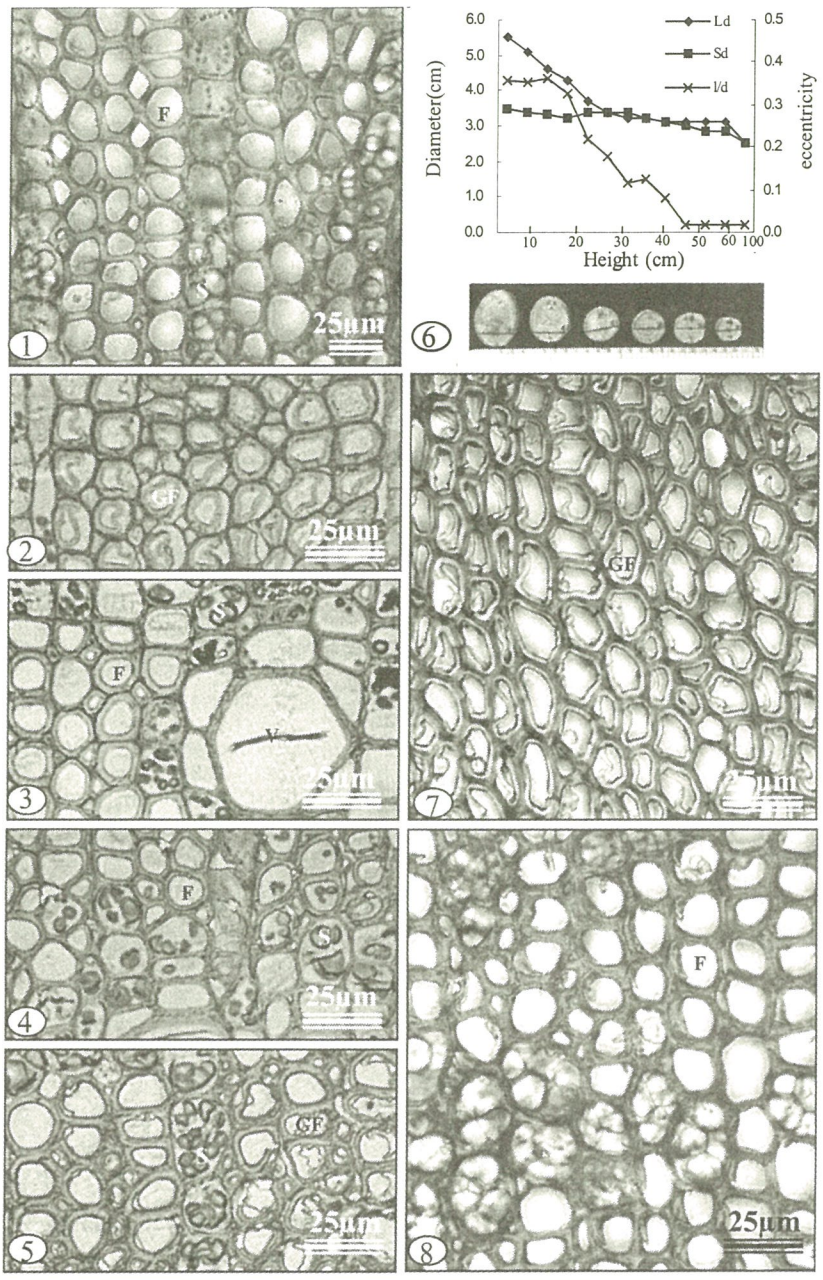

The Light Microscope of *Swietenia macrophylla*

Fig.1. Cross section of the wood in control.

Fig.2 and 3. C.S. of tension wood horizontally positioned for 4months.

Fig.4 and 5. C.S. of tension wood horizontally positioned for 4months.

Fig.6. The trunks horizontally positioned for 10 months with obvious eccentrically tension wood.

Fig.7. C.S. of the tension wood horizontally positioned for 10 months.

Fig.8. C.S. of the opposite wood horizontally positioned for 10 months.

Abortive Pollen In *Salvia japonica* Thunb.

Lee, Yi-Ling (李宜玲) and Chen, Su-Hwa (陳淑華)

Department of Life Science, National Taiwan University, Taipei, Taiwan.

Salvia japonica Thunb. occurs in China, Japan and the northern Taiwan. Its pollen viability was less than 30%. During simultaneous cytokinesis, the normal tetrad with four cells (Fig.1) and the abnormal penta, hexad (Fig.2), and octad with more than four cells can be found. Three nuclei can be detected in the mature fertile pollen grain (Fig.3) and only one nucleus (Fig.4) or no prominent DNA content (Fig.5) can be detected in the abortive pollen grain in the DAPI test. In FCR test, some tetrads were with all four cells viable (Fig.6), while some were only one, two, three or none viable (Fig.7). This phenomenon occurred also in pentad (Fig.8), hexad or octad (Fig.9). There was a dramatic change in pollen viability before (Fig.10) and after (Fig.11) anthesis. The abortive pollen grain was different from the fertile one for their morphology (Fig.12, 14), exine ornamentation (Fig.13, 15) and DNA content. Furthermore, the contents of protein (Fig.16), lipid (Fig.17) and polysaccharides (Fig.18) in the abortive pollen were lower than the fertile one. It is suggested that the occurrence of abortive pollen grains was influenced by the abnormality of cytokinesis and metabolism.

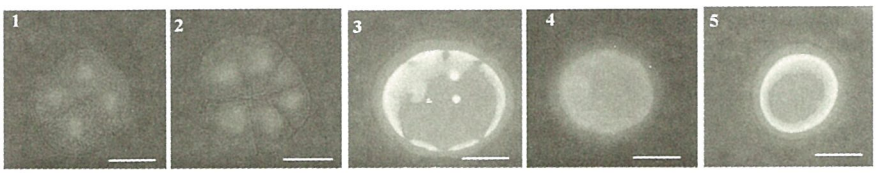

Fig.1-5. DAPI test. Fig.1. a tetrad with four cells. Fig.2. a hexad with six cells. Fig.3. a fertile pollen grain with three nuclei. Fig.4. an abortive pollen with one nucleus. Fig.5. no detection of DNA in an abortive pollen. (Fig.1 & 2. bar=3μm; Fig. 3-5. bar=25μm)

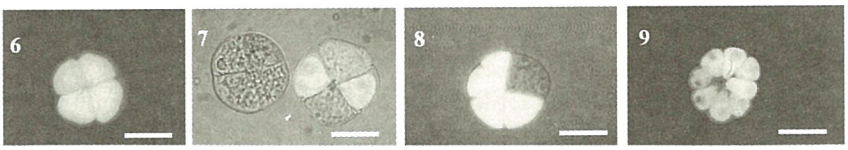

Fig.6-9. FCR test. Fig.6. four cells in a tetrad viable. Fig.7. none or two of four cells in tetrads viable. Fig.8. four of five cells in a pentad viable. Fig.9. eight cells in an octad viable. (Fig.6-9. bar=3μm)

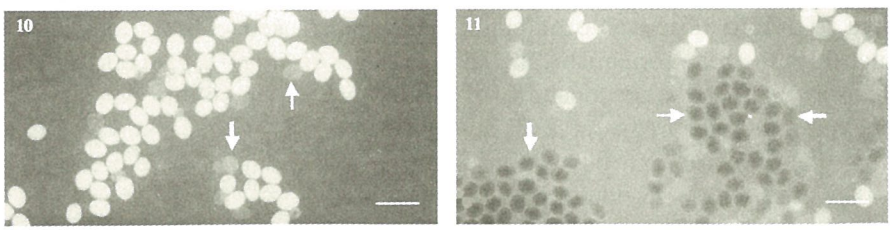

Fig. 10 & 11. FCR test. Fig.10. before anthesis. most pollen grains viable and a few unviable (→). Fig.11. after anthesis. most pollen grains unviable (→) and a few viable. (Fig.10 & 11. bar=100μm)

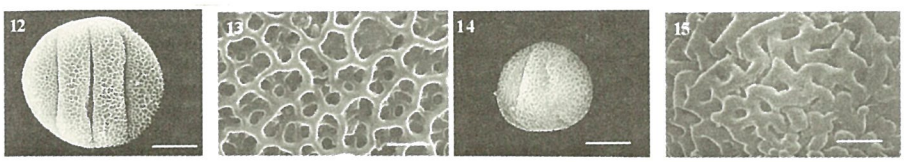

Fig.12-15 SEM. Fig.12. a fertile pollen grain in equatorial view. Fig.13. high resolution of reticulate exine of Fig.12. Fig.14. an abortive pollen grain in equatorial view. Fig.15. high resolution of compactly rugulo-reticulate exine of Fig.14. (Fig.12. bar=4μm; Fig.13. bar=1.5μm; Fig.14.

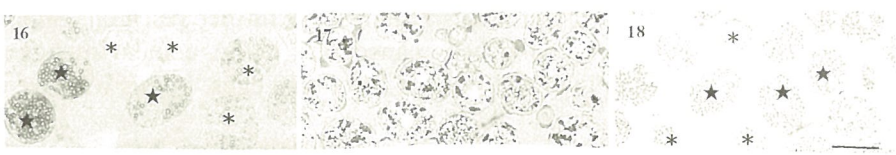

Fig.16-18. LM. at pollen maturation stage. Fig.16. Coomassie brilliant blue test: fertile (★) and abortive (*) pollen grains. Fig. 17. Sudan black test: fertile (☆) and abortive (*) pollen grains. Fig.18. PAS test: fertile (★) and abortive (*) pollen grains. (Fig.16-18. bar=20μm)

UTILIZATION OF HIGH POLYUNSATURATED FATTY ACIDS CONTENT MICROALGAE SUPPLEMENT IN POULTRY DIETS

LIU, Ching-Piao (劉清標)[1]; LIN, Liang-Ping (林良平)[1]; GING, Hong-Rong (金鴻榮)[2] and DING, Shih-Torng (丁詩同)[2]

Department of Biochemical Science and Technology[1], Department of Animal of Science[2], National Taiwan University, Taipei, Taiwan 106

The ω-3 Polyunsaturated Fatty Acids (PUFAs) of algae are one of the important resources in the marine food chain. Utilization of algal DHA oil in poultry diet can also enhance yolk DHA content. Because the cost of algal DHA oil is high, their practicability's need to be improved. This research is designed to examine strains of PUFA-rich microalgae or other microorganism for oil production, and establish simple and proper cultural methods of microorganism to produce this bio-product for poultry diet. The bio-product can supply inexpensive PUFA to raise value of egg products. We used concentrations of 0, 1, 3 % bio-product from the microorganism, such as *Thraustochytrium roseum* added to the diets for leghorn hens to estimate the practicability of this bio-product in poultry diets. We recorded the egg production and collect eggs at 1, 2, 3 week for yolk fatty acid composition analysis. At the end of the experiment, the poultries were killed and the expression of hepatic lipogenesis-related genes was determined.

The structural and morphological changes during the lipid formation of the *Monodus subterraneus* UTEX 151 and *Mortierella elongate* NRRL 5513 were observed by light (Fig. 1) and transmission electron (Fig. 2) microscopy. The methods for extraction of lipids from microalgae, analysis of broth and cultural conditions that affected yields of PUFAs, and their PUFA content in the total acids were investigated. Optimum culture temperature and initial pH for EPA production were 25℃ and 8.0, respectively. The EPA yield increased with cultivation time until 8th day. During culturing periods, *Monodus subterraneus* UTEX 151 revealed the structures might be associated with lipid synthesis, and might be an indication for microalgae production of these fatty acids. In conclusions, a sufficient for mass culture of microorganisms to produce this bio-products requires the further research. Supplements of these bio-products in the diet of laying hens can enrich PUFA content of egg yolk. This method produce a low cost and high DHA content functional eggs. In this way, we can get the higher value of egg products.

References

1. Bajpai, P. K.; Bajpai, P. and Ward, O. P.; J. Indust. Microbiol., 1992 (9) 11-18.
2. Cohen, Z.; J. Am. Oil Chem., 1994 (71) 9: 941-945.
3. Lewin, N. M.; Seburg, S. and Flanagan, N. L.; Poultry Sci., 2000 (79) 971-974.
4. O'Leary, W. M.; Microbial Lipids. The Word Pub. Co. Cleveland. 1967.
5. Hoppert, M. and Holzenburg, A; Electron Microscopy in Microbiol. BIOS, UK 1998.

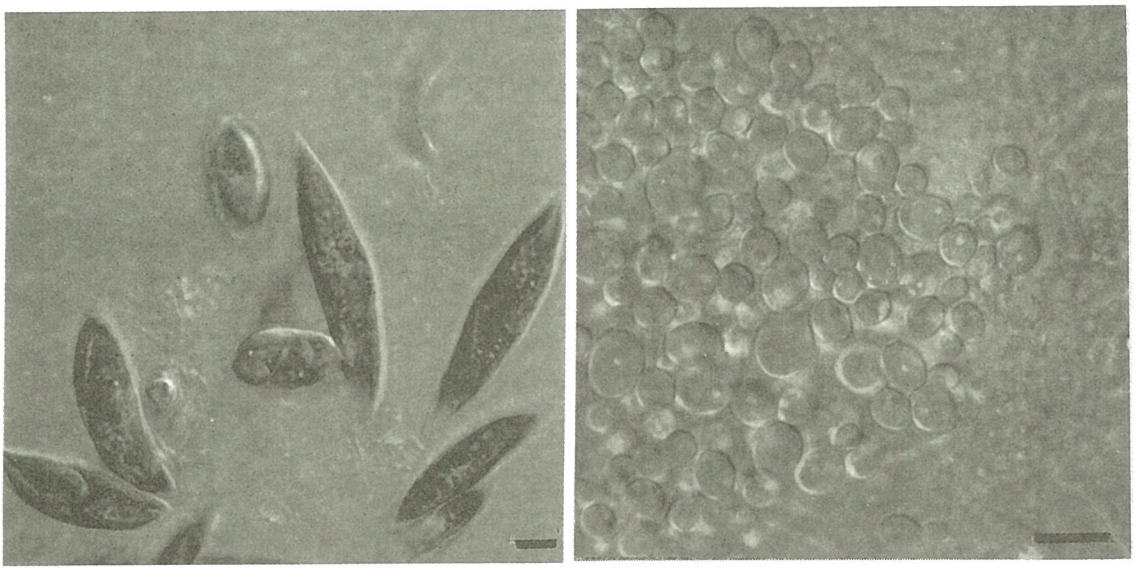

Fig.1. Observations on *Monodus subterraneus* UTEX 151 and *Mortierella elongate* NRRL 5513 in Nomarski interference microscope. Scale bar = 2 μm

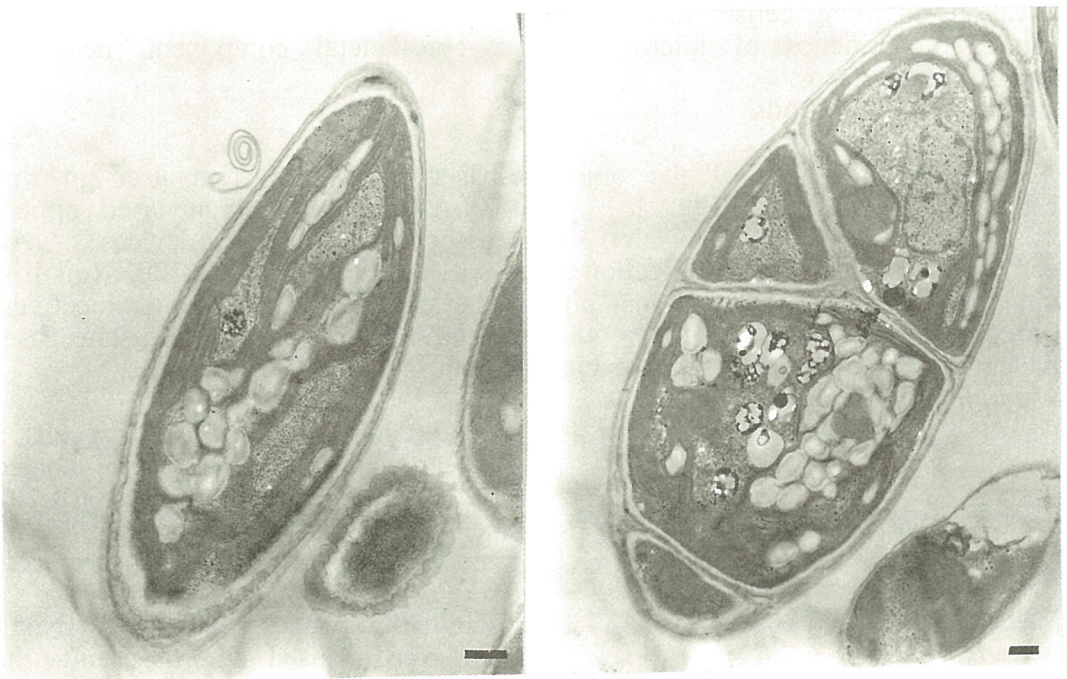

Fig.2. Transmission electron micrographs of *Monodus subterraneus* UTEX 151. Scale bar = 500 nm

PROBING MICROTUBULE KINETICS AND VESICLE ENDOCYTOSIS IN LIVING CELLS USING TOTAL INTERNAL REFLECTION FLUORESCENCE MICROSCOPY

Chen, Chien-Hua [1]; Yu, Shu-Jung [2]; Lin, Chi-Hung [1, 3] and Tsai, Din Ping [2]

[1]Institute of Biophotonics, [3]Institute of Microbiology and Immunology,
Nation Yang Ming University, Taipei 10617, Taiwan, R.O.C
[2]Department of Physics, Nation Taiwan University, Taipei 10617, Taiwan, R.O.C

1. Introduction

The uses of total internal reflection fluorescence microscopy (TIR-FM) in life science studies have shed light on important cellular processes taking place near the plasma membrane. The technique provides a convenient way to excite, and therefore to visualize, fluorephores at the cell-substrate interface. The principle of TIR-FM is based on surface evanescent field that occurs when light is internally reflected at the interface of two media of different refraction indices. Because the intensity of evanescent field decays exponentially as a function of distance, excitation of fluorescent molecules only takes place in a near-zone (~100-200 nm) close to the interface, resulting in a very high signal to noise ratio (SNR) at that specific nano-scale depth.

TIR-FM is particularly useful for studying growth substrate-associated cellular activities at a molecular resolution. The rapid decay of evanescent field significantly reduces photo-damages to the bio-samples, enabling researchers to perform long-term observations in living cells. In this report, we have used TIRFM to monitor, in real-time, the kinetics of microtubules, a cytoskeletal component, near the cell-substrate interfaces.

2. Materials and methods

Microscopy

A schematic view of the objective-based TIRFM system used in this investigation is shown in Fig. 1. The system consists an inverted optical microscope (IX70, Olympus Inc.) and associated imaging devices. An objective-based total internal reflection setup was constructed using 100X (oil Iris, Olympus) or 60X (BFP1, Olympus) high numerical aperture (NA) oil objectives. An argon-ion laser (wavelength = 488nm) and a diode-pump solid-state laser (wavelength = 532nm) were used as excitation light sources.

Bio-sample preparations

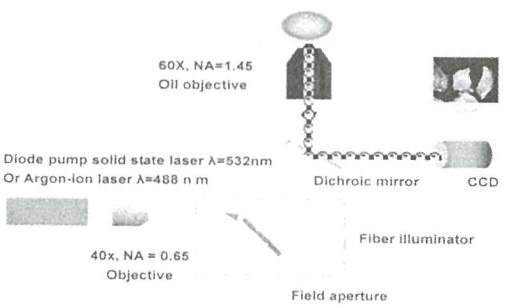

Figure 1. Schematic of the experimental setup.

CHO (Chinese Hamster Ovary) cells, a cancerous cell line. GFP-labeled β-tubulin gene was expressed in CHO cells via a pEYFP vector using conventional transfection protocols (Lian et al., 1999).

The macrophage cell (ATCC Num: TIB-67) is used for observing the cellular endocytosis. We loaded the Lectin Concanavalin (fluorescein labeled) to the cell culture medium,

and we could observe the endocytosis according to the movement of fluorescence spots.

3. Results and Discussions

Typical images of a living CHO cell containing fluorescently labeled microtubules were obtained by either epi-fluorescence (Fig. 2a) or TIRFM mode (Fig. 2b). Note the relatively fuzzy picture of microtubule distributions under the epifluorescence microscope, which is due mainly to the "whole-mount" view of the microtubule structures, as well as the soluble tubulin proteins present in the cytosol. Microtubule organization centers (MTOC) were readily discernible (*arrow*, Fig. 2a). The same cell under TIRFM, on the other hand, exhibited a much clearer picture where individual microtubules near the growth substrate could be resolved (Fig. 2b). Using TIRFM, we were able to visualize the progress of an important kinetic process of microtubules, the dynamic progression (Fig. 3), where a single microtubule was noted to initially undergo a relatively slow growing phase (*arrows*), then went to the catastrophe phase that was characterized by a rapid shrinking, or depolymerization of that specific microtubule (*arrowhead*). We could also observe the cellular endocytosis clearly within the several hundred nano-meter.

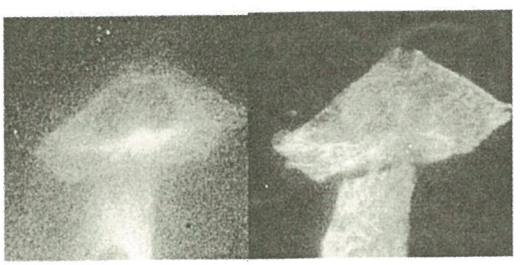

Figure 2. (a) An Epi-fluorescence image of a living CHO cell, containing fluorescently labeled microtubules. (b) The same cell was visualized under TIR-FM.

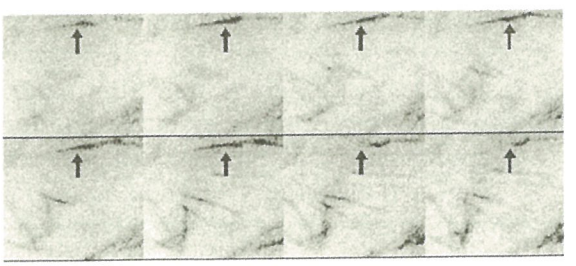

Figure 3. Sequential TIRFM images showing dynamics of microtubules kinetics in a living CHO cell . Time interval=6sec

4. References

(1) Danial A. Methods in Cellular imaging. p.362-p.380 (1989)
(2) Thompson NL and Lagerholm BC. . Curr. Opin. Biotechnol. 8:58-64(1997)
(3) Derek T and Diermar JM. Trends in cell bio. Vol. 11 No.7 (2001).
(4) Steyer J.A. and Almers W. Nature Rev. Mol. Cell Bio.2,268-275(2001)

PURIFICATION, CHARACTERIZATIO N AND IMMUNOLOCIZATION OF HYDROLYTIC ENZYMES IN *RHIZOBIUM FREDII* CCRC15769

HU, Chung-Yi[1]; Hsu, Cheng-Ling[2], WANG, Jaang J[2] and LIN, Liang-Ping[3]
[1]Department of Nutrition and Health Science, Fooyin University, Kaohsiung.
[2]Department of Biology and Anatomy, National Defense Medical Center, Taipei. [3]Graduate Insistute of Agricultural Chemistry, National Taiwan University, Taipei.

Hydrolytic enzymes in rhizobia provides the function of the first entrance of rhizobia into legume plant. Carboxymethyl cellulase (CM-cellulase, EC 3.2.1.4) may be the key enzyme in this symbiotic process, with polygalacturonase (pectinase, EC 3.2.1.15) another critical enzyme involved early in the mechanism of nitrogen supply. After sonication of the cell pellet, ammonium sulfate precipitation, ion-exchange chromatography and electroelution are the preferred methods for derivation of the purified protein, with CM-cellulase characterized as follows: purification fold, 36.30; recovery, 9.8%; and specific activity, 0.053 U mg^{-1}. Two CM-cellulase isozymes were determined from native activity stain assay, with gel filtration revealing molecular weights of approximately 196 and 30 kD; the SDS PAGE activity gel resolved four enzyme subunits of 94, 67, 37, and 30 kD. It is suggested that the CM-cellulase in *S. fredii* CCRC15769 is a two-isozyme form, one a trimer of 196 kD (94, 67 and 37 kD), and the other a 30 kD monomer.

Electron microscope immunogold-labeling experiments for CM-cellulase labeling were performed using ultrathin sections of *Sinorhizobium fredii* CCRC15769. Specific immunogold labeling was not detected in *Bradyrhizobium japonicum* USDA110, however, it was observed in *S. fredii* USDA205, *R. meliloti* ATCC9930, *R. loti* ATCC33669, and *R. leguminosarum* bv. *viceae* ATCC 10004. Preliminary results indicate that antigenic determinants of membrane-bound carboxymethyl cellulase are exposed to the periplasmic space surrounding the cytoplasmic membrane, with the 10-nm immunogold particles hardly ever observed in the cytoplasm or other intracellular spaces. Flavonoid genistein induction in the early log phase of *Sinorhizobium fredii* CCRC15769 caused the aggregiation of CM-cellulase towards two sites of cell, and the plant-rhizobia infection pictures revealing the critical role of the enzyme in the early symbiosis.

References

Mateos, P.F., Baker, D.L., Petersen, M., Velazquez, E., Jimenez-Zurdo, J.I., Martinez-Molina, E., Squartini, A., Orgambide, G., Hubbell, D.H., Dazzo, F.B. 2001 Erosion of root epidermal cell walls by *Rhizobium* polysaccharide-degrading enzymes as related to primary host infection in the *Rhizobium*-legume symbiosis. *Canadian Journal of Microbiology* 47: 475-487.

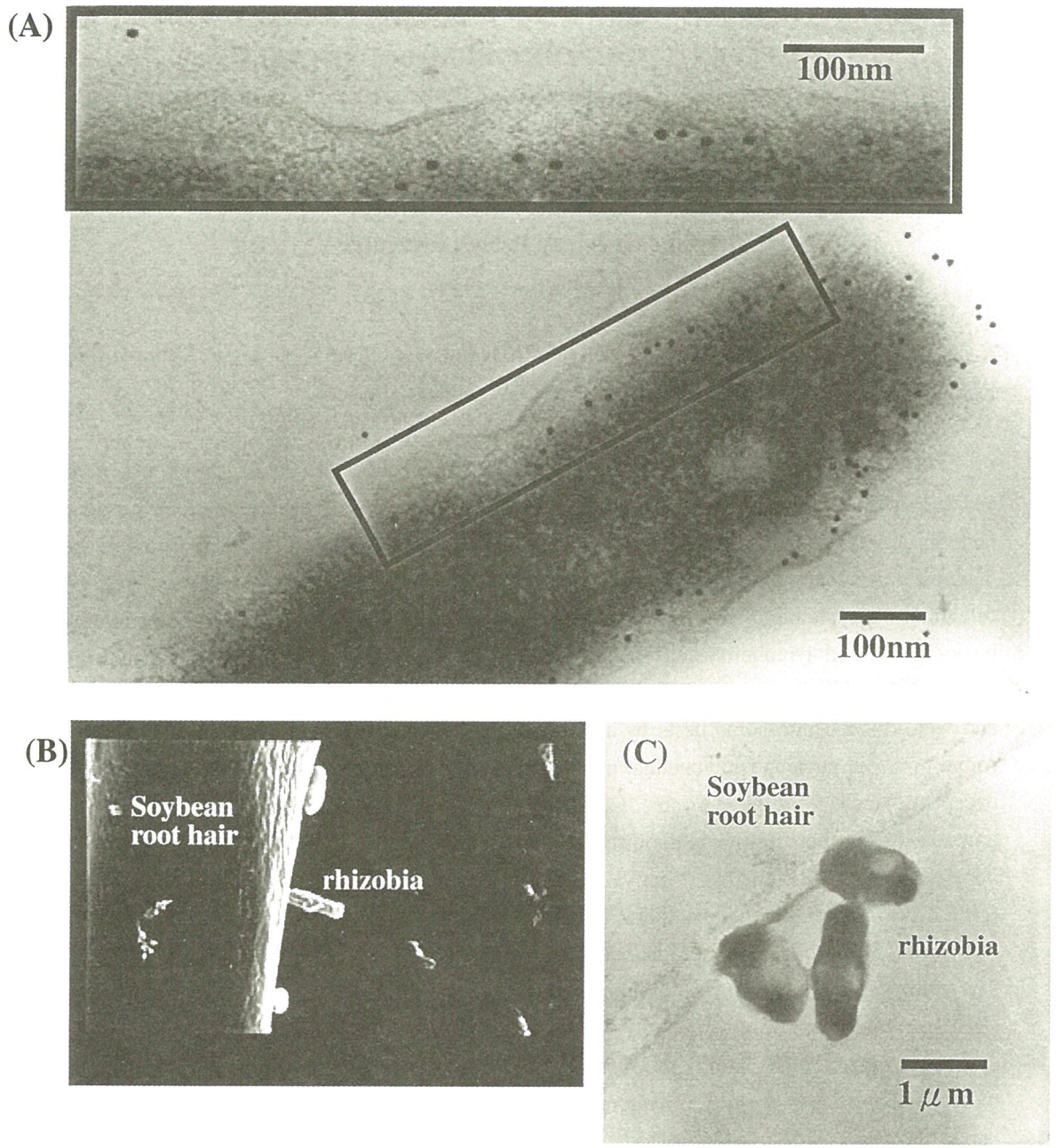

Figure (A). Transmission electron micrograph of ultrathin sections of partial gold-labeled bacteria cell with *Sinorhizobium fredii* CCRC15769 using immunogold-labeled procedures. CM-cellulase of the gold-labeled (10 nm) bacterial cell, provide preliminary indication that the antigen determinants of CM-cellulases are mostly exposed to the periplasmic space on the outside of the cytoplasmic membrane. Bar represents 100nm. Figure (B). Scanning electron micrograph of plant-rhizobia (*S. fredii* CCRC15769) infection pictures. Bar represents 1 μ m. Figure (C). Transmission electron micrograph of ultrathin sections of plant-rhizobia (*S. fredii* CCRC15769) infection pictures. Bar represents 1 μ m.

E ROUND CELLS
SCOPY

thology,
niversity

oma, mast cell tumor, histiocytoma,
nations.

nereal tumor (TVT), lymphoma, mast
the dog. Because their histological
find a method for making a precise
can be specifically differentiated by
TVT cells were compared with
unohistochemical and ultrastructural
arranged compactly or grew in cords
nnective tissue. The cells contained a
result was found in the histiocytoma
phoma cells were round with various
g, both TVT and histiocytoma cells
n, S-100, and neuron-specific enolase
. In ultrastructural observation, the
with one or two prominent nucleoli.
ondria, rough endoplasmic reticulum
Many microvilli protruded from the
acent cells. In degenerated cells, the
nitochondrial swelling. On the other
plasm with a moderate number of
ytoplasm and few organelles only.
chemical and electron microscopic
ures are the most differential among
transmission electron microscopy is

"Diagnostic immunohistochemistry
5-499.

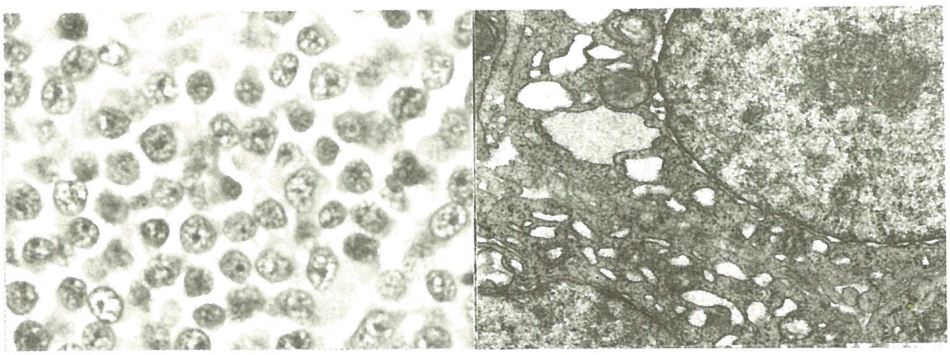

Fig. 1. The histological and ultrastructural pictures of TVT cells .

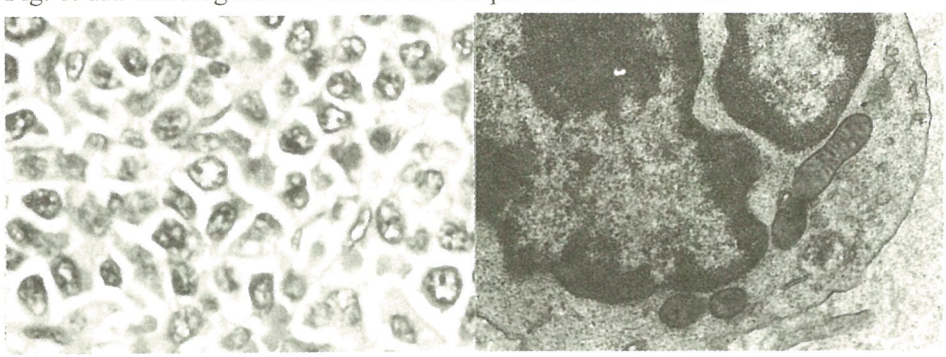

Fig. 2. The histological and ultrastructural pictures of lymphoma cells .

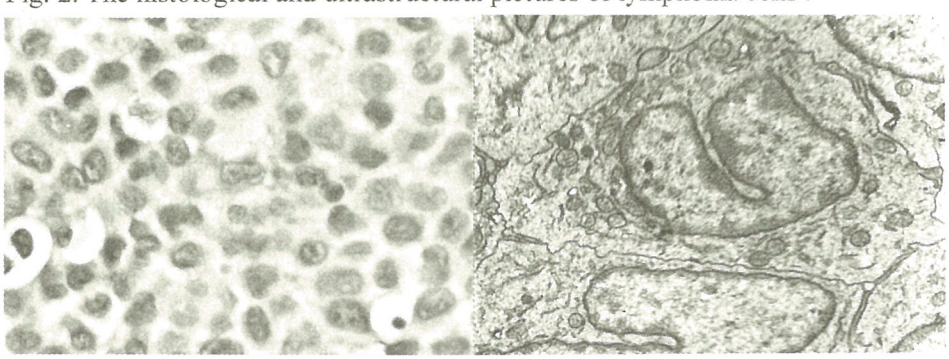

Fig. 3. The histological and ultrastructural pictures of histiocytoma cells .

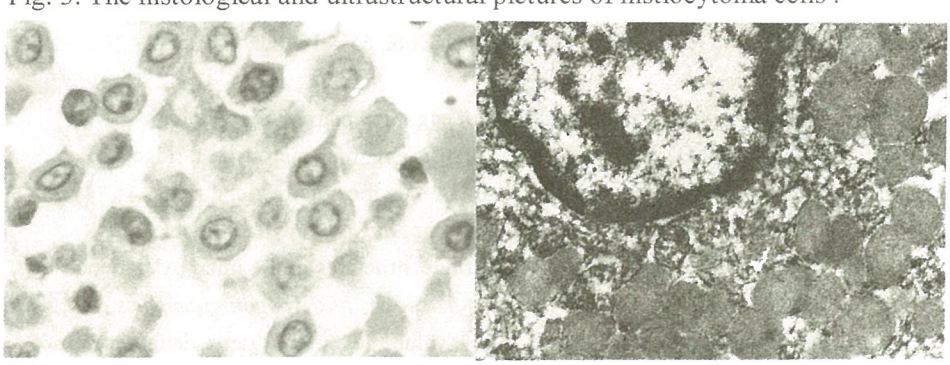

Fig. 4. The histological and ultrastructural pictures of mast cells .

COMPARATIVE ULTRASTRUCTURAL STUDIES OF THE EGG SURFACE OF APOGONIDAE.

CHEN, Chia.-Hsuan.[1] ; WU, Chun- Chun[2] and YANG, Jui- Sen[1]

1. Institute of Marine Biology, National Taiwan Ocean University, 202 Keelung, Taiwan.
2. Department of Applied Mathematics, Feng Chia University, Taichung, Taiwan.

Fish egg intensity is important in studing fish popalation in reefs as well as ocean. Egg shape, pigment, size etc. by light microscopy were used for egg identification in observing egg intensity. However, electron microscopy became a new technique for examining egg ultrastructural features. The ultrastructural features of egg chorion surface are used as a criterion for the identification of fish eggs.

Apogonidae are popular fishes in Taiwan coast reefs. In this work the surface features of the eggs of Apogonidae including *Apogon lateralis*, *A. aureus*, *A. nitidus*, *A. cookii* and *A. guamensis* were studied by scanning electron microscopy. Egg surface ultrastructures including egg size, the length and the number of attaching filament, and the diameter of micropylar region were examined. ANOVA and Scheffe's test were used to analyze the difference among the eggs of five fishes. The ultrastructural characters were significantly different among the eggs of the five fishes. Taxonomic key for identifying the five species of Apogonidae based on egg surface ultrastructures was similar to that based on fish body characteristics in conventional studies although the positions of *A. nitidus* and *A. guamensis* in the key based on the egg were different from that on the body characteristics. Conclusively, with ANOVA and Scheffe's test the ultrastructural characteristics of egg chorion surface were useful characters for egg identification and phylogenetic inference.

References:

(1) K. C. Chen, K. T. Shao and J. S. Yang, 1999. J. Fish Biol. 55: 288-300.
(2) Y. H. Li, C. C. Wu and J. S. Yang. 2000. J. Fish Biol. 56: 615-621.
(3) R. Riehl and R. A. Patzner, 1998. Ital. J. Zool. 65: 415-420.

Fig.1 Micropylar region of *Apogon cookii* egg, mc, micropyle; r, ridge.
Fig.2 Micropylar region of *Apogon guamensis* egg, mc, micropyle; r, ridge.
Fig.3 Micropylar region of *Apogon nitidusis* egg, mc, micropyle; r, ridge.
Fig.4 Micropylar region of *Apogon aureus* egg, mc, micropyle; r, ridge.
Fig.5 Box plot of the longest length of ridge structures in the micropylar region of *Apogon spps*. AA, *A. aureus*; AC, *A. cookii*; AG, *Apogon guamensis*; AL, *A. lateralis;* AN, *A. nitidus*. Mean values with the same letters are not significantly different ($p>0.05$).

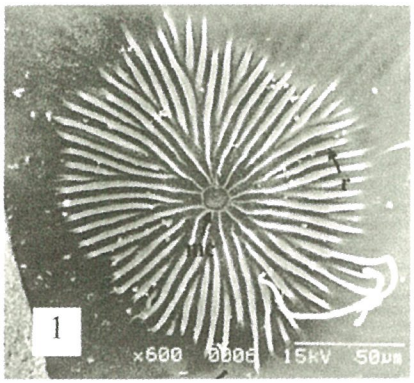
r
mc
1
×600 0006 15kV 50μm

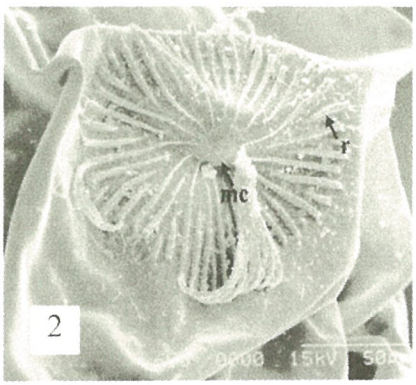
r
mc
2

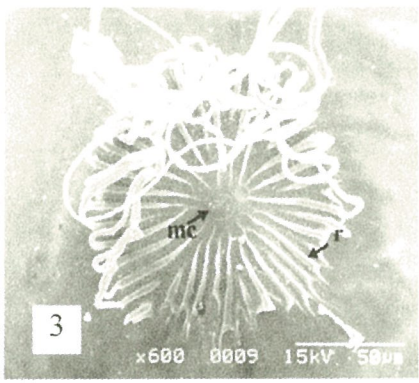
mc
r
3
×600 0005 15kV 50μm

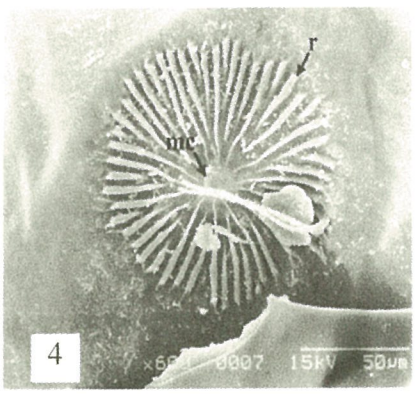
r
mc
4
0007 15kV 50μm

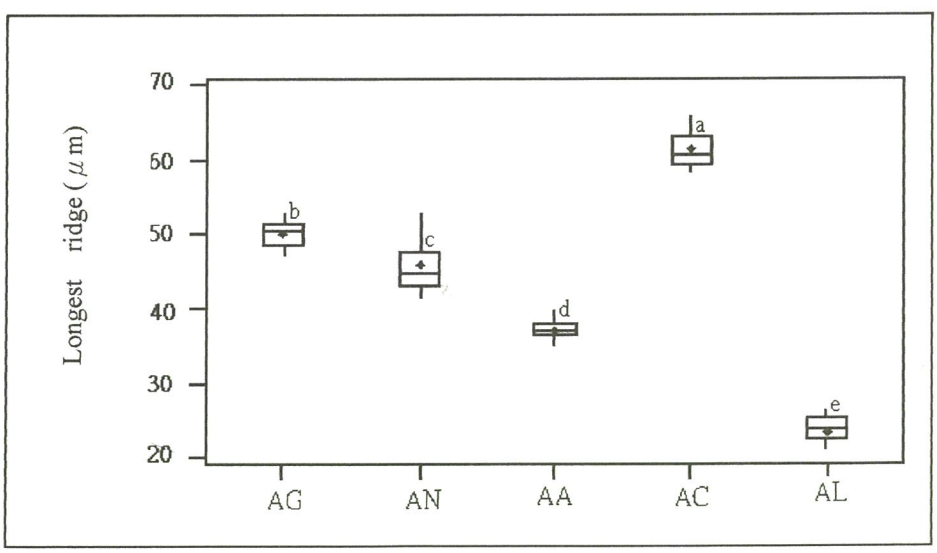
Longest ridge (μm)
70
60
50
40
30
20
a
b
c
d
e
AG
AN
AA
AC
AL

5

廣　　告

廣告廠商索引

感謝下列廠商贊助本屆顯微鏡學術年會

	公 司 名 稱	地　　址	電　話
1	友聯光學有限公司	台北市基隆路一段186號9樓之4	2763-9031
2	台灣儀器行股份有限公司	台北市南京東路三段272號9樓	2772-3333
3	捷東股份有限公司	台北市忠孝東路一段112號7樓	2395-2978
4	技邦企業股份有限公司	台北市士林區大南路354號1樓	2882-5585
5	汎達科技有限公司	新竹市光復陸路二段295號8樓之2	(03)5728466
6	嘉威國際有限公司	台北市北投區石牌路二段17巷90號5樓	2825-0747

(依先後登記順序排名)

顯微鏡共軛焦升級模組

技邦公司提供您最經濟的解決方案，讓您輕鬆擁有Confocal顯微鏡

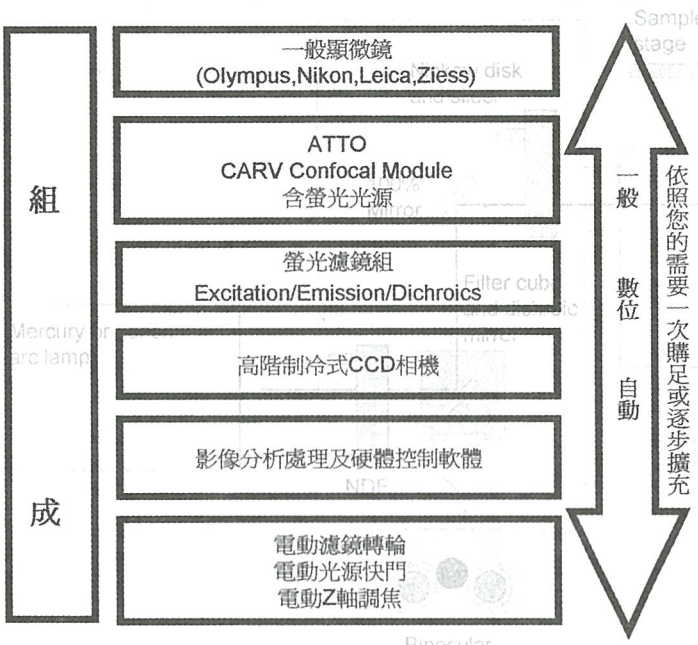

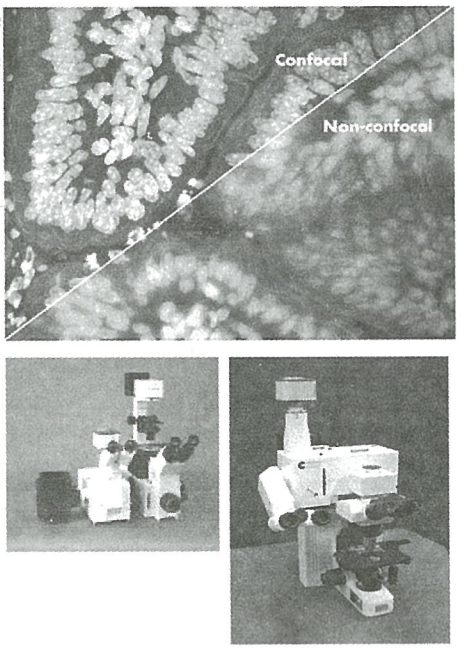

QPe 穿透式電子顯微鏡位相差系統

QUANTITATIVE PHASE ELECTRON MICROSCOPE

數位時代新選擇!!!

跨時代的改革新技術!!!

- Enhanced image contrast without the need for staining techniques.
- Ease of differentiation of structures within samples free of intensity artifacts.
- Optical density (Phase) data on samples for a more complete analysis

位相差系統優勢

- 快速地爲電顯影像提供各種成像模式
  Differential Interference Contrast (DIC)
  Hoffman Modulation Contrast (HMC)
  Zernike Phase Contrast (ZPC)
  Simulated Darkfield
- 分別記錄相位和光強度信息
- 可做定量分析，測量光強度、弧度、波長、光學厚度
- 厚度、折射率等參數測量
- 影像訊息數據可以長久保存

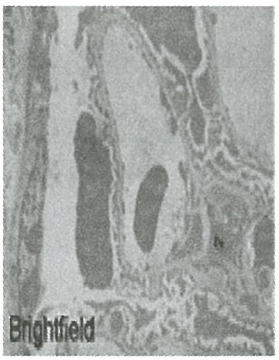

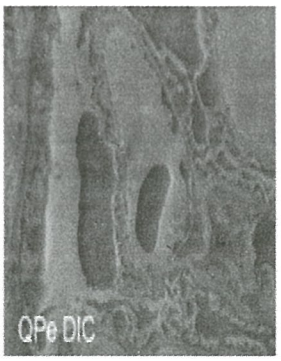

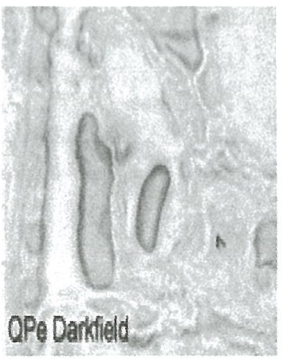

位相差系統應用

材料科學
- 可測量折射率指標或物質的厚度
- 光電材料、矽晶片研究、礦物學

生物科學
- 定量分析樣本(厚度/折射率指標/光強度)、對照分析
- 測量樣品隨著時間的相對改變、結構的相對差異
- 血液分析、癌症研究、醫藥研究

KEYBOND
技邦科技
技邦企業股份有限公司
KEYBOND TECHNOLOGY INC.

台北市士林區大南路354號1樓
TEL : (02)2882-5585 FAX : (02)2882-536
台中市五權西路二段131號9樓之3
TEL : (04)2475-0325 FAX : (04)2473-6041

高雄市大順一路93號7樓之3
TEL : (07)558-5868 FAX : (07)558-5953
Http://www.keybond.com

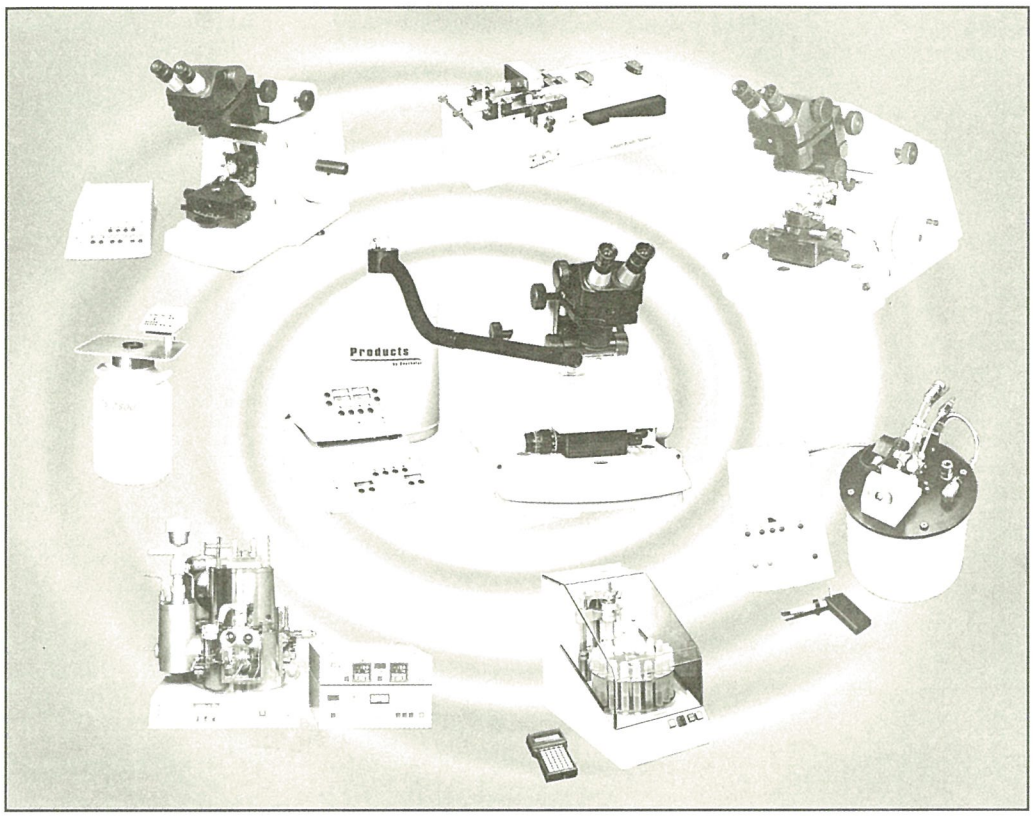

RMC-EM
Preparation Products

Products
by Boeckeler

嘉威國際有限公司
CBV Enterprise Inc.
台北市北投區石牌路二段 17 巷 90 號 5 樓
TEL:28250747　FAX:28209904